The Effect of Low Frequencies on Seismic Data in Theory and a West Texas Case Study

by

Nicholas Carter McDaniel

A thesis submitted to the Department of Earth and Atmospheric Sciences,

College of Natural Sciences and Mathematics

in partial fulfillment of the requirements for the degree of

Master of Science

in Geophysics

Chair of Committee: Robert R. Stewart

Committee Member: John P. Castagna

Committee Member: David J. Monk

University of Houston

May 2020

DEDICATION

To my family. I couldn’t have done this without your love and support.

ACKNOWLEDGEMENTS

This work would not have been possible without the generous donation of data and funding from Apache Corporation. Thanks to my advisor, Dr. Robert Stewart and my committee members, Dr. John Castagna and Dr. David Monk for pushing me to strive for more than I knew I was capable of. Thanks to the University of Houston Allied Geophysical Lab and my amazing cohorts for making me smile every day on campus. A very special thank you to Jim Parker, NSM Graduate Academic Advisor, for calling me directly to offer me admission to this program upon seeing the University of Houston overlooked my application and the many great conversations that followed. Finally, thanks to my family for… everything.

ABSTRACT

Low frequencies in seismic data are important as they contribute to better wavelet stability, resolution, penetration, and inversion. These contributions from low frequencies in the seismic frequency band are investigated in theoretical terms through synthetic modeling and in a practical application via analysis of field data.

Modeling wavelet stability shows that attributes of the seismic wavelet, such as peak-to-trough ratio, central lobe width, and central-to-sidelobe energy ratio, have a complex relationship to the frequency band that is often not dependent upon the maximum or minimum frequencies independently. Modeling penetration reiterates the importance of low frequencies for long travel paths because of the inverse relationship of frequency to scattering and absorption. Modeling impedance inversion with varying frequency band demonstrates the importance of low frequencies in filling the gap between conventional seismic and well log data. Modeling of the Fresnel zone connects spatial resolution to frequency and introduces the possibility of sparse sampling for low frequencies.

Comparison of field data from a 2D seismic line in West Texas with collocated conventional geophones (10Hz) and low-frequency geophones (5 Hz) investigates the additional coherent frequency content from use of low-frequency geophones and the value of the associated extension of the frequency band. This analysis was performed through a comparison of frequency spectra, comparison of filter panels, and calculation of magnitude squared coherence using the raw data and comparison of frequency spectra, filter panels, and extracted wavelets in the processed data. The low-frequency geophone dataset did not yield as much coherent low-frequency content as anticipated, likely due to a lack of strong low-frequency signal in the presence of significant low-frequency noise.

In conclusion, synthetic modeling demonstrated the importance of low frequencies in seismic data, while the field data analysis did not yield as much coherent low-frequency content as anticipated, likely due to lack of strong low-frequency signal in the presence of significant low-frequency noise.

TABLE OF CONTENTS

LIST OF TABLES

LIST OF FIGURES

Chapter 1: INTRODUCTION

1.1 Motivation and Objective

As the world wrestles with the challenge of reducing greenhouse gasses and the precarious state of the price of oil, the subject of carbon dioxide (CO_2) injection as a method of enhanced oil recovery (EOR) and CO_2 sequestration has become increasingly popular. According to the United States Department of Energy, CO_2-EOR has the potential to produce over 60-billion barrels of oil by expanding the technique into basins throughout the United States (United States Department of Energy, 2011). CO_2-EOR, however, is not presently well-characterized and requires time-lapse geophysical monitoring to decipher the CO_2 migration. In many cases, the geophysical method of choice is 4D or repeated 3D seismic technology. The 4D seismic images allow the interpreter to analyze the changes of the elastic properties captured in 3D space by the seismic survey at a time before the injection and later, during the injection. An accurate interpretation requires knowledge of the effect of CO_2 on rock properties and adequate seismic data quality and resolution (Miller et al., 2006).

The genesis of this thesis is a cooperative effort by the University of Houston and Apache Corporation to improve future seismic acquisition design to resolve subtle differences in a carbonate reservoir under CO_2 flood in the Permian Basin to improve the enhanced oil recovery, time-lapse reservoir monitoring, and rock property estimations (Hirscha et al., 1990). Preliminary analysis was undertaken through a simple evaluation of the influence of CO_2 in various rocks through Gassmann fluid substitution modeling (see APPENDIX A). Following the preliminary rock physics evaluation, Apache Corporation acquired a 2D seismic line comprised of a variety of vibroseis sweeps and different receiver models to test different combinations of sources and

receivers. Apache Corporation has generously provided the University of Houston with these datasets.

The acquisition design of the 2D seismic line emphasized low-frequencies by using sweeps starting at 1.5 Hz and including low-frequency receivers. This design was motivated by research showing that low frequencies increase wavelet stability, resolution, penetration, and inversion quality (ten Kroode et al., 2013). The objective of this thesis was to investigate the contributions from low frequencies in the seismic frequency band in theoretical terms through synthetic modeling and in a practical application via analysis of field data provided by Apache Corporation.

1.2 Datasets Used

This research utilizes data from a high-density 2D seismic line comprised of five different types of nodal geophones (Table 1.1) and four different vibroseis source sweeps/configurations (Table 1.2) acquired and generously provided by Apache Corporation.

This research focuses on the data from the FairfieldNodal ZLand and GoK Low-Frequency receivers acquired with the two vibroseis 15-second linear sweep. From this combination, the influence of extended bandwidth gained by utilizing a low-frequency receiver as opposed to a conventional receiver can be analyzed. There is a wealth of data in this full dataset that could be explored in further research evaluating topics such as sampling intervals for source and receiver, one vibroseis versus two vibroseis or 8-second versus 15-second vibroseis configuration, and linear versus low dwell vibroseis sweeps.

Table 1.1 Geophone specifications.

	Spacing	Corner Frequency	Sample Interval
FairfieldNodal ZLand	27.5' (~8.4m)	10 Hz	2 ms
Geospace GS30-CT 3C	110' (~33.5m)	10 Hz	2 ms
Innoseis Tremornet	Variable	5 Hz	2 ms
GTI Nuseis	27.5' (~8.4m)	10 Hz	2 ms
GoK Low-Frequency	110' (~33.5m)	5 Hz	2 ms

Table 1.2 Source specification and availability for geophones.

	1 Vibe 8s Linear	2 Vibe 8s Linear	2 Vibe 15s Linear	2 Vibe 15s Low Dwell
Shot Interval	27.5' (~8.4m)	27.5' (~8.4m)	55' (~16.8m)	55' (~16.8m)
Number of Sweeps	412	412	205	205
Frequency	1.5 – 120 Hz	1.5 – 120 Hz	1.5 – 120 Hz	1.5 – 120 Hz
FairfieldNodal ZLand	X	X	X	X
Geospace GS30-CT 3C	X	X	X	X
Innoseis Tremornet	X	X	X	X
GTI Nuseis	X		X	
GoK Low-Frequency	X	X	X	X

1.3 Acquisition Overview

The high-density 2D (HD2D) data used in this thesis were acquired on January 10th, 2017 as part of a larger 4D and upscaled 3D acquisition in West Texas between Lubbock and Midland. The surface land of the acquisition area is largely agricultural with active wells interspersed throughout the area. The survey source sweeps used at even and odd shot point numbers were non-uniform (Table 1.3) allowing creative move-up design for the vibrators.

Table 1.3 Sweeps at even and odd shot points.

	2 Vibe 15s Low Dwell	2 Vibe 15s Linear	2 Vibe 8s Linear	1 Vibe 8s Linear
Even Source Points	X	X	X	X
Odd Source Points			X	X

Table 1.4 Choreography of vibe acquisition and move-up.

Vibe 1	15s LD	15s Linear	8s Linear	Move-up	8s Linear	8s Linear	Move-up
Vibe 2	15s LD	15s Linear	8s Linear	8s Linear	Move-up	8s Linear	Move-up

The vibrators were choreographed to acquire all three shots at even points that required both vibe 1 and vibe 2, then vibe 1 would move to the next location (an odd point) as vibe 2 swept the final shot only requiring one vibe. As vibe 2 then moved to meet vibe 1 at the next odd shot point vibe 1 swept the shot only requiring one vibe. Vibe 1 would then arrive at the odd shot point as vibe 2 finished the sweep and the two vibes would sweep the shot requiring two vibes at that shot point before both vibes moved to the next even shot point together and repeated the process (Table 1.4 and Figure 1.1). This source move-up choreography allowed 412 shot points to be acquired over 9 hours and 19 minutes at a rate of 44 shot points/hour. Due to the fact that time of acquisition has a major influence on acquisition cost, further analysis of optimal vibroseis choreography is warranted in future research.

Figure 1.1 Image of 2 vibes during acquisition of HD2D line. One vibe is moving-up as the other is sweeping a shot.

Figure 1.2 Planted Innoseis nodal geophone.

Figure 1.3 Planted GTI nodal geophone.

Figure 1.4 Planted Z-Land nodal geophone.

Figure 1.5 Planted Geospace 3C geophone with battery and recorder.

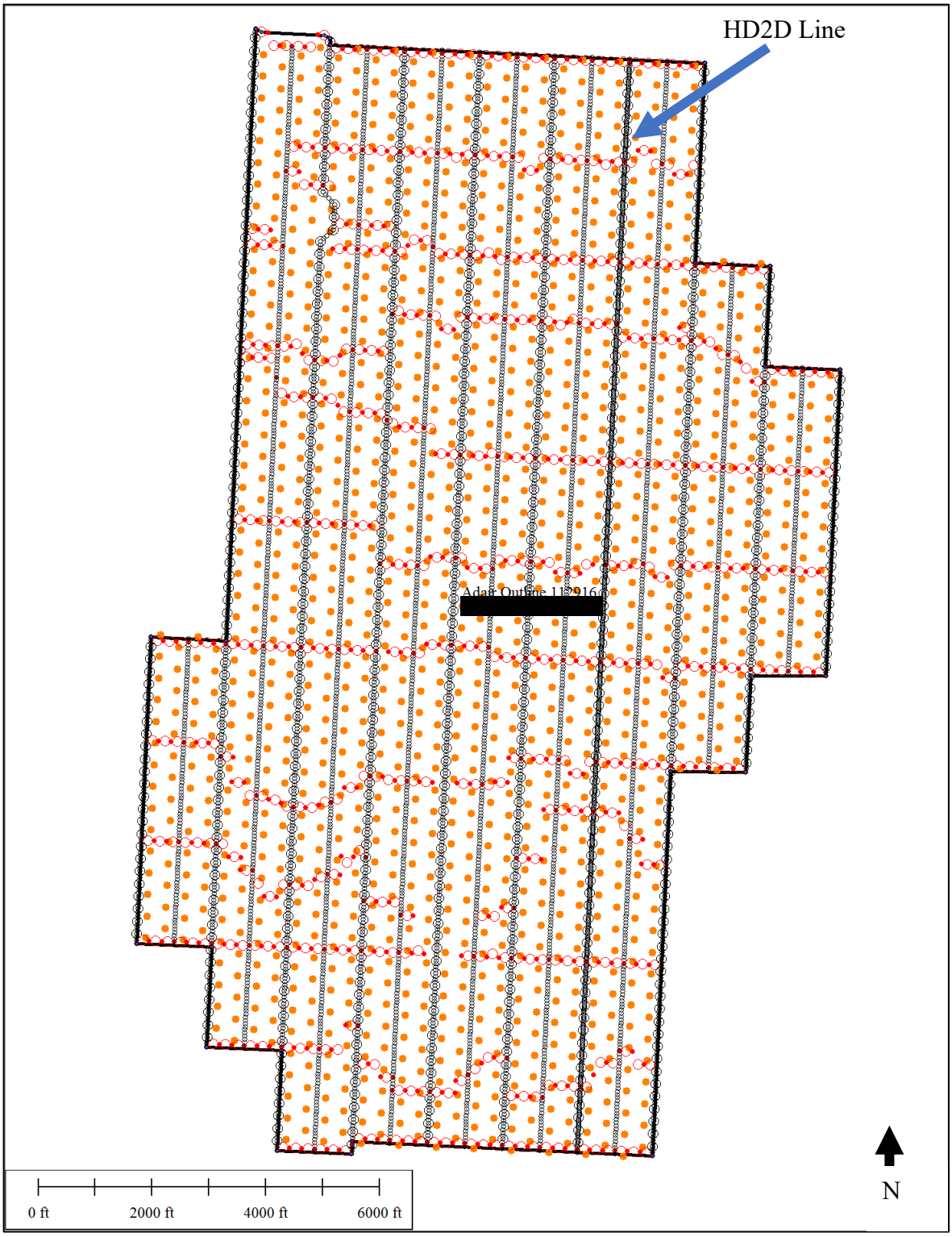

Figure 1.6 Total survey geometry. Gray and orange symbols are receiver locations. Red symbols are source locations.

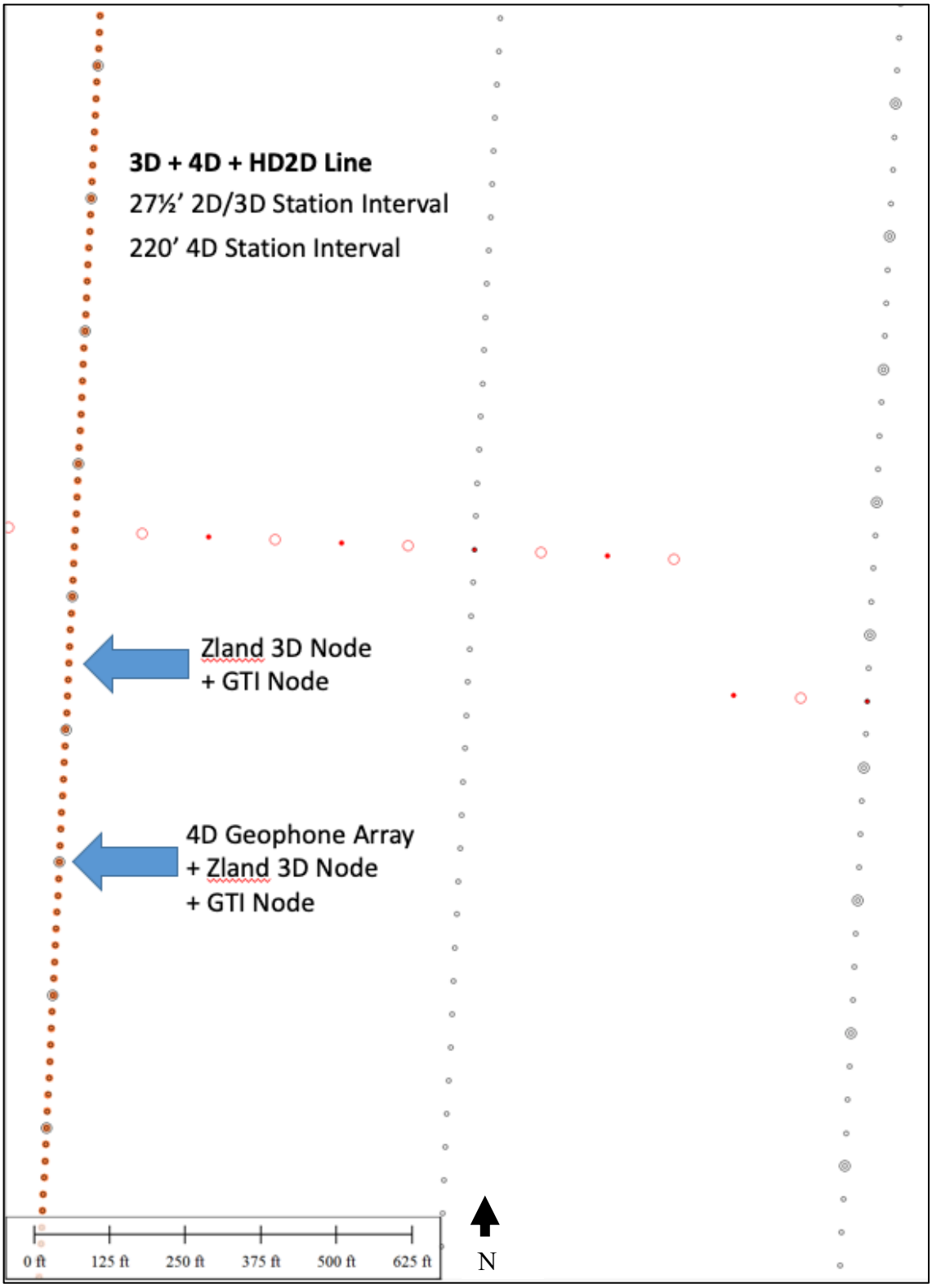

Figure 1.7 Detailed survey layout for HD2D portion of survey.

1.4 Geology and Map

The target formation for this study is a Permian age, approximately 500 foot (~150 meter) thick, dolomitized carbonate at a depth between 3000 and 5000 feet (~915 and 1525 meters) TVD located between Midland and Lubbock in the Permian Basin (Figure 1.8). This formation is characterized by an upward shallowing succession of outer to inner-ramp carbonate lithofacies with an average porosity around 10% (Ruppel, 2006) (Figure 1.9). This formation was produced conventionally since the 1920s and has been the subject of an enhanced oil recovery (EOR) CO2 flood in more recent years.

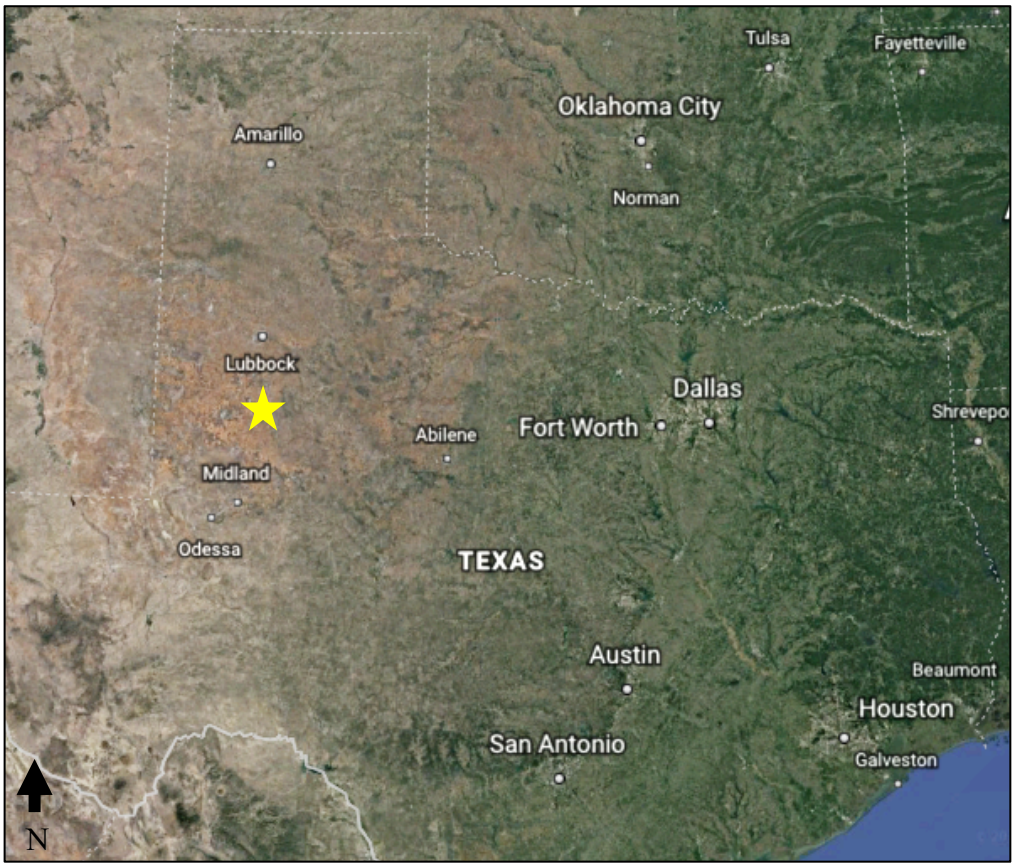

Figure 1.8 Regional map of Texas with yellow star indicating the general location of the survey. (Google, 2019)

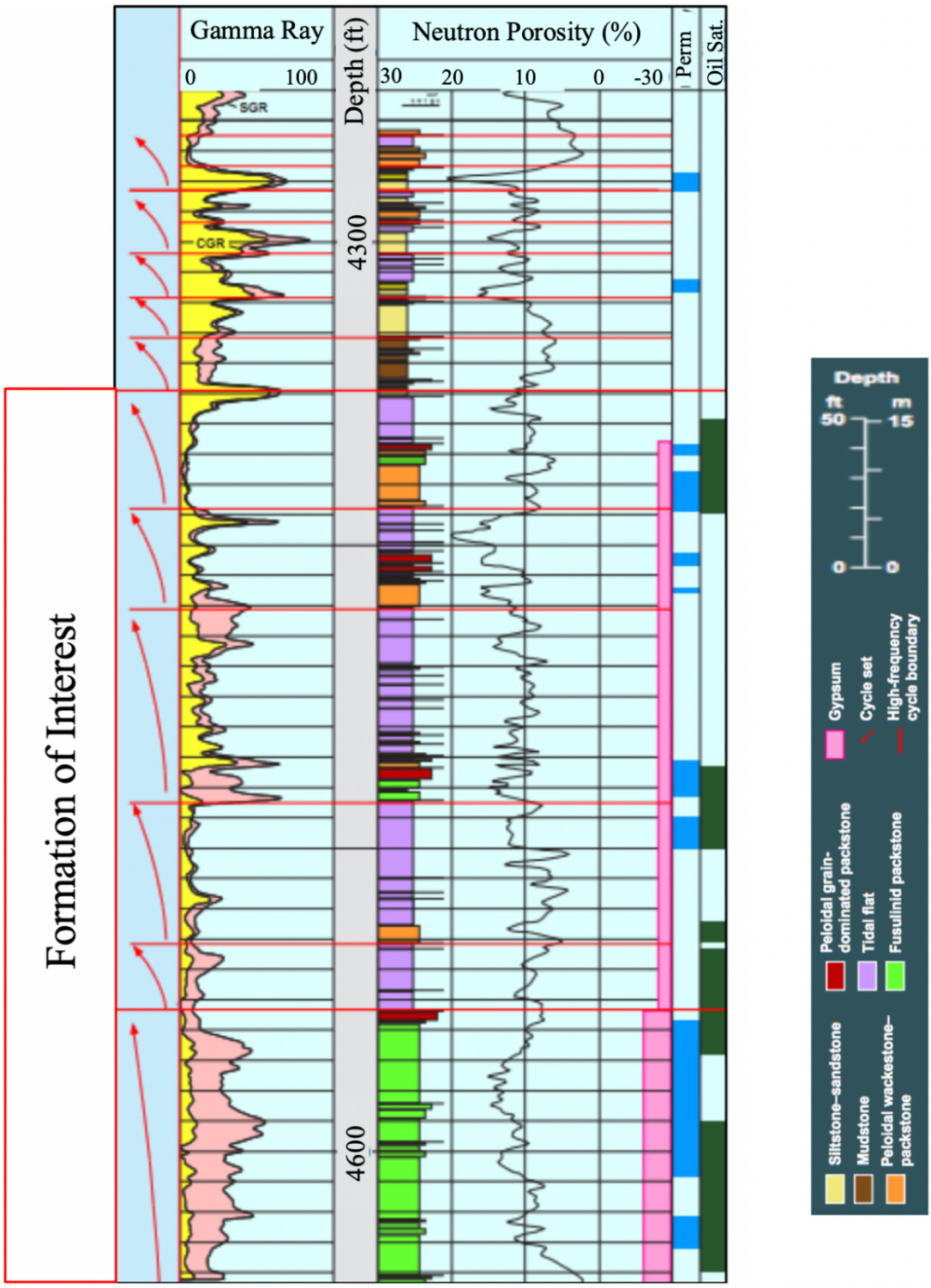

Figure 1.9 Gamma ray and neutron porosity log annotated with stratigraphy and facies of formation of interest. (Ruppel, 2006)

1.5 Software Used

The software used in this thesis includes VISTA, a desktop seismic data processing software from Schlumberger, for the processing of seismic data, RokDoc, a quantitative interpretation software from Ikon Science, for the wavelet extractions, and MATLAB, a high-level programming language developed by MathWorks, for wavelet and Fresnel zone modeling. CREWES (Consortium of Research in Elastic Wave Exploration Seismology) developed a toolbox of a large collection of geophysical codes for research in exploration seismology that was used extensively in this thesis.

Chapter 2: IMPORTANCE OF LOW-FREQUENCIES

2.1 Introduction

Low-frequency content in seismic data is important as it contributes to better wavelet stability, resolution, penetration, and inversion. In particular, extending the bandwidth of the recorded seismic signal at the low end of the spectrum leads to fewer sidelobes on the wavelet. In addition, low frequencies scatter less and suffer less from absorption in the earth, so they penetrate deeper, the number of local minima in least-squares misfit functions used in full-waveform inversion is smaller, so we have a better chance to converge to the true earth model with this method, and finally, a richer low-frequency content may eliminate the need for well-derived velocities to fill the traditional bandgap in impedance inversion (Smith et al., 1991; ten Kroode et al., 2013).

2.2 Wavelet Stability

The seismic wavelet is the important link between seismic data and stratigraphy as well as rock properties of the subsurface (Cui and Margave, 2014). With a stable wavelet, seismic interpretation can then be performed with the highest possible confidence, circumventing potential pitfalls introduced by laterally and/or temporally varying wavelets (Baan, 2012). The interpretive quality of a wavelet is also related to the relative size of its side lobes. Smaller side lobes mean less ambiguity, fewer interferences, and higher accuracy in interpretation (Kallweit and Wood, 1982; Zeng and Backus, 2005). Furthermore, seismic data processors tend to focus on the seismic wavelet when considering the deconvolution problem because if the wavelet is reliably estimated, it can generally be deconvolved or shaped with a digital filter (Dey, 1999). Therefore, a more

stationary and stable wavelet should result in a more accurate deconvolution. The following sections analyze the bandwidths of Ricker and Klauder wavelets in terms of Peak-to-Trough Ratio, Central Lobe Width, and Sidelobe Energy.

The Ricker wavelet is a zero-phase, second derivative of the Gaussian function that is commonly used in seismic modeling or manufacturing synthetic seismograms. The equation for the Ricker wavelet with peak frequency f_M at time t is given by:

(2.1)

$$amplitude\colon\ f(t) = (1 - 2\pi^2 f_M^2 t^2)e^{-\pi f_M^2 t^2}$$

(2.2)

$$frequency\colon\ \ F(f) = \frac{2}{\sqrt{\pi}}\frac{f^2}{f_M^3}e^{-\frac{f^2}{f_M^2}}$$

The Klauder wavelet is, in effect, the seismic source waveform for correlated vibroseis records which is reached directly by autocorrelation of a vibroseis sweep. The Klauder wavelet is defined by its terminal low frequency, f_1, its terminal high frequency, f_2, and the duration of the input signal, T. The real part of the following formula will generate a Klauder wavelet (Neelima et al., 2018).

(2.3)

$$Klauder(t) = real\left[\frac{\sin\big(\pi kt(T-t)\big)}{(\pi kt)e^{2\pi i f_0 t}}\right]$$

Where,

$$k = \frac{f_2 - f_1}{T} \tag{2.4}$$

$$f_0 = \frac{f_2 + f_1}{2} \tag{2.5}$$

2.2.1 Peak-to-Trough Ratio (Ricker)

The analysis of the Ricker wavelet peak-to-trough ratio is performed by varying the single controlling factor of the wavelet, dominant frequency (f_M), and plotting the resulting wavelets and peak-to-trough ratios versus dominant frequency. The result of this exercise is shown in Figure 2.1. For every dominant frequency used to generate the Ricker wavelet, the peak-to-trough ratio is a constant of 2.2408. This result is not obvious in the top plot of Figure 2.1, but is more apparent in the middle plot, with a normalized maximum amplitude, and the bottom plot showing peak-to-trough ratio versus dominant frequency.

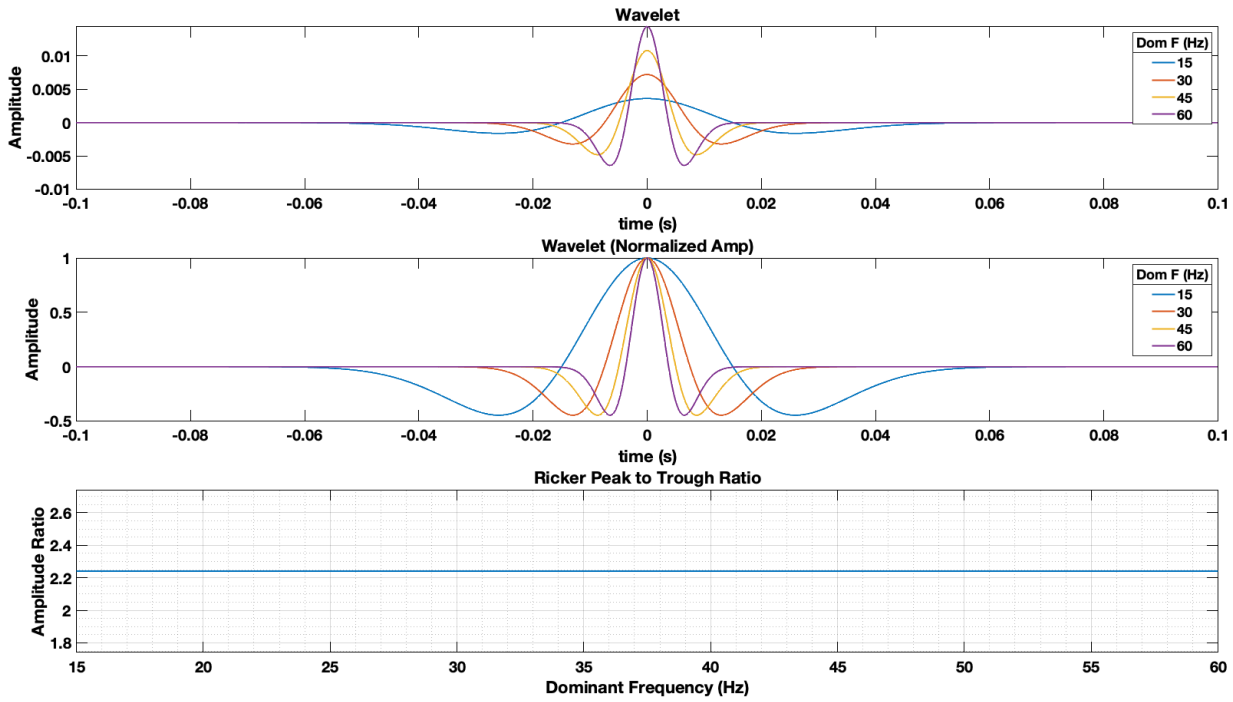

Figure 2.1 Top: Plot of Ricker wavelets with varying dominant frequencies. Middle: Plot of Ricker wavelets normalized to a max amplitude of 1 with varying dominant frequencies. Bottom: Plot of peak-to-trough ratio of Ricker wavelets vs dominant frequency.

2.2.2 Peak-to-Trough Ratio (Klauder)

Unlike the Ricker wavelet, the Klauder wavelet is defined by more than one input making the analysis slightly more involved. There are two inputs to adjust the frequency band of the wavelet, the terminal low frequency, and the terminal high frequency. In this analysis, the terminal low and high frequencies are adjusted independently and then dependently in terms of octaves to determine the effect of the inputs on the peak-to-trough ratio.

The first test holds the terminal high frequency constant (128 Hz) while varying the terminal low frequency from 1 Hz to 32 Hz. The results of this test are displayed in Figure 2.2. The peak-to-trough ratio versus minimum frequency, in the second plot from the bottom, shows

an exponential decay trend. Another way to think of this trend is in the opposite direction as exponential growth. As the terminal low frequency is pushed lower, the peak-to-trough ratio increases exponentially. To understand how the total bandwidth is affected concurrently with the peak-to-trough ratio, the number of octaves in the frequency band must be compared to the peak-to-trough ratio in the bottom plot. This plot shows a logarithmic trend in which the peak-to-trough ratio increases more rapidly at a lower number of octaves and flattens out with more octaves of bandwidth. This flattening out with more octaves shows diminishing returns of peak-to-trough ratio with bandwidth which should be considered against the increase in the effort needed to achieve the higher bandwidth in seismic surveys.

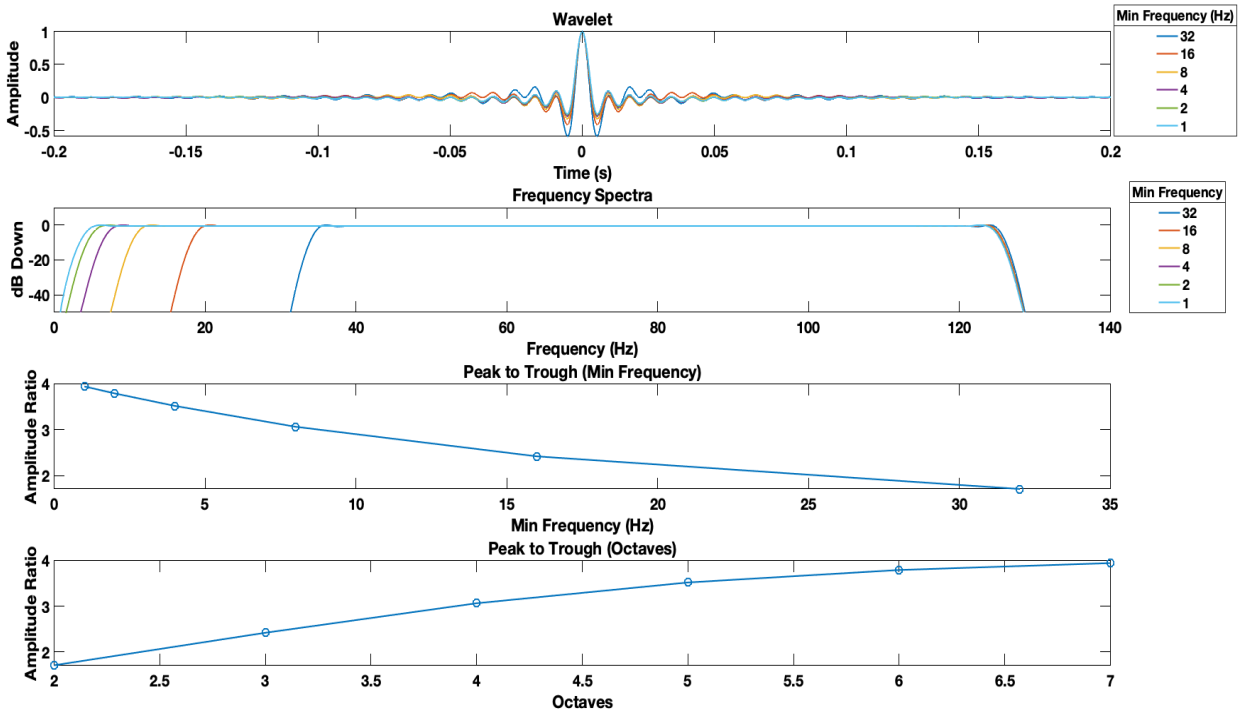

Figure 2.2 Top: Plot of normalized Klauder wavelets with varying terminal low frequencies (1, 2, 4, 8, 16, 32 Hz) and constant terminal high frequencies (128 Hz). Middle Top: Plot of frequency spectra for wavelets in the top plot. Middle Bottom: Plot of peak-to-trough ratio versus terminal low frequency. Bottom: Plot of peak-to-trough ratio versus octaves.

The second test for the investigation of the peak-to-trough ratio of the Klauder wavelet holds the terminal low frequency constant (1 Hz) while varying the terminal high frequency from 4 Hz to 128 Hz (total bandwidth of 2 to 7 octaves). The results of this test are displayed in Figure 2.3. The peak-to-trough ratio versus maximum frequency, in the second plot from the bottom, shows a logarithmic trend. Interestingly, when comparing this to the trend seen in the same plot in Figure 2.2, the extension of bandwidth in the higher frequencies has a smaller effect on peak-to-trough ratio than the extension of bandwidth in the lower frequencies. However, when comparing the extension of bandwidth in the lower and higher frequencies in terms of octaves as shown in the bottom plots of figures 2.2 and 2.3 respectively, the plots are the same irrespective of terminal low frequency or terminal high frequency.

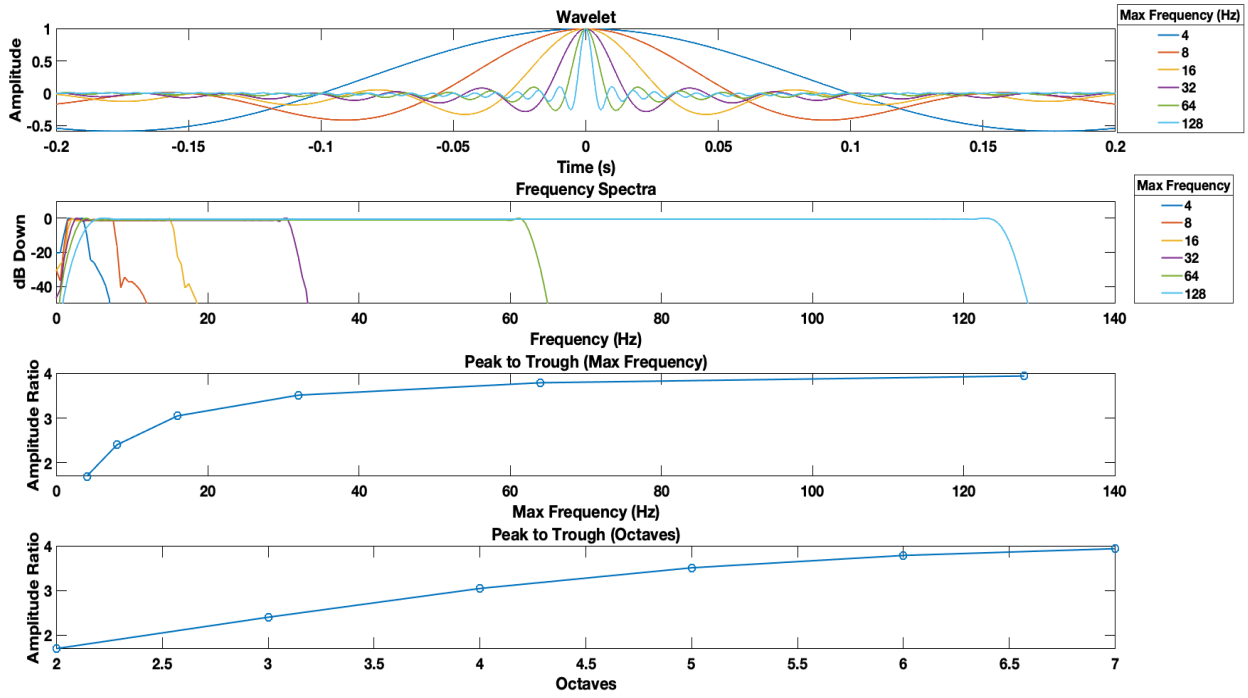

Figure 2.3 Top: Plot of normalized Klauder wavelets with varying terminal high frequencies (4, 8, 16, 32, 64, 128 Hz) and constant terminal low frequency (1 Hz). Middle Top: Plot of frequency spectra for wavelets in the top plot. Middle Bottom: Plot of peak-to-trough ratio versus terminal high frequency. Bottom: Plot of peak-to-trough ratio versus octaves.

To test the observation that peak-to-trough ratio is dependent upon octaves of bandwidth rather than terminal low frequency or terminal high frequency the peak-to-trough ratio must be calculated with varying terminal low frequency and terminal high frequency while keeping the number of octaves of bandwidth constant. To determine the frequencies to use in this test, the terminal low frequencies were first selected ($f_l = 2,\ 3,\ 4,\ 5,\ 6$ Hz), the number of octaves to test was selected ($Oct = 4$) and the terminal high frequencies ($f_h = 32, 48, 64, 80, 96$ Hz) were calculated by the formula below.

(2.6)

$$f_h = 2^{Oct} \times f_l$$

The bottom plot of Figure 2.4 shows that peak-to-trough ratio is constant when varying terminal low frequency and terminal high frequency at a rate such that the bandwidth is a constant number of octaves, as observed in the previous tests.

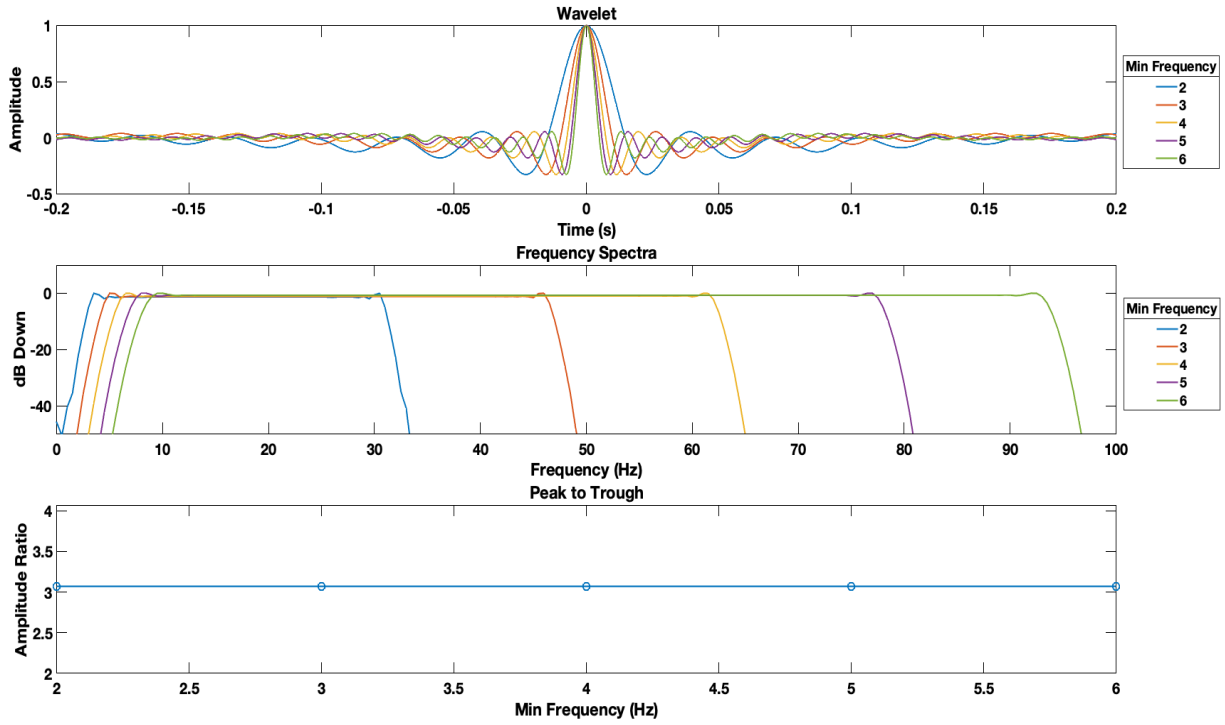

Figure 2.4 Top: Plot of normalized Klauder wavelets with a constant 4 octave bandwidth, varying terminal low frequencies (2, 4, 5, 6 Hz), and varying terminal high frequencies (32, 48, 64, 80, 96 Hz). Middle: Plot of frequency spectra for wavelets in the top plot. Bottom: Plot of peak-to-trough ratio vs minimum frequency (max frequency 4 octaves higher).

Some other helpful visualizations of the effects of terminal low frequency and terminal high frequency on the peak-to-trough ratio are shown in Figure 2.5 and Figure 2.6. The first two plots of Figure 2.5 are changing terminal low and terminal high frequencies with different constant terminal high and terminal low frequencies respectively and the bottom plot is the result of the previous two plots in terms of octaves. This figure serves as a general summary of the previous tests and can help with understanding Figure 2.6. Figure 2.6 is a 3D plot of peak-to-trough ratio versus minimum frequency and maximum frequency. Looking at the 3D plot from the perspective of the minimum frequency axis resembles the top plot of Figure 2.5 with the axis in the reverse

orientation and, similarly, looking at the 3D plot from the perspective of the maximum frequency axis resembles the middle plot of Figure 2.5 with the axis in reverse. From the 3D plot, it is clear that the increase in bandwidth at lower frequencies has a greater effect on peak-to-trough ratio than at higher frequencies as stated previously. This makes sense when considering what was observed for the dependence of peak-to-trough ratio on octaves since the number of octaves of bandwidth increases more rapidly at lower frequencies as shown in Figure 2.7. Furthermore, the character of the peak-to-trough ratio versus octaves plots showing a flattening at higher octaves can be explained by the observation that the number of octaves increases more rapidly than the peak-to-trough ratio at lower frequencies.

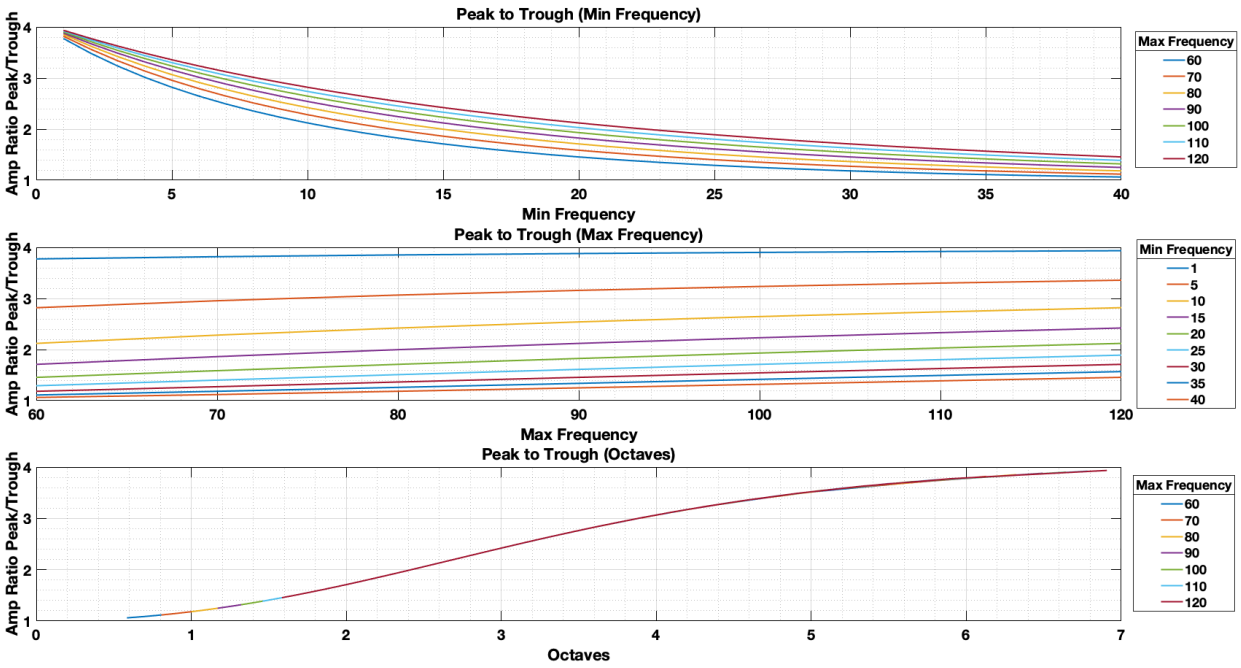

Figure 2.5 Top: Plot of peak-to-trough ratio versus minimum frequency with several different max frequencies. Middle: Plot of peak-to-trough ratio versus max frequency with several different minimum frequencies. Bottom: Plot of peak-to-trough ratio versus octaves with a range of bandwidths from the previous plots.

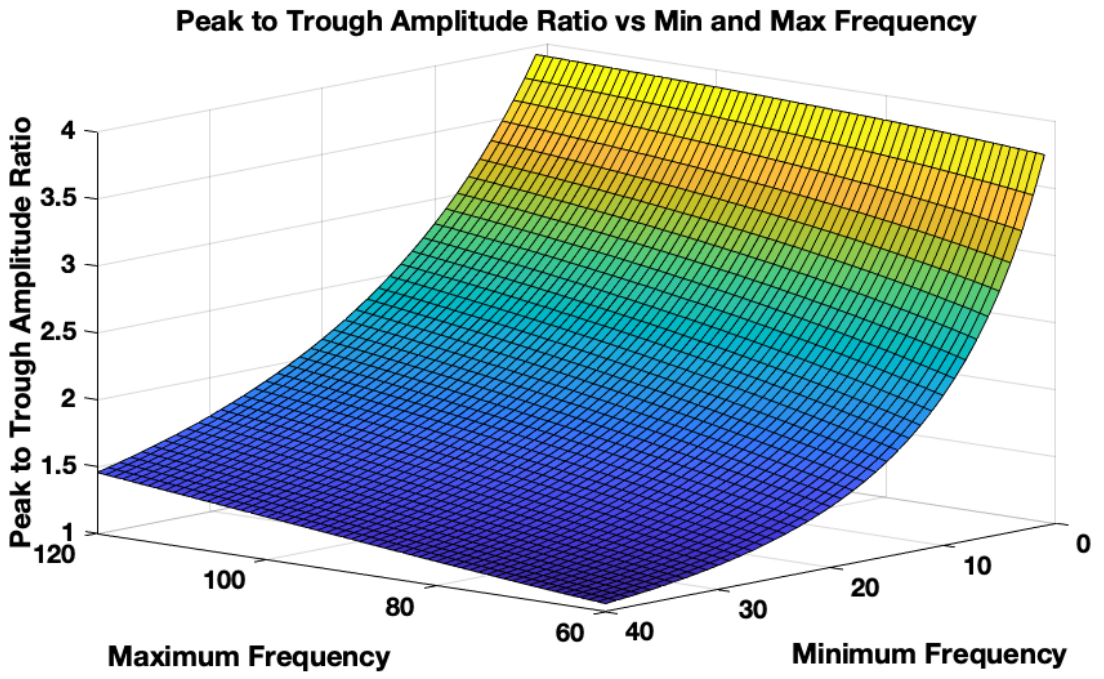

Figure 2.6 3D plot of peak-to-trough ratio versus minimum and maximum frequencies (Hz).

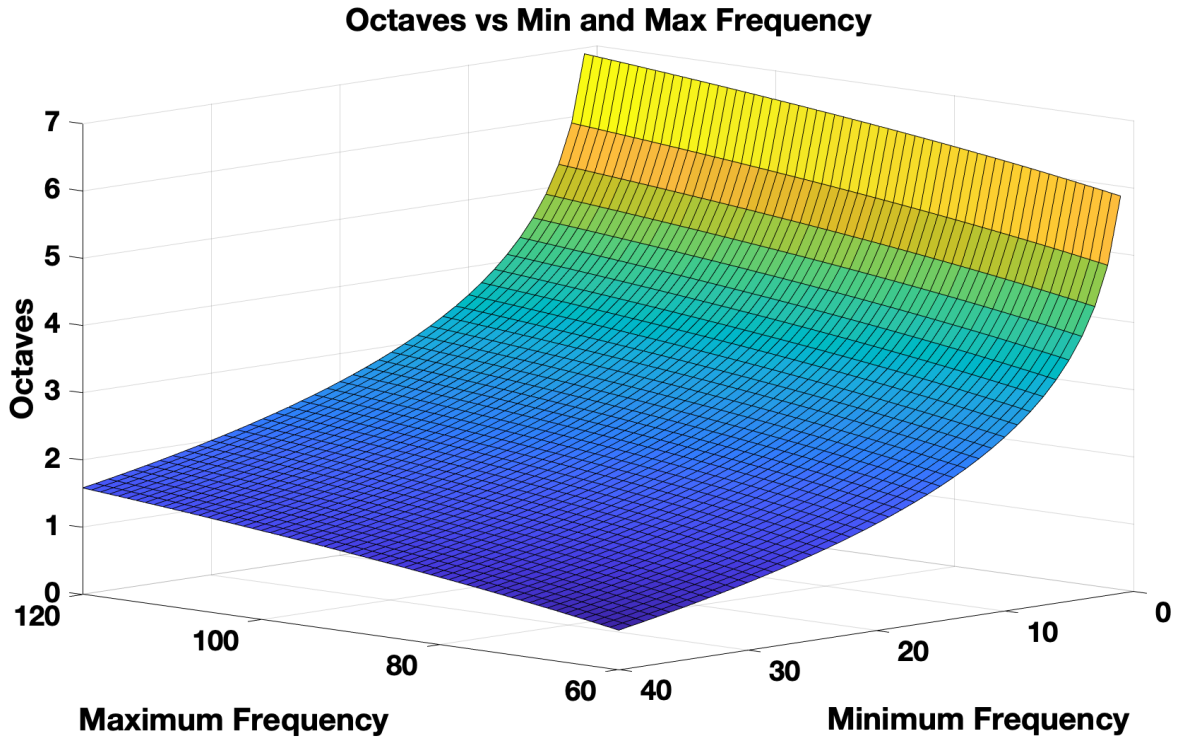

Figure 2.7 3D plot of Octaves versus minimum and maximum frequencies.

Taking these observations one step further, it is useful to determine the inflection point at which the effort to increase peak-to-trough ratio through bandwidth extension realizes diminishing returns. This can be achieved by locating the maximum of the derivative of the peak-to-trough ratio versus octaves as shown in Figure 2.8. The value of the inflection point was determined to be approximately 2.7 octaves of bandwidth. This is a useful observation that should aid in the consideration of effort to extend bandwidth in seismic surveys. While as much bandwidth as possible is the best option, extending bandwidth often involves increased costs associated with advanced sources and receivers. This observation shows that there is a greater return in effort expended increasing bandwidth to at least 2.7 octaves.

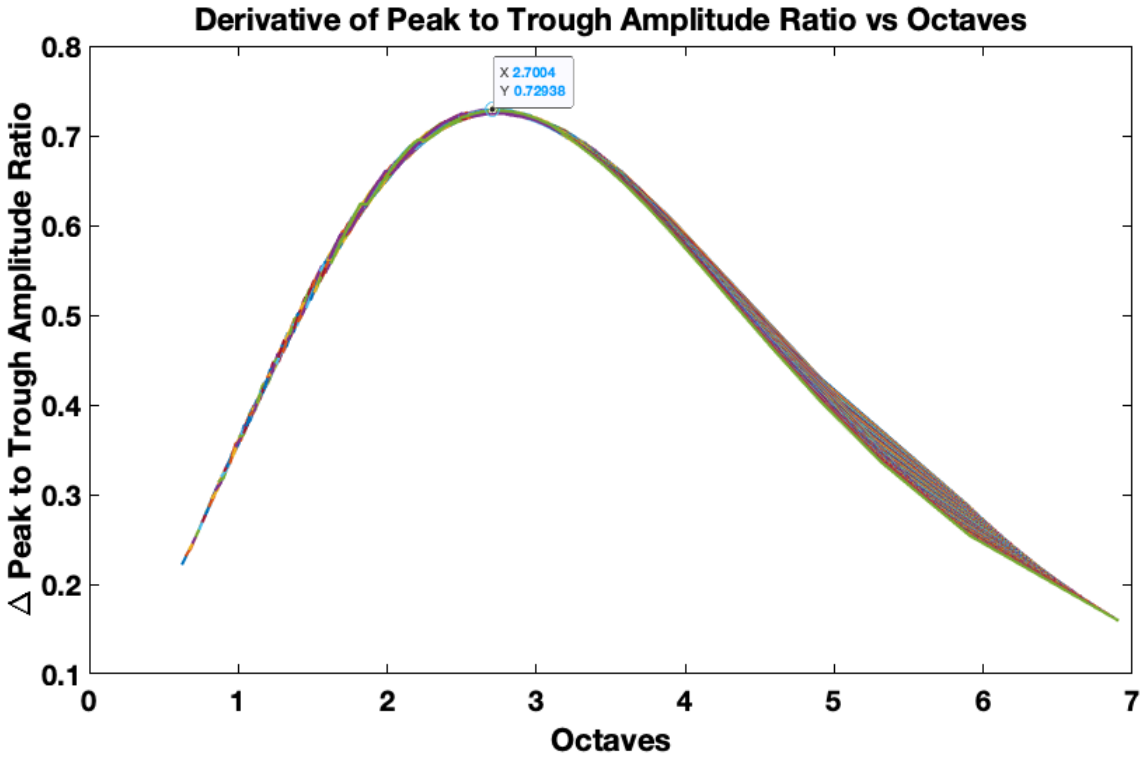

Figure 2.8 Plot of the derivative of peak-to-trough ratio versus octaves for Klauder wavelets. The marked point is maximum value of the derivative of this plot and inflection point of the peak-to-trough ratio versus octaves plot.

2.2.3 Central Lobe Width (Ricker)

The analysis of the Ricker wavelet peak-to-trough ratio is performed by varying the single controlling factor of the wavelet, dominant frequency (f_M), and plotting the resulting central lobe widths, calculated in terms of width between central zero-crossings, versus dominant frequency. The result of this exercise is shown in Figure 2.9. The expected general trend between central lobe width and frequency is observed in the plot showing a decrease in central lobe width as the dominant frequency is increased. However, the relationship between dominant frequency and central lobe width of the Ricker wavelet is exponential rather than linear. As the dominant frequency increases, the incremental decrease in central lobe width diminishes. This is due to the relationship between frequency (f) and wavelet period (T) for a sinusoid as shown in (2.7. Interestingly, upon observation of the bottom plot of Figure 2.9, it is evident that the central lobe width of the Ricker wavelet is smaller than that of a sinusoid with the same dominant frequency. This can be explained by the analysis of the frequency spectra in Figure 2.10. While the Ricker wavelet is constrained by a dominant frequency, the total frequency spectrum of a given wavelet spans beyond that frequency with a lower amplitude, unlike a simple sinusoid where the frequency spectrum would resemble a spike at the dominant frequency. This additional higher amplitude in the Ricker wavelet leads to a shorter period than a standard sinusoid for the same dominant frequency.

(2.7)

$$T = f^{-1}$$

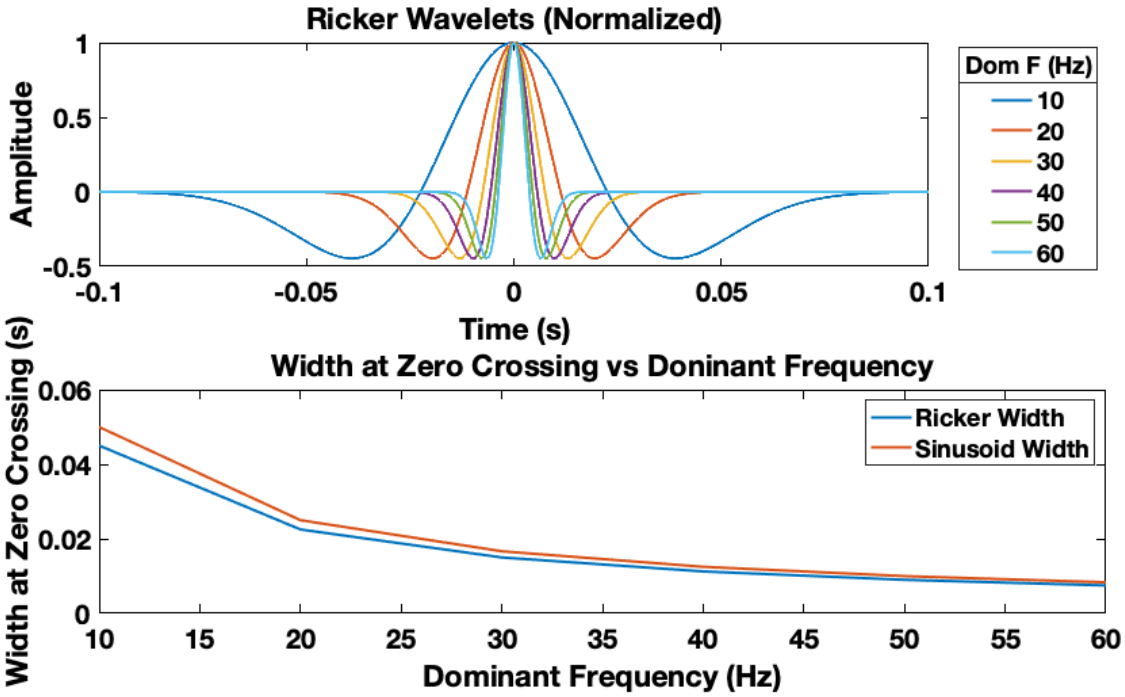

Figure 2.9 Top: Plot of normalized Ricker wavelets with varying dominant frequencies (10, 20, 30, 40, 50, 60 Hz). Bottom: plot of central lobe width at zero crossing versus dominant frequency for the Ricker wavelets in the top plot.

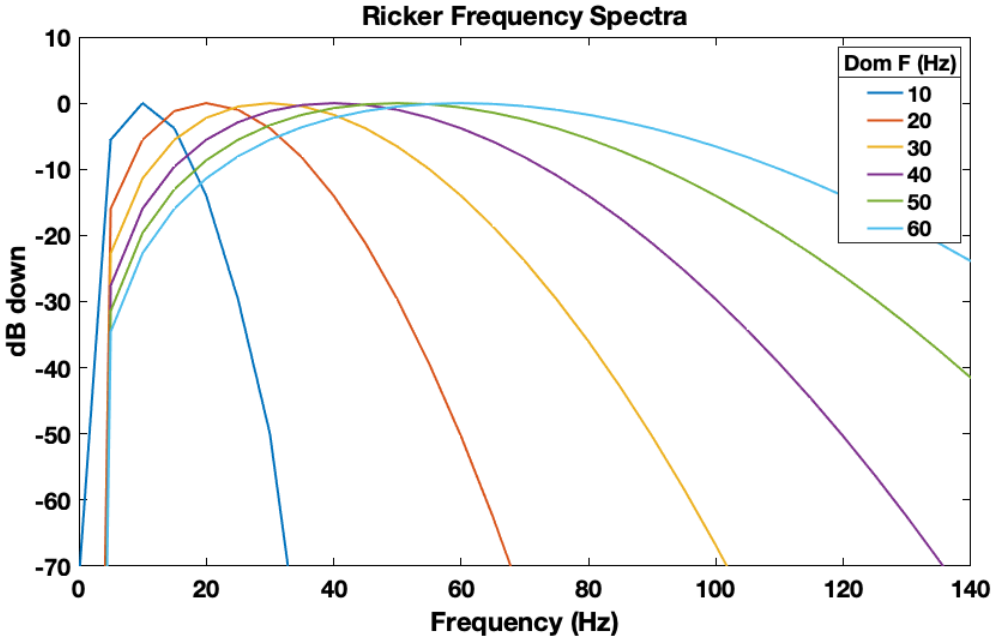

Figure 2.10 Plot of frequency spectra for wavelets in Figure 2.9.

2.2.4 Central Lobe Width (Klauder)

Similar to the tests of the peak-to-trough ratio for the Klauder wavelet, testing the central lobe width is also done by varying the terminal low frequency and terminal high frequency. Figure 2.11 shows the result of varying the terminal low frequency from 1 Hz to 40 Hz for Klauder wavelets with several different terminal high frequencies (60 Hz to 120 Hz). This plot shows that there is an exponential increase in central lobe width for the Klauder wavelet with decreasing terminal low frequency. While the general trend when reducing terminal low frequency is an increase in central lobe width, wavelets with higher terminal high frequencies experience less of a change than wavelets with lower terminal high frequencies. Comparing the wavelet with a terminal high frequency of 60 Hz to that of the wavelet with a terminal high frequency of 120 Hz, the wavelet with the higher terminal high frequency has a smaller change in central lobe width. This is also evident when observing the change in central lobe width at varied terminal high frequencies with constant terminal low frequencies in Figure 2.12. From these two plots, there is one important observation; Klauder wavelets with higher terminal high frequencies have a smaller central lobe width which is more stable with changing terminal low frequency than Klauder wavelets with lower terminal high frequencies. Another demonstration of the dependence of central lobe width on terminal low frequency and terminal high frequency is the 3D plot in Figure 2.13. By examination of the slopes along the x and y axes (Minimum Frequency and Maximum Frequency), one can observe the stronger dependence on maximum frequency by the greater slope along the Max Frequency axis and increased stability at high frequencies by the more subtle slope along the Min Frequency axis.

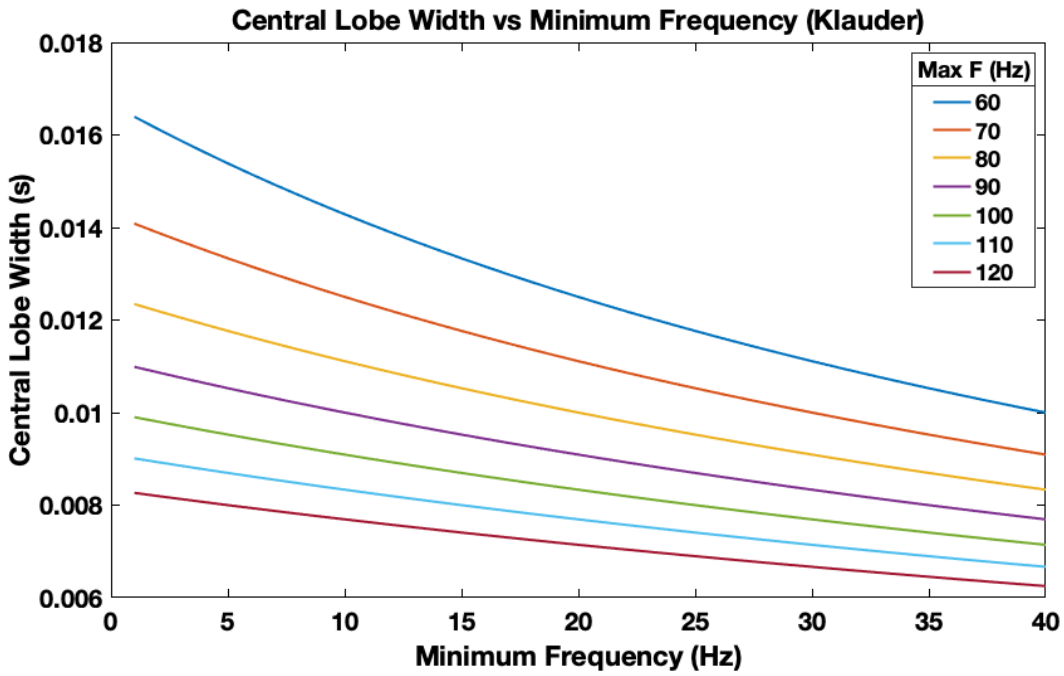

Figure 2.11 Plot of central lobe width versus minimum frequency for Klauder wavelets with several max frequencies (60 – 120 Hz).

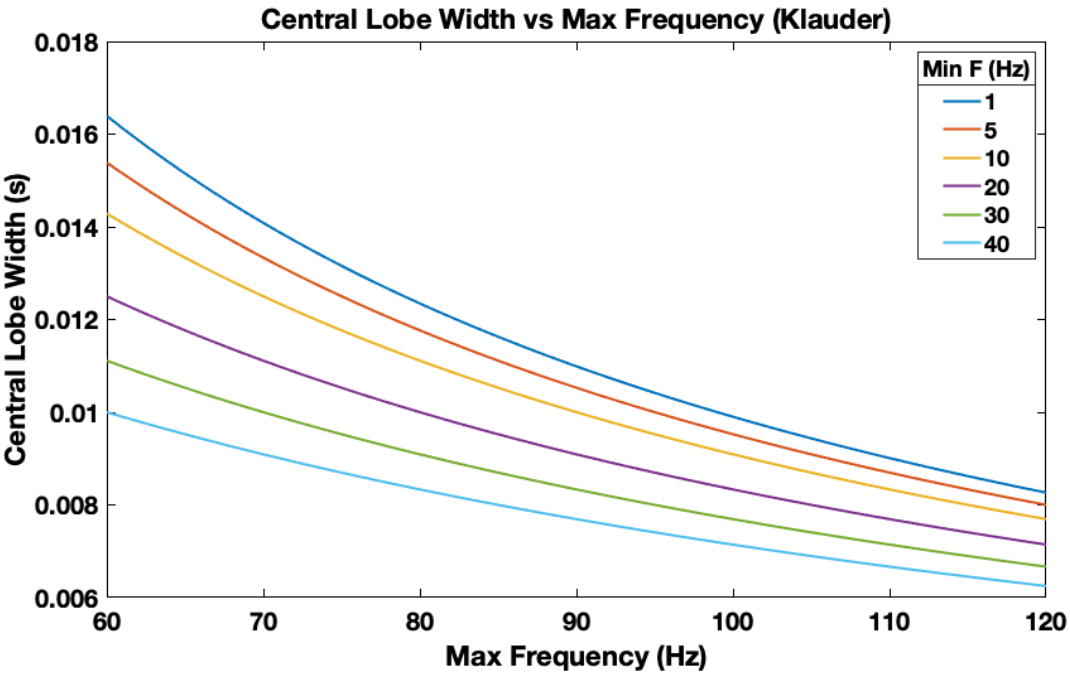

Figure 2.12 Plot of central lobe width versus max frequency for Klauder wavelets with several minimum frequencies (1 – 40 Hz).

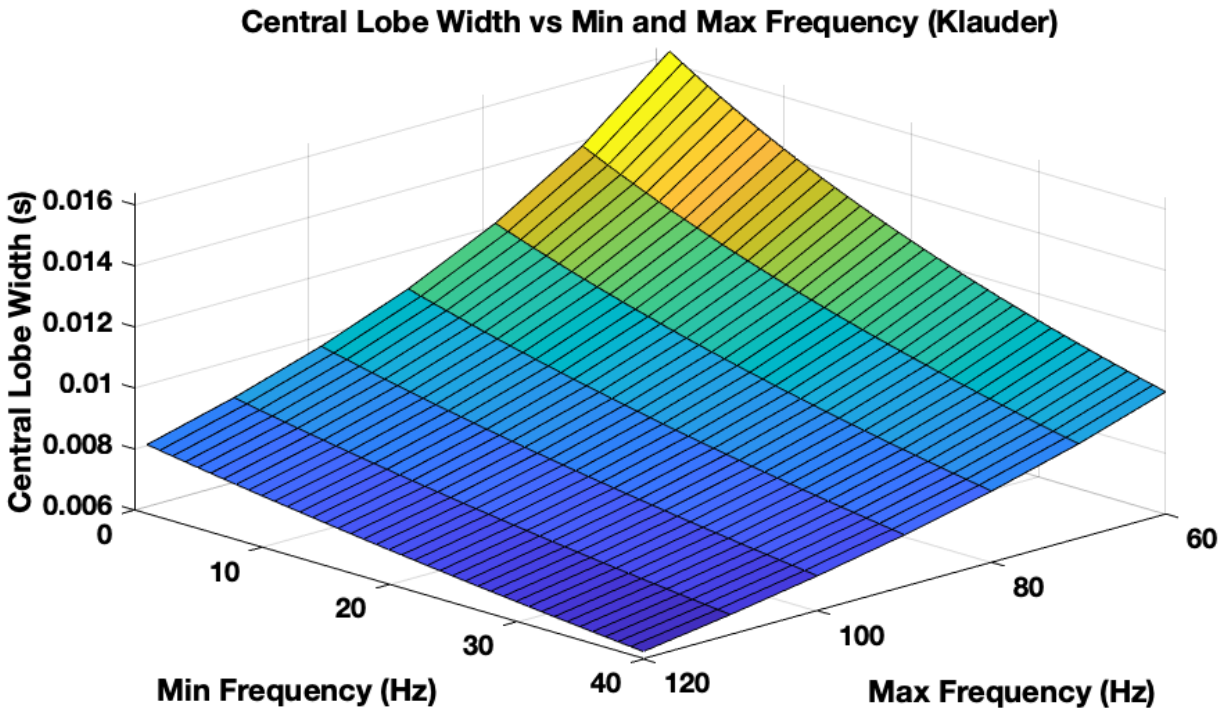

Figure 2.13 3D plot of Central Lobe Width vs Min and Max Frequency for a Klauder Wavelet.

The next test for investigating central lobe width for Klauder wavelets is through consideration of total bandwidth through octaves. Figure 2.14 shows central lobe width for Klauder wavelets with several different constant terminal high frequencies while varying terminal low frequencies plotted in terms of octaves. Unlike the observation made in section 2.2.2 regarding peak-to-trough ratio, this plot suggests bandwidth itself is not the controlling factor in central lobe width. The plot also shows that the greater the number of octaves of bandwidth, the more stable the central lobe width becomes. This can be seen more clearly in Figure 2.15, the derivative of the central lobe width versus octaves, by the asymptotic flattening of all derivatives at higher numbers of octaves.

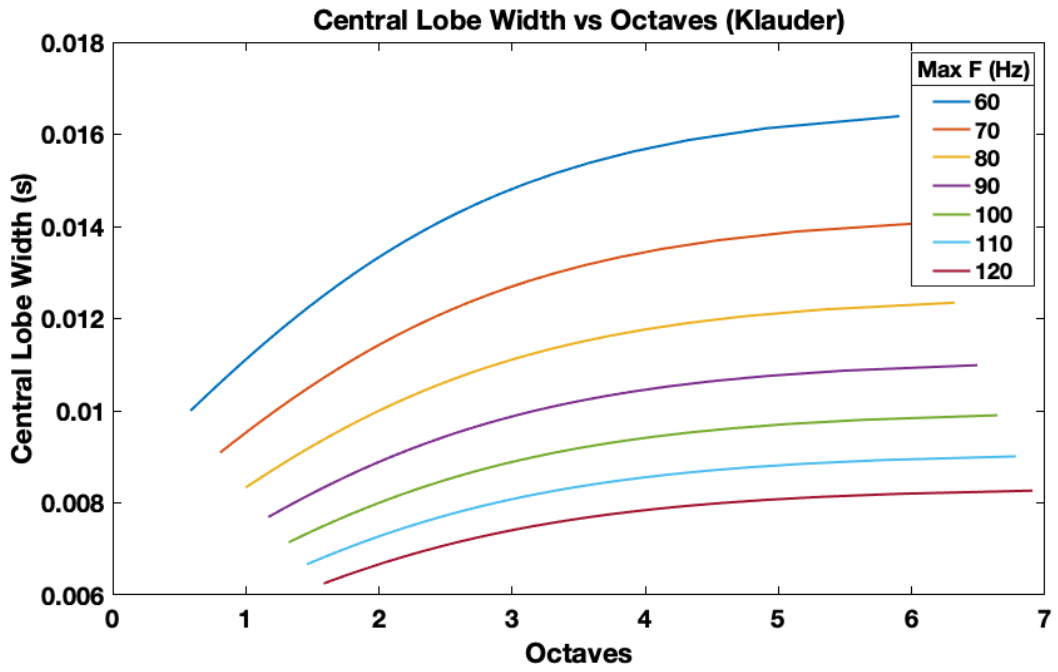

Figure 2.14 Plot of central lobe width versus octaves for Klauder wavelets with several constant max frequencies while varying minimum frequency.

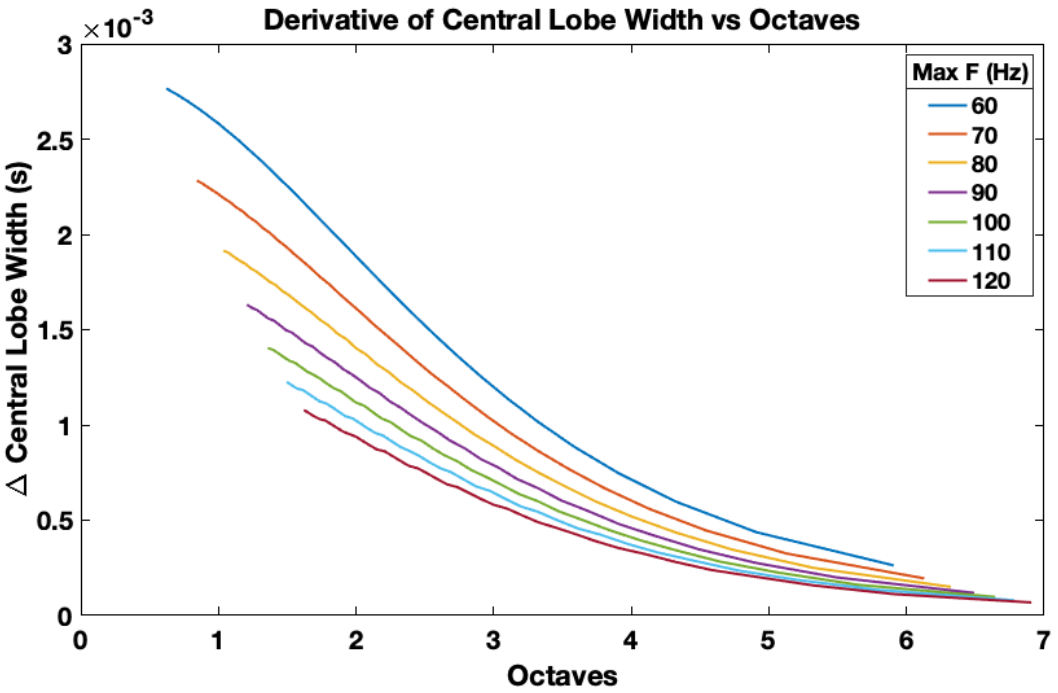

Figure 2.15 Plot of the derivative of Figure 2.13, central lobe width versus octaves for Klauder wavelets with several constant max frequencies while varying minimum frequency.

2.2.5 Central to Sidelobe Energy Ratio (Ricker)

Sidelobes are another component of wavelets that are of particular interest to geophysicists because of their negative influence on the identification of thin beds in seismic records. The investigation of Ricker wavelet sidelobe energy dependence upon dominant frequency can be summarized in Figure 2.16 and Figure 2.17. These figures show that for a Ricker wavelet of any dominant frequency, the sidelobe and central lobe areas are equal and, therefore, the central-to-sidelobe ratio is equal to 1. This is by design since the Ricker wavelet is the second derivative of the gaussian function, and the gaussian function is symmetric. Consequently, the integral of its second derivative is zero. Since all of the energy of a Ricker wavelet is in the central lobe and first side lobes, the ratio of central to sidelobe energy is equal to one.

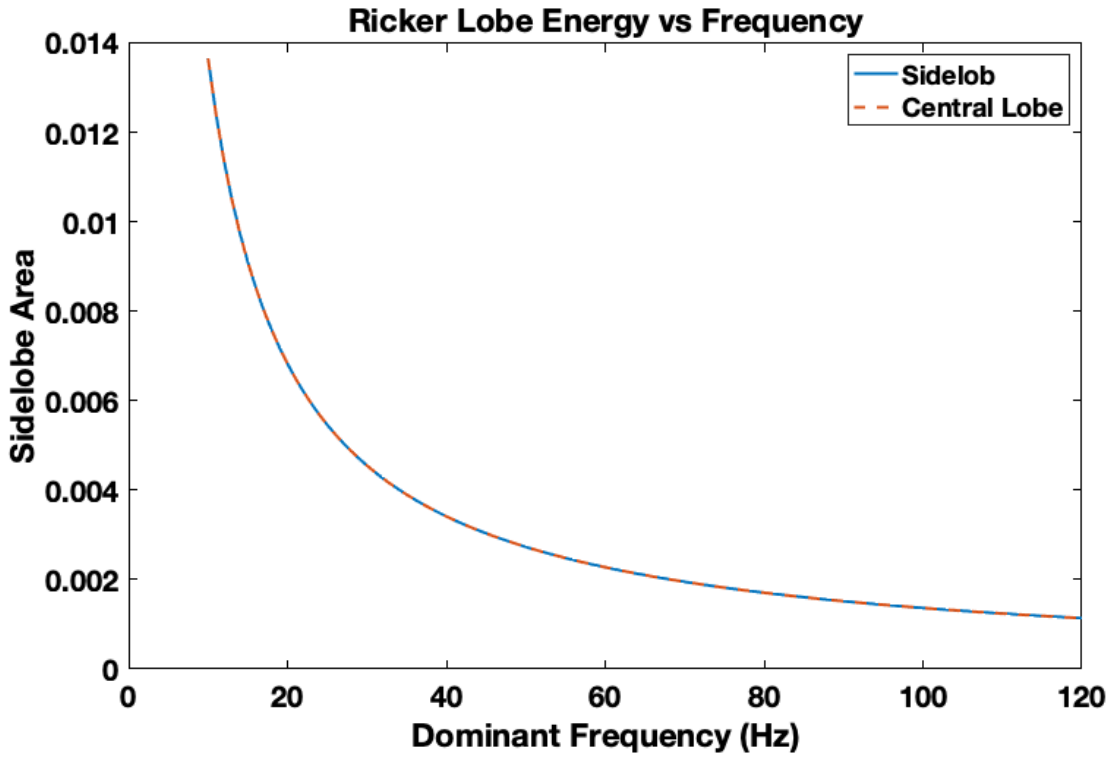

Figure 2.16 Plot of Ricker lobe energy (central lobe and sidelobe areas) versus frequency.

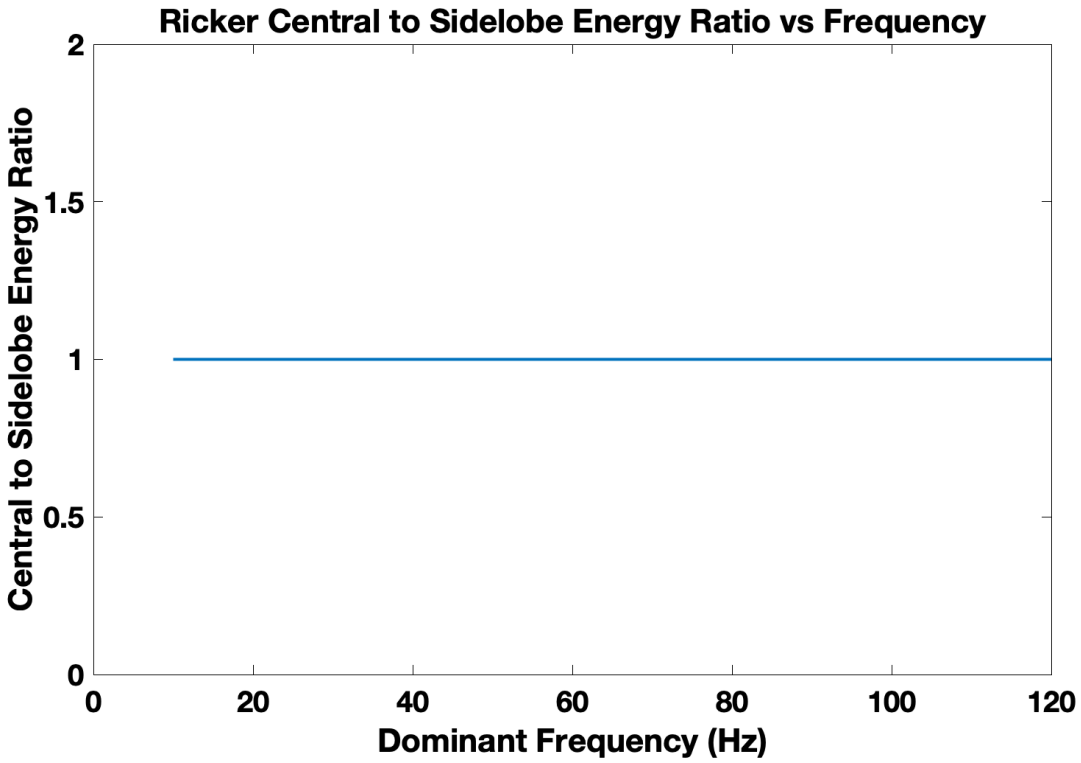

Figure 2.17 Plot of ratio of Ricker central to sidelobe area versus frequency.

2.2.6 Central to Sidelobe Energy Ratio (Klauder)

Following the format of the previous tests on the Klauder wavelet, evaluating the central to sidelobe energy ratio is also done by varying the terminal low frequency and terminal high frequency. Figure 2.18 shows the effect of changes in terminal low frequency with a variety of associated terminal high frequencies. As terminal low frequency decreases, the central to sidelobe energy ratio increases exponentially, similar to the trend seen in the analysis of peak to trough ratios with changing minimum terminal frequency in Figure 2.2. This finding follows what has been noted in published literature, low frequencies reduce sidelobe energy (ten Kroode et al., 2013; Karsh and Dondurur, 2013).

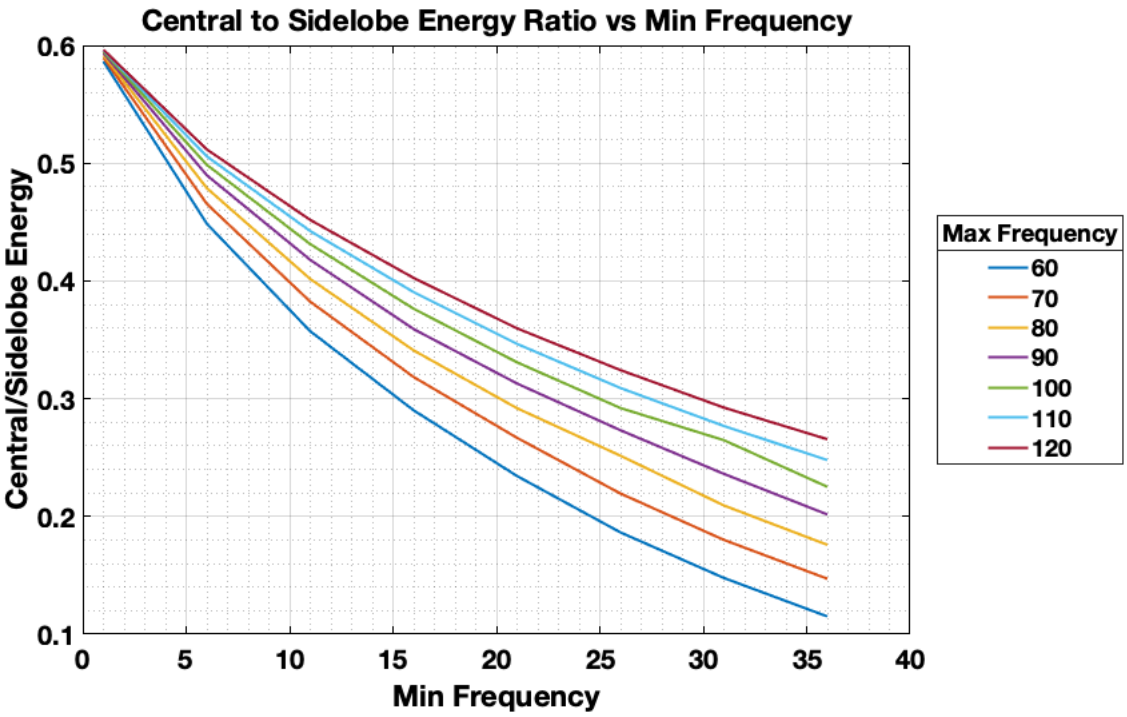

Figure 2.18 Plot of central to sidelobe energy ratio vs minimum frequency (Hz) for Klauder wavelets with several different maximum frequencies (Hz).

The effect of changing the terminal high frequency is shown in Figure 2.19. Upon observation, there is an obvious increase in central to sidelobe energy ratio with increasing terminal high frequency, however, the change in terminal high frequency has a much lesser impact on central to sidelobe energy ratio when compared to changing terminal low frequency. Furthermore, the effect of increasing the terminal high frequency diminishes when considering wavelets of decreasing terminal low frequency. This may be more apparent through observation of Figure 2.20, the central to sidelobe energy ratio versus both terminal low and terminal high frequencies. These findings, in agreement with the analysis of changing terminal low frequency, are comparable to the findings from the analysis of peak to trough ratio.

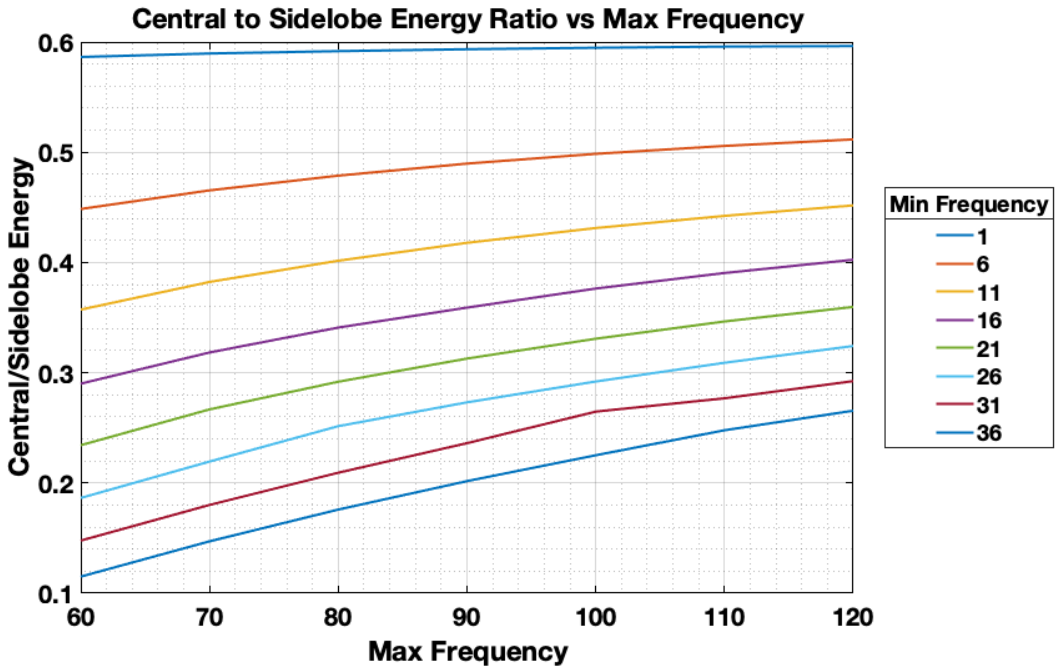

Figure 2.19 Plot of central to sidelobe energy ratio vs maximum frequency (Hz) for Klauder wavelets with several different minimum frequencies (Hz).

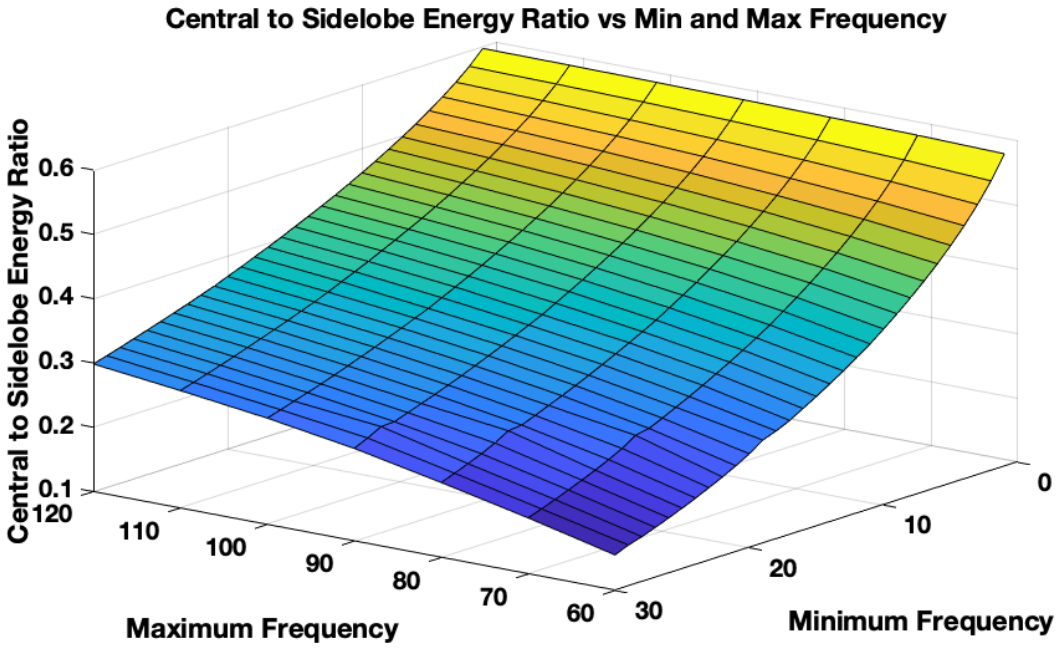

Figure 2.20 Plot of central to sidelobe energy ratio vs minimum frequency (Hz) and minimum frequency (Hz) for Klauder wavelets.

Finally, Figure 2.21 shows the relationship between central to sidelobe energy ratio and bandwidth in terms of octaves. As the bandwidth increases, the central to sidelobe energy ratio also increases with diminishing incremental gain in central to sidelobe energy ratio independent of either terminal high or terminal low frequency alone. From this plot and the previous analysis of terminal high and low frequencies independently, there are some notable observations. In literature, the presence and magnitude of sidelobes have been related to the amount of low-frequency content in a wavelet, however, Figure 2.21 shows that the central to sidelobe energy ratio is not directly dependent upon low frequency alone, but dependent upon total bandwidth in terms of octaves (Karslı and Dondurur, 2013). This seemingly contradictory finding can be explained through the definition of an octave as previously described in Section 2.2.2, (2.6. Since the number of octaves increases more quickly by lowering the terminal low frequency rather than increasing the terminal high frequency, a correlation to octaves of bandwidth describes a stronger dependence on terminal low frequency than terminal high frequency. Furthermore, the incremental increase in central to sidelobe energy ratio with octaves of band diminishes with increasing bandwidth. Therefore, there may be a point for which the effort or cost to obtain increased bandwidth, thereby increasing central to sidelobe energy ratio, cannot be justified by the incremental increase in central to sidelobe energy ratio.

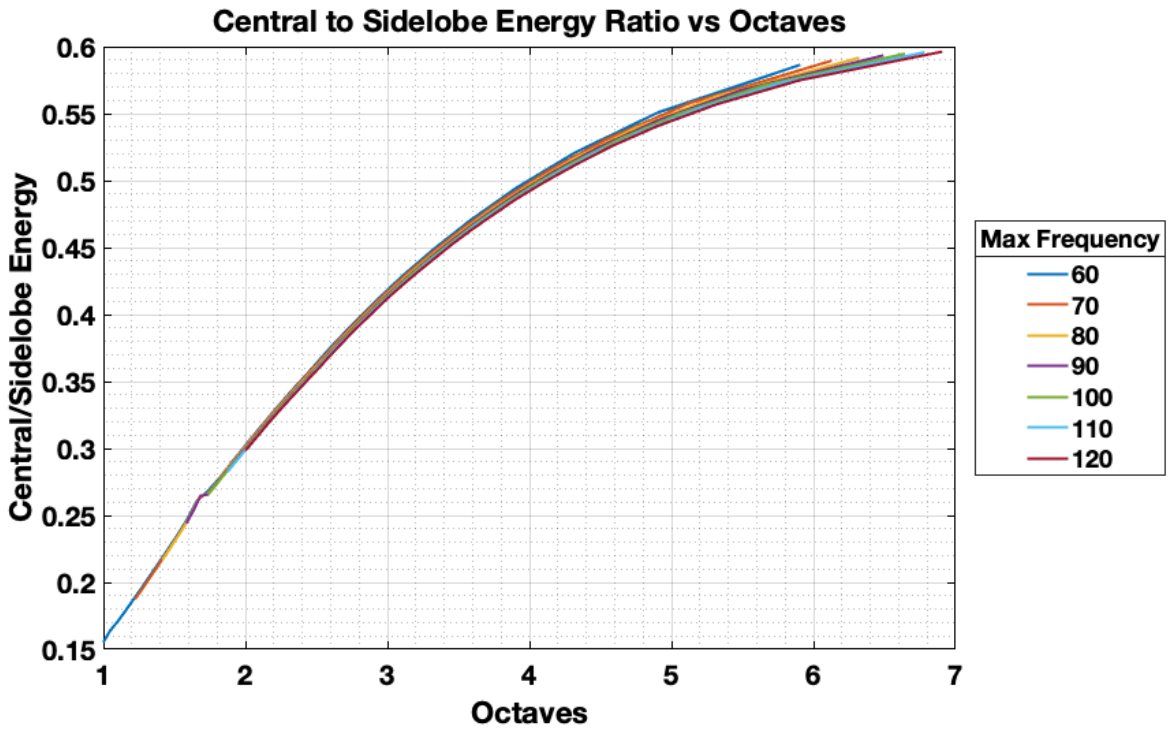

Figure 2.21 Plot of central to sidelobe energy ratio octaves for Klauder wavelets with several different maximum frequencies (Hz).

2.2.7 Wavelet Analysis Summary and Discussion (Ricker and Klauder)

The previous sections 2.2.1 - 2.2.6 comprise the entirety of the wavelet analysis undertaken in this thesis. Table 2-1 summarizes these findings with brevity for a simple review. While the analysis thoroughly investigated Klauder and Ricker wavelets in terms of the peak-to-trough amplitude ratio, central lobe width, and central to sidelobe energy ratio, there remains an opportunity for further analysis through the application of different synthetic sweeps, changes in phase, and addition of random noise.

In this analysis, the Klauder wavelets were generated using a 15-second linear synthetic sweep. In modern seismic acquisitions, extending the signal frequency toward low frequencies is often achieved through low-dwell or other non-linear sweeps (Jinping et al., 2018). The synthetic

wavelets can be further improved to model wavelets obtained in acquisitions by application of vibroseis mechanical constraints, especially as they influence phase and random noise. Further analysis with modern non-linear sweep design along with these additional variables may lead to slightly different results or a methodology to optimize vibroseis sweep for a particular seismic acquisition (Tellier and Ollivrin, 2019).

Table 2.1 Summary of Ricker and Klauder Wavelet analysis results.

	RICKER	KLAUDER
PEAK TO TROUGH AMPLITUDE RATIO	Constant peak to trough amplitude ratio ≈ 2.24.	Peak to trough amplitude ratio dependent upon octaves, not terminal high or terminal low frequency independently. Change in peak to trough amplitude ratio as a function of octaves is greatest at ≈ 2.7 octaves.
CENTRAL LOBE WIDTH	The central lobe width for Ricker wavelets, measured at zero crossings, follows the trend of the inverse of frequency. The central lobe width is slightly lower than f^{-1} due to the inclusion of more high-frequency content in a Ricker wavelet with a dominant frequency of f.	The central lobe width for Klauder wavelets, measured at zero crossings, is more strongly dependent upon terminal high frequency than terminal low frequency and, unlike peak to trough amplitude ratio, is not entirely dependent upon octaves.
CENTRAL TO SIDELOBE ENERGY RATIO	The central to sidelobe energy ratio is 1.	Central to sidelobe energy ratio is dependent upon octaves, not terminal high or terminal low frequency independently. Central to sidelobe energy ratio experiences diminishing growth with increasing bandwidth.

2.3 Penetration – Scattering and Absorption

2.3.1 Scattering

Scattering is a form of attenuation experienced by seismic waves due to interaction with heterogeneities in the Earth. The magnitude of scattering produced by an inhomogeneity is computed using the ratio of the size of the inhomogeneity to the wavelength (λ) as shown below in terms of wavenumber (k) (Ludwig-Maximilians-University, 2006).

(2.8)

$$k = \frac{2\pi}{\lambda}$$

$$k \times a \ll 0.01\ (quasi - homogenous\ medium) - \text{no significant scattering}$$

$$k \times a < 0.1\ (Rayleigh\ scattering) - \text{produces apparent Q and anisotropy}$$

$$0.1 < k \times a < 10\ (Mie\ scattering) - \text{ strong attenuation and scattering in the signal}$$

k can also be written in terms of frequency (f) and velocity (V) as shown below.

(2.9)

$$k = \frac{2\pi f}{V}$$

From the above form of the wavenumber formula and the conditions for the product of $k \times a$, the relationship between frequency and scattering is directly apparent. Considering a constant velocity (2500 m/s) and constant inhomogeneity sizes (5, 10, 20, and 40 meters) the magnitude of scattering

at each frequency can be seen in Figure 2.22. At lower frequencies, the value of $k \times a$ is always smaller than at higher frequencies, therefore, lower frequencies are less effected by scattering.

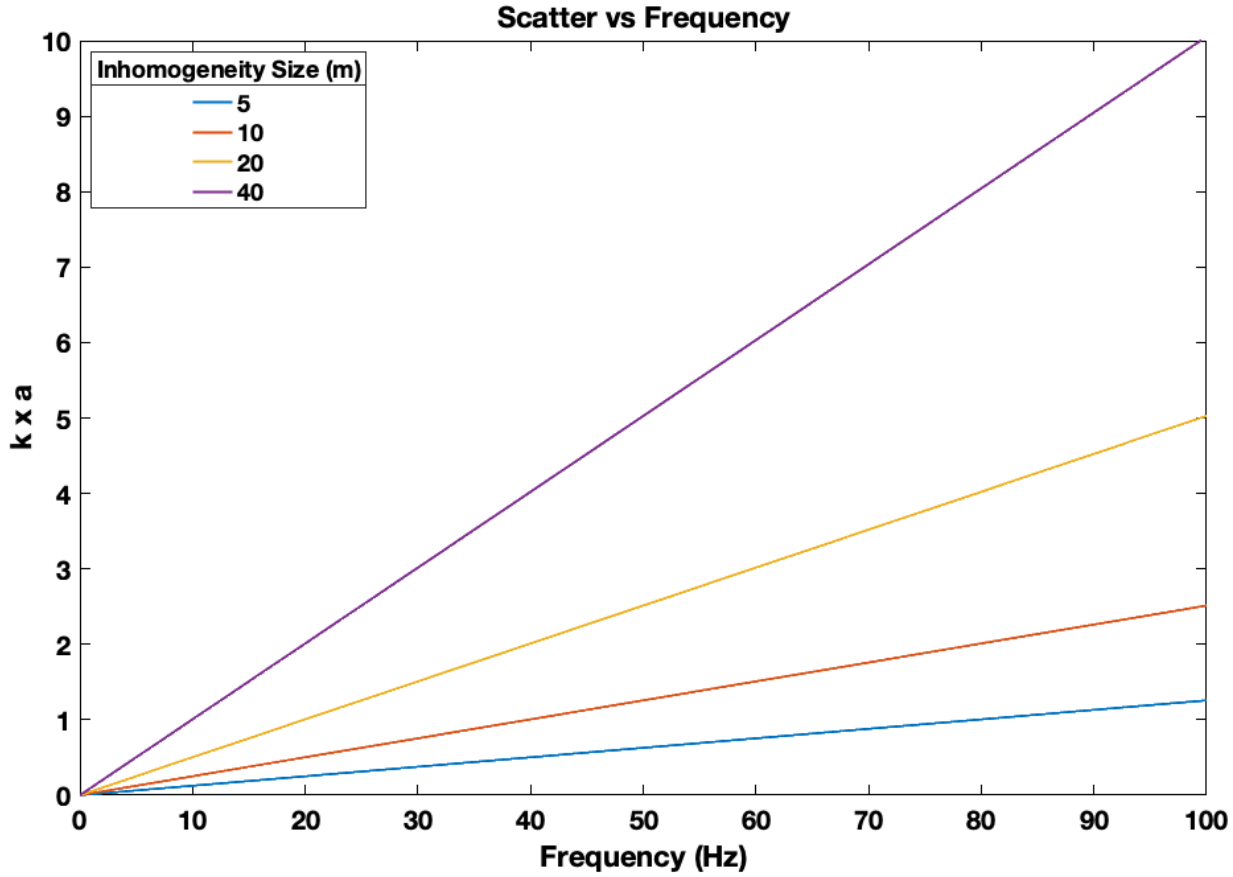

Figure 2.22 Plot of the product of $k \times a$, the indicator for the amount of scattering, versus frequency for constant velocity (2500 m/s) and several constant inhomogeneity sizes.

2.3.2 Intrinsic (Anelastic) Absorption

Elastic wave propagation consists of the permanent exchange between potential (displacement) and kinetic (velocity) energy. This process is not completely reversible due to energy loss from shear heating at grain boundaries, mineral dislocations, fluid interactions, and other energy sinks. Intrinsic absorption is the conversion of the elastic energy to the other forms

of energy (Padhy and Subhadra, 2013). In reflection seismology, the attenuation factor, which is often expressed as the seismic quality factor or Q (inversely proportional to the attenuation factor), quantifies the effects of intrinsic attenuation on the seismic wavelet (Toksöz et al., 1981). Q is defined as

(2.10)

$$Q = 2\pi\left(\frac{E}{\delta E}\right)$$

Where $\frac{\delta E}{E}$ is the fraction of energy that is lost per cycle. A general rule to seismic attenuation can be written as:

$$high\ frequencies - more\ oscillations - more\ attenuation$$

$$low\ frequencies - less\ oscillations - less\ attenuation$$

The typical values of Q are shown in Table 1.1. Synthetic modeling utilizing the CREWES toolbox function "einar" to generate a constant Q impulse response, based on Khartansson (1979) in MATLAB is shown in Figures 2.20-2.23. Figure 2.23 shows the wavelet at various times during propagation in a constant velocity medium with a Q value of 30, representative of shale, while Figure 2.24 shows the wavelet propagation in a constant velocity medium with a Q value of 58, representative of a sandstone. The associated amplitude spectra of the aforementioned figures are shown in Figures 2.21 and 2.22 respectively. While these synthetic demonstrations of intrinsic attenuation effectively convey the effect of different Q values on the wavelet, a more convincing

argument can be made by observation of amplitude spectra at different times in field data, as shown in Figure 2.27. Note that this case demonstrates pure mode, P-wave, attenuation. For further reading on converted mode attenuation refer to the Bale and Stewart (2002) publication of "The impact of attenuation on the resolution of multicomponent seismic data".

Table 2.2 Quality factor typical values for different rock types.

Rock Type	**Quality Factor**
Shale	30
Sandstone	58
Granite	250
Peridotite	650

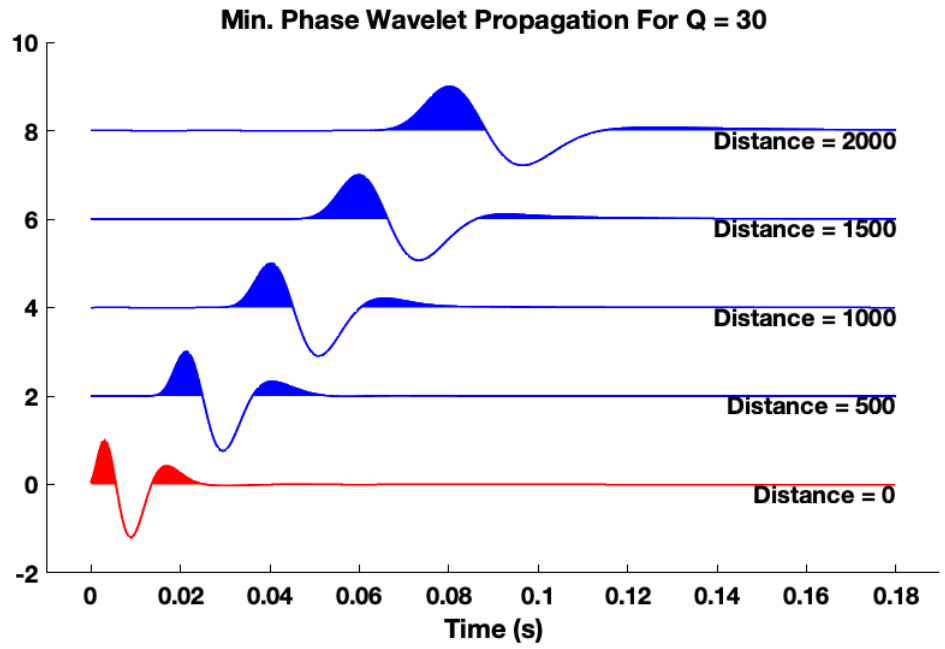

Figure 2.23 Plot of normalized minimum phase wavelet propagation in constant velocity medium (V=2000 m/s) with a Q value of 30.

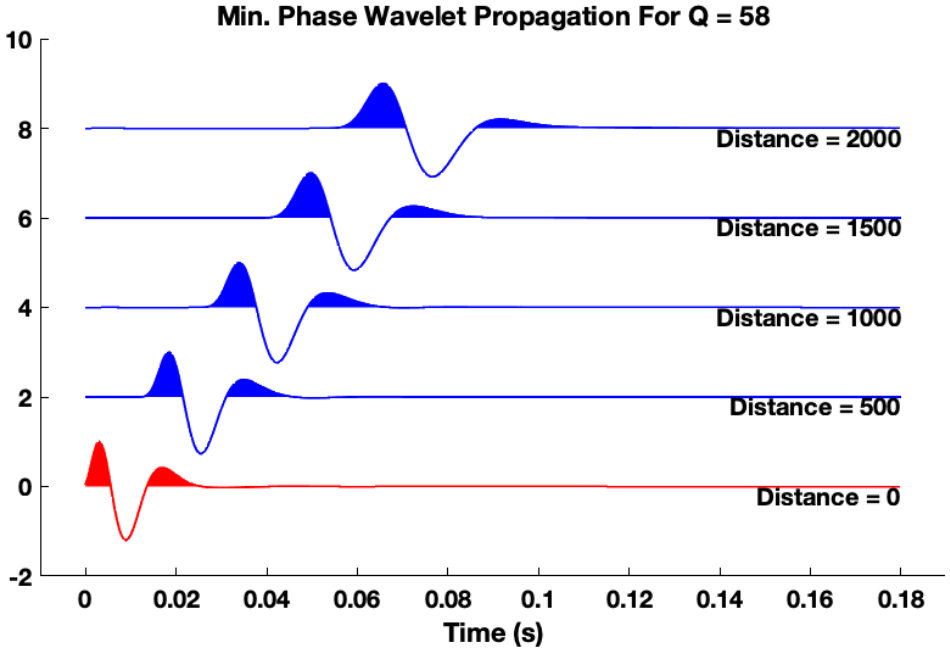

Figure 2.24 Plot of normalized minimum phase wavelet propagation in constant velocity medium (V=2000 m/s) with a Q value of 58.

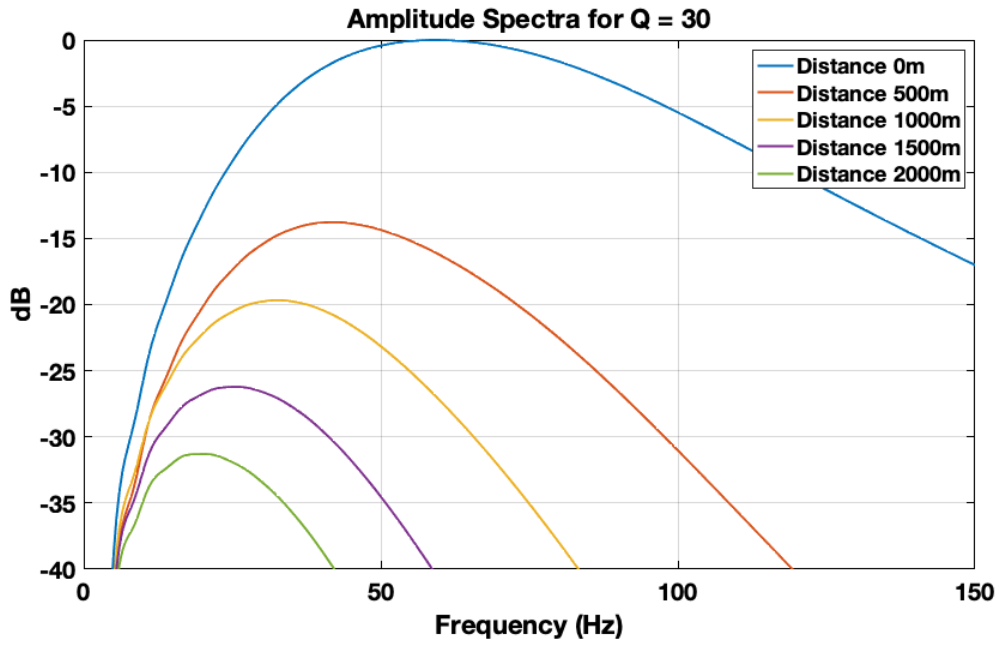

Figure 2.25 Plot of amplitude spectra corresponding to wavelets in Figure 2.20.

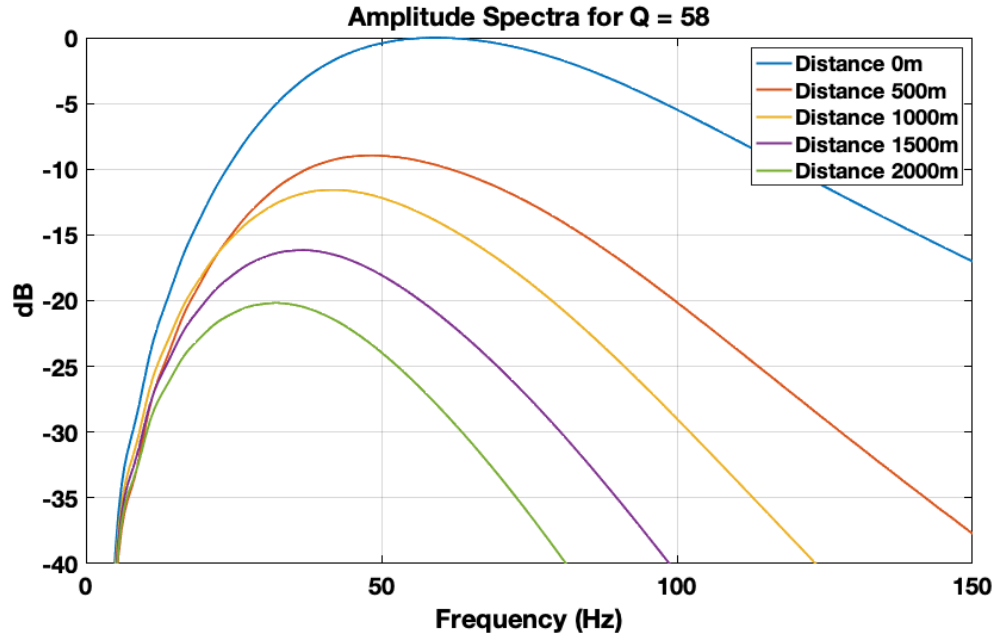

Figure 2.26 Plot of amplitude spectra corresponding to wavelets in Figure 2.22.

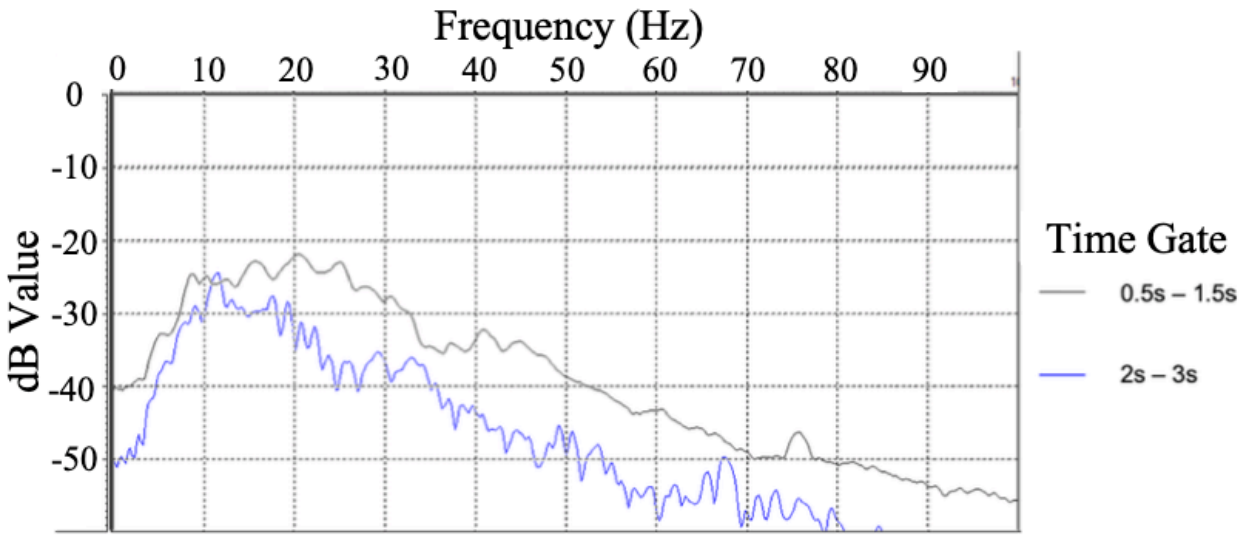

Figure 2.27 Plot of frequency spectra of raw HD2D data shot record at different time gates shows loss of high-frequency content at later times.

From the above synthetic and real data examples it is apparent that high frequencies are more subject to attenuation and, therefore, low frequencies have greater penetration. The advantage of this is that data with more low-frequency content will produce more coherent reflection events at greater depth or in the presence of more inhomogeneities than data without significant low-frequency content. Additionally, the effect of more coherent events aids in the velocity model building during processing which leads to a more accurate inversion product.

2.4 Impedance Inversion

One of the major difficulties with obtaining a reliable impedance inversion is creating an accurate low-frequency starting model (Kumar Ray and Chopra, 2016). In the traditional impedance inversion from band-limited seismic data, a low-frequency model must be obtained from low pass filtered impedance logs. For large exploration fields with sparse well logs or areas with exceptionally complex geology, the well-derived low-frequency model may not be accurate

which could propagate the error to the final inversion result (Dragoset and Gabitzsch, 2007; Michel et al., 2015). Case studies of the importance of low frequencies in impedance inversion are plentiful (see Smith et al., 1991; Martin and Stewart, 1994; Bergler et al., 2013; Michel et al., 2015), however, for breadth, the following impedance inversion using a well log from a well (Well A) located near the area of the seismic survey (HD2D) used in Chapter 4 serves to further demonstrate the importance of low frequencies. Figure 2.28 shows the P-wave velocity (m/s) computed from sonic and Density (km/m^3) in a section of Well A from approximately 900m to 1500m (the entirety of sonic and density log in well). The formation of interest is annotated on this well by the red line correlating to an increase in density and p-wave velocity, indicative of a carbonate, at roughly 1330m.

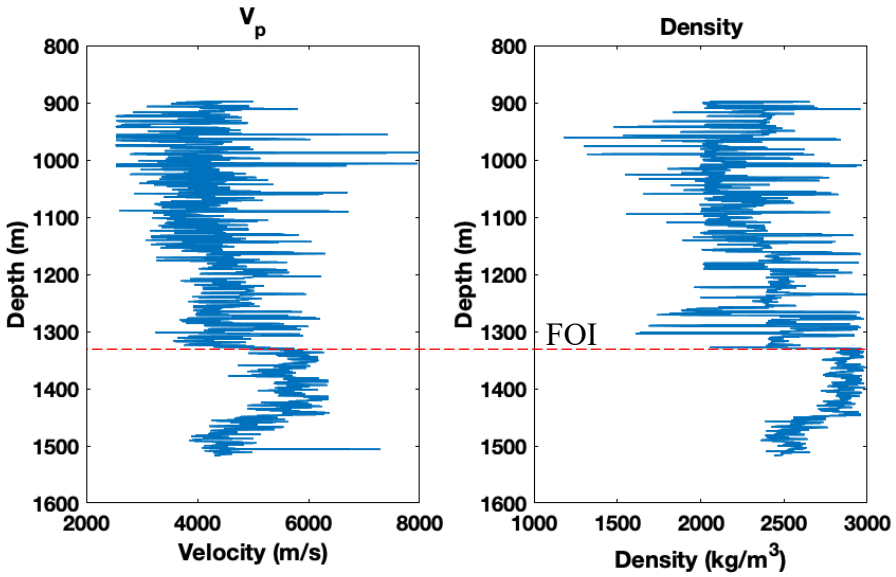

Figure 2.28 Plot of P-wave velocity log (m/s) from sonic (Left) and density log (kg/m^3)(Right) for Well A. The top of the formation of interest (FOI) is annotated by the red line.

These logs can then be converted into time and the impedance, the product of velocity and density, can be calculated at log sampling rate and the more sparse seismic sampling rate (in this case, an aggressive 1ms seismic sampling rate was applied). Next, a synthetic 1-D seismogram

must be computed. This is done by computing the reflection coefficients by taking the derivative of the log of impedance and convolving the resulting reflectivity series with a predetermined wavelet. After generating the synthetic 1-D seismogram, the impedance is calculated by (2.11).

(2.11)

$$imp = imp_0 * e^{2 * \int reflectivity}$$

Figure 2.29 shows the result of this exercise using a 0-.1-50-60 Hz low-frequency wavelet and a 5-10-50-60 Hz traditional wavelet to generate the synthetic seismograms. From inspection, it is apparent that the 0-60 Hz synthetic inversion follows the actual impedance seen in the well log much more closely than the 10-60 Hz synthetic inversion. Additionally, the greatest difference occurs when the acoustic impedance increases substantially at the FOI, which could lead to misinterpretation in the high-interest zone.

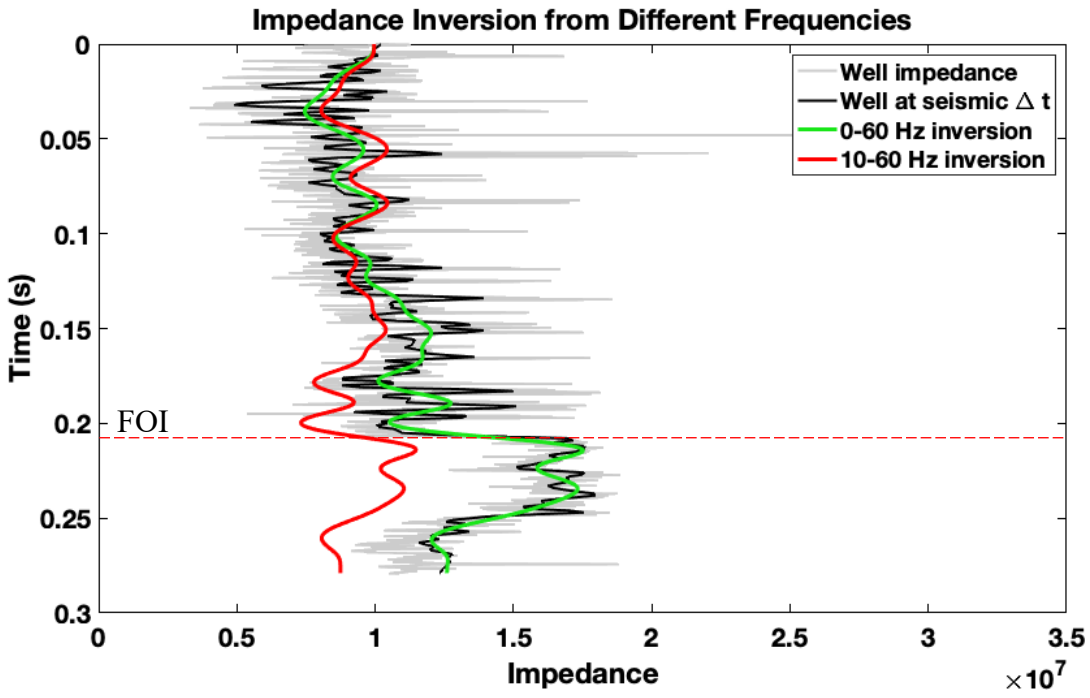

Figure 2.29 Plot of impedance calculated from Well A at log sampling rate and seismic sampling rate (0.001s), and impedance inversion from synthetic seismic created from the well log with different terminal low frequencies.

This deviation from the well derived impedance is seen more directly in Figure 2.30, the difference between the impedances inverted from the synthetic seismic and the well log computed impedance. As seen above, the difference between the well log computed impedance and the 0-60 Hz inversion remains low for the entirety of the log interval while the 0-60 Hz inversion begins to deviate around the FOI.

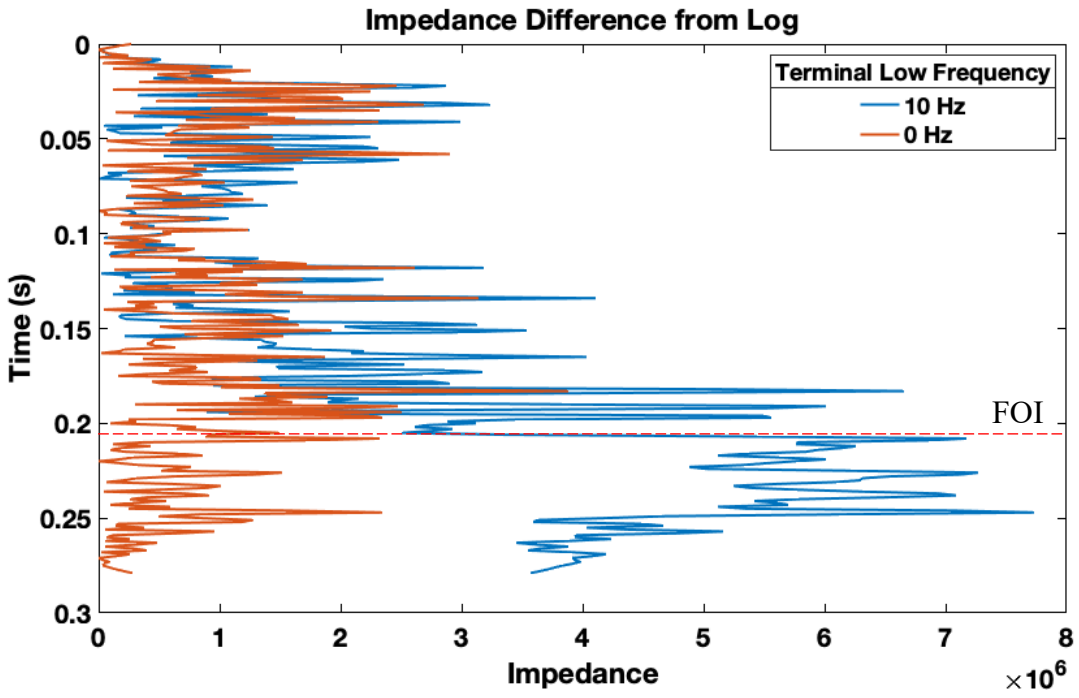

Figure 2.30 Plot of difference between impedance from inverted synthetic seismic with different terminal low frequencies.

After examination of the results of inversions of synthetic seismic with terminal low frequencies of 0 Hz and 10 Hz, there remains a question of how the inversion result changes within the 0-10 Hz terminal low-frequency range. Figure 2.31 shows the result of investigating the impedance inversion results of synthetic seismograms with different terminal low frequencies ranging from 0.1 Hz to 10 Hz. The inversion result of the synthetic seismogram with a terminal low-frequency of 0.1 Hz tracks very well with the well log derived impedance, however, increasing the terminal low-frequency to just 1 Hz creates noticeable deviation between the inversion result and actual impedance in Figure 2.32. Further increase in terminal low frequency continues this trend and the difference between well log derived and inversion derived impedance expands. Table 2.3 shows the average difference between the impedances from inversion and the well log through the entire log and from the top of the formation of interest to the end. The table again shows that

the average difference is less through the entirety of the log at a lower terminal low frequency and the average this is even more evident in the FOI.

This example of impedance inversion from a synthetic seismogram created using well data demonstrates the importance of low frequencies in impedance inversions and how lacking low frequencies can impact the result. In practice, most sources have difficulties generating frequencies below 5 Hz, with aggressive lower limits reaching 1.5 Hz, and most available receivers have corner frequencies of 10 Hz, with some more aggressive, less accessible, and more expensive options reaching below 5 Hz (Wei, 2018). Because of this, externally supplied trends are usually applied to fill the frequency gap (Martin and Stewart, 1994). Nonetheless, extending the terminal low frequency closer to zero gives a more confident, data-driven, inversion result.

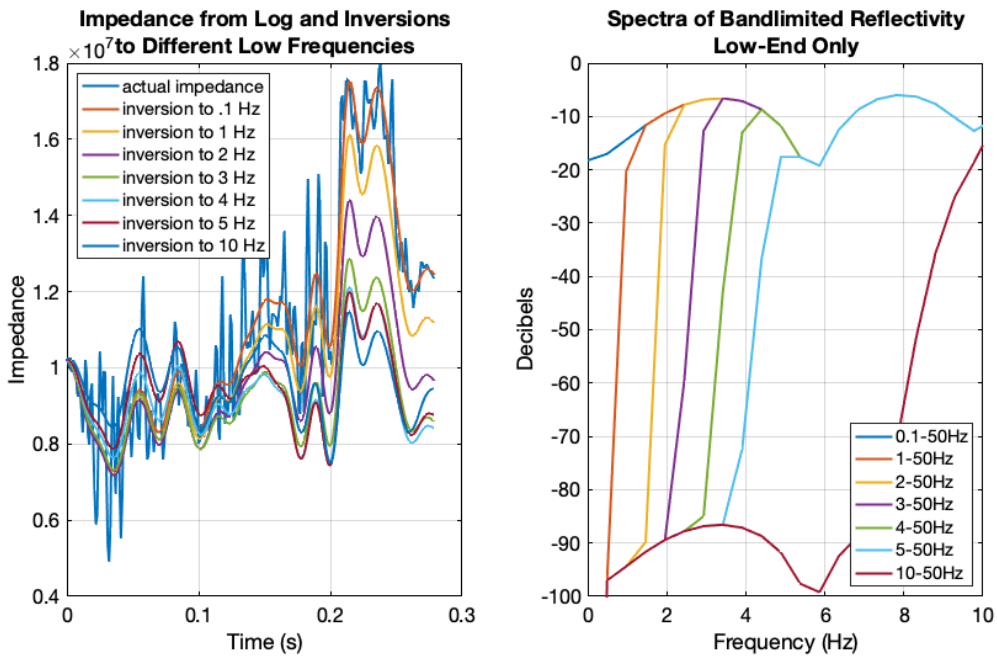

Figure 2.31 (Left) Plot of impedance from well log and synthetic seismic with different terminal low frequencies. (Right) Plot of low-end frequency spectra of synthetic seismic used for inversions in the plot on the left.

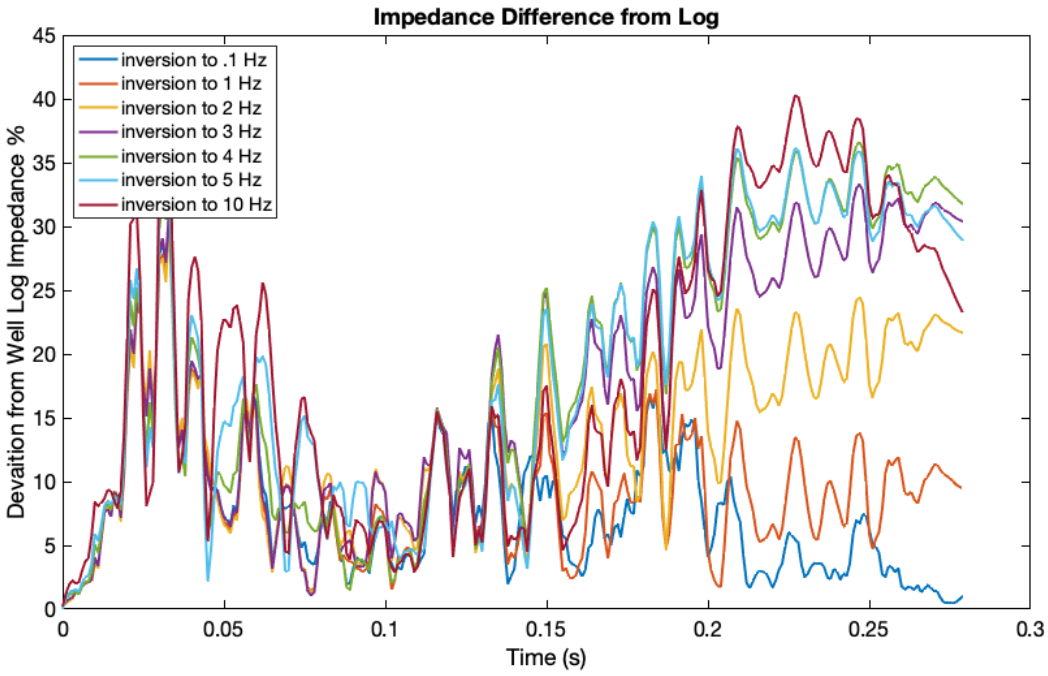

Figure 2.32 Plot of the percentage difference of impedance from inversion of synthetic seismogram with different terminal low-frequencies and well log derived impedance.

Table 2.3 Difference of impedance from inversion and well log

TERMINAL LOW-FREQUENCY (HZ)	AVG. DIFFERENCE OF IMPEDANCE FROM INVERSION AND WELL LOG (%)	AVG. DIFFERENCE OF IMPEDANCE FROM INVERSION AND WELL LOG (%) (STARTING AT FOI TOP)
0.1	7.57	3.63
1	9.10	8.77
2	13.40	19.46
3	17.30	28.42
4	18.70	31.89
5	19.02	31.36
10	18.76	32.53

Chapter 3: SEISMIC LATERAL RESOLUTION

3.1 Introduction

The lateral resolution of seismic data is the minimum lateral separation between two reflection events so that they can still be resolved individually. Lateral resolution is constrained by two main factors, one due to the physics of seismic reflections and the other being determined by the receiver spacing. To address the second, more elementary, constraint first, in the basic case of a flat-lying reflector, as seen in Figure 3.1, the horizontal sampling is equal to half the receiver spacing. If the receiver spacing (x) increases, the horizontal sampling will increase proportionately to $x/2$. Therefore, to achieve greater horizontal resolution, the receiver spacing must be kept small. Another noteworthy observation that can be drawn from Figure 3.1 is that the length sampled along the reflector ($s/2$) is half of the total receiver spread length (s) and the distance from the source and the first reflection point ($d/2$) is half of the distance between the source and the first receiver (d).

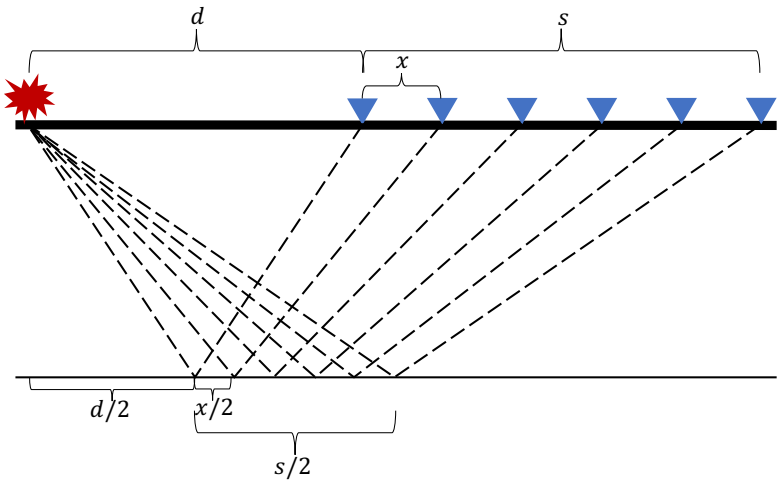

Figure 3.1 Seismic acquisition cross-section with a source (red), receivers (blue), and ray paths (dashed lines).

While decreasing the receiver separation does increase the sampling density and horizontal resolution, there is a limit of the achievable horizontal resolution as a consequence of the physics of seismic reflections. Figure 3.1 illustrates the paths between source and receiver as a simple ray path, however, the reality is more complicated.

While seismic reflections are often illustrated as ray paths, the seismic source does not create a single ray of energy, but rather a complicated wavefield. To more accurately describe the reflection process, consider the wavefield as it propagates through the subsurface. In the simple case of a flat reflector, the typical abstraction of the ray path is the line from the source to the point on the reflector that is first contacted by the source generated wavefield and back to the receiver. However, considering that the wavefield continues to propagate, as the wavefield comes in contact with the rest of the reflector, there are reflections generated in the form of a reflected wavefield that the receiver will also record. Simply put, reflected energy arriving at a receiver is the culmination of an infinite number of point scatterers on the reflecting surface. The limit of horizontal resolution in seismic data is a consequence of this fact. As shown in Figure 3.2 and Figure 3.3, the energy that arrives at a receiver within half a wavelength (or period) of the initial reflected arrival interferes constructively and indiscernibly. The area of the reflector from which this energy is returned is known as the first Fresnel zone, or more commonly just Fresnel zone. Around the first Fresnel zone are a series of concentric energy rings for which the energy interferes destructively and cancels out leaving just the first Fresnel zone of energy recorded at the receiver.

$v = rms\ velocity$

$t_0 = vertical\ two\ way\ time$

$f = frequency$

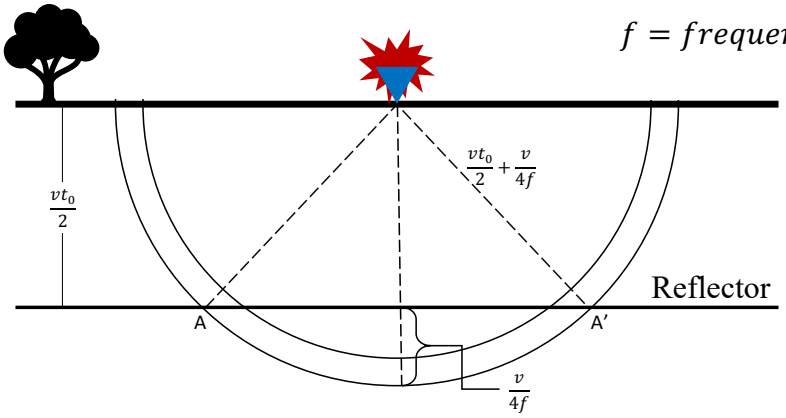

Figure 3.2 Schematic of zero-offset Fresnel zone. The blue triangle represents the receiver, red explosion represents the source. A tree is included for vertical reference.

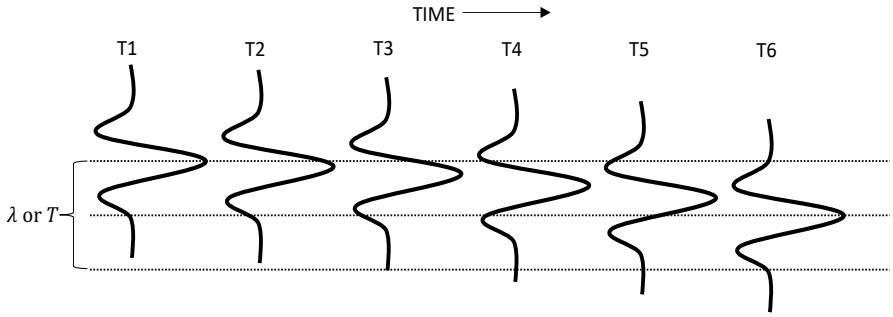

Figure 3.3 Representation of wavelets arriving at a receiver within a half a period or wavelength which would interfere constructively. This visualization can help comprehension of the constructive interference from reflections within a Fresnel zone.

For a simple zero offset case, the radius of the Fresnel zone ($\overline{AA'} = r_{fz}$) can be written as shown below.

(3.1)

$$r_{fz} = \sqrt{\frac{z_0\lambda}{2}} = \frac{V}{2}\sqrt{\frac{t_0}{f}}$$

Where z_0 is the depth to the target, λ is the wavelength, V is the seismic velocity, t_0 is the zero-offset travel time, and f is the frequency. The more complicated, yet accurate Fresnel zone equations accounting for offset, published by Monk (2010), are below.

(3.2)

$$\perp \; to \; shot - receiver \; axis: Y_F = \frac{V}{2}\sqrt{t_f^2 - t_0^2 - \frac{4h^2}{V^2}}$$

(3.3)

$$\parallel \; to \; shot - receiver \; axis: X_F = \frac{t_f V}{2}\sqrt{1 - \frac{t_0^2 V^2}{t_F^2 V^2 - 4h^2}}$$

Where,

(3.4)

$$t_f = t_x + \frac{\tau}{2}$$

(3.5)

$$t_x = \frac{2}{v_{rms}}\sqrt{\left(\frac{h}{2}\right)^2 + \left(\frac{t * v}{2}\right)^2}$$

$$t_o \text{ is zero} - \text{offset traveltime}; \quad 2h \text{ is source/receiver offset}$$

This derivation accurately represents the Fresnel zone, in terms of inline and crossline component, as an ellipse for source-receiver offsets greater than zero.

3.2 Fresnel Zone Marine Application

The offset Fresnel zone application has great value in marine seismic acquisition, specifically, in marine seismic infill decisions. In the marine environment, seismic sources and streamers experience "feathering" where they are moved unpredictably by ocean currents. This movement results in less than perfect surface-derived CMP coverage leaving empty or low-fold bins requiring additional "infill" acquisition to achieve a contiguous dataset. The process of infilling these holes is often very costly. Historically, the cost of infill in a marine seismic acquisition can be as much as 25% or more of the total cost of prime seismic acquisition (Monk, 2010). Taking a typical marine prime seismic line acquisition of 50 days, for example, at an average day-rate of $300k/day, that amounts to as much as 13 days and $3,750,000 of infill acquisition (Figure 3.4). Along with the significant monetary drive to reduce time acquiring infill sequences, there is a benefit of shortened exposure to safety risks associated with the acquisition and decreased cycle time to deliver, interpret, and act on the data.

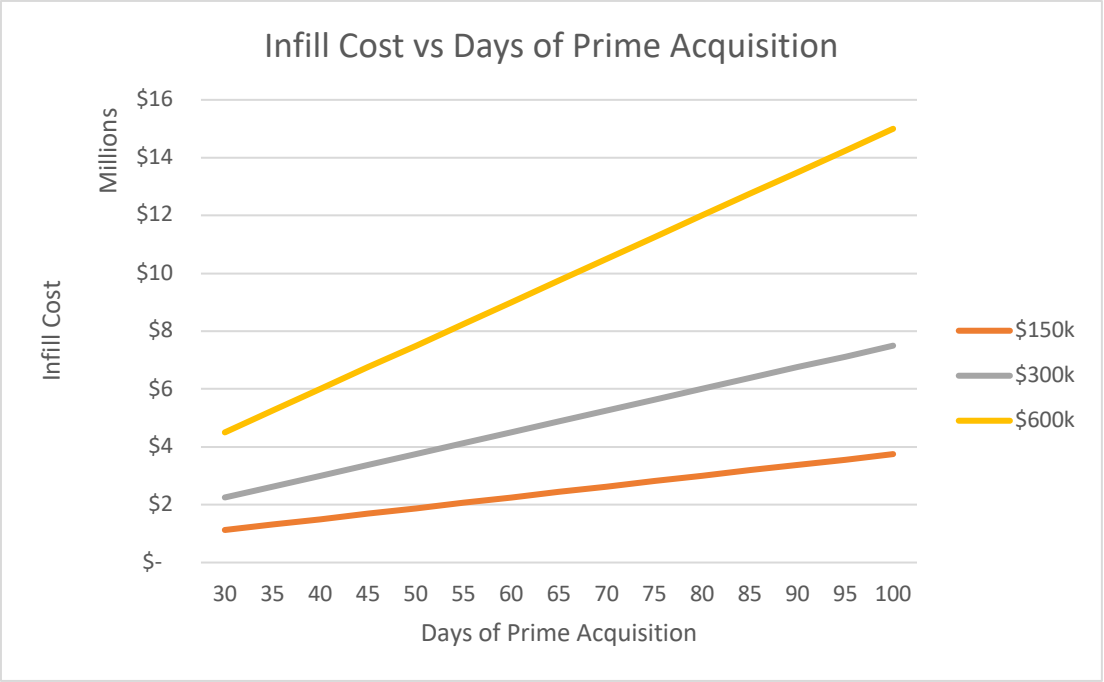

Figure 3.4 Plot of infill cost estimate vs days of prime acquisition for three different day rates following the assertion that historically the cost of marine infill acquisition can be as much as 25% or more of the total cost of prime seismic acquisition from Monk (2010).

Infill decisions for marine seismic were traditionally made based upon two main factors: the size of the missing data area, and its proximity to a reservoir or other high value-areas. These decisions utilized expanded bin coverage ("Flexed bin") maps to highlight areas of exceptionally poor coverage. These maps would allow the bins to count shots whose midpoints were within a defined expansion factor of the center of each bin. For example, consider a bin with 0 fold between 2 bins that had 20 fold. If the expanded map allowed for 100% expansion, the bin that had 0 fold originally would appear to now have 40 fold. These maps were visual tools that helped offer insight into when full coverage could be reasonably interpolated to fill in small coverage deficiencies during processing. Presently, integration of geology and geophysics into marine seismic infill evaluations is achieved through Fresnel zone calculations and forward modeling.

3.2.1 Forward Modeling

Day and Rekdal (2005) provided a method for predicting the effects of coverage holes on a migrated image by synthetic modeling followed by pre-stack time migration. These modeled results, given in terms of amplitude and time-shift, can then be used to assess infill requirements based on a predetermined level of data quality degradation. One significant advantage of this method is that it may be performed in the survey planning stage rather than during or after the acquisition. Determining infill requirements at this stage allows for clarity in contracts and saves time on evaluations that could delay further acquisition in the field.

The method Day and Rekdal provide, as mentioned previously, is based upon time and amplitude shifts of PSTM models as shown in Figure 3.5 and Figure 3.6 respectively and Appendix B. The issue with relying on this method is two-fold. First, the time shift realized from this method is typically less than a few milliseconds, which, at an aggressive 2ms sample rate, amounts to as little as a one-sample time shift for a hole size of 140m. Second, the PSTM model does nothing to compensate for the area of little or no data that results in the amplitude difference. In processing today, many modern tools can be used to compensate for this.

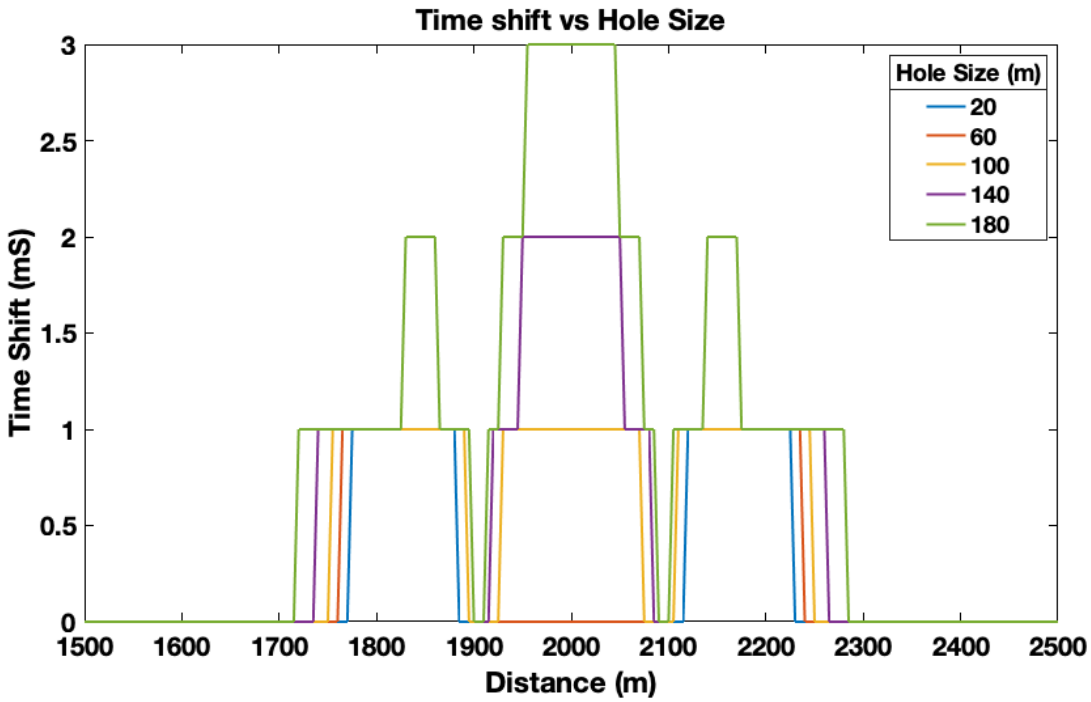

Figure 3.5 Plot of time-shift versus hole size plot for migration forward modeling.

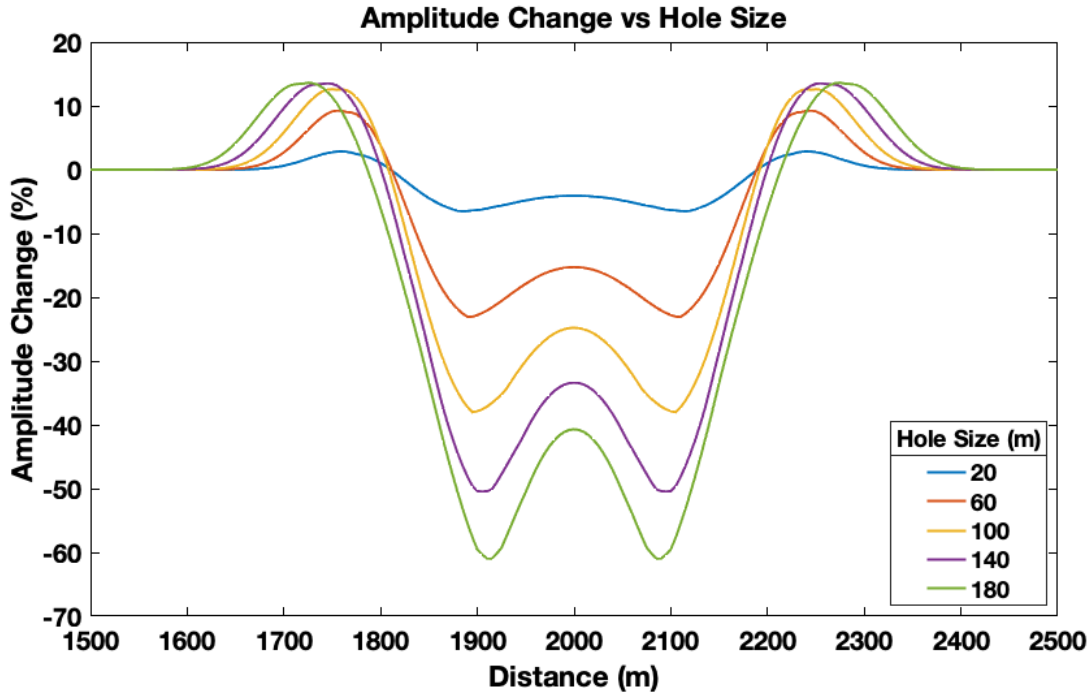

Figure 3.6 Plot of Amplitude change versus hole size for migration forward modeling.

While the Day and Rekdal method for analyzing infill opportunities has been used in the industry for a several years, it does not account for the advanced processing techniques being applied today. However, another method exists in the form of Fresnel zone infill analysis based purely on the physics of the reflection rather than processing techniques.

3.2.2 Fresnel Zone Infill Analysis

The technique of Fresnel zone infill analysis is based upon the fact that the area of illumination on a reflector is much larger than the size of CMP bin used to account for a given ray-path in many cases. As noted in Section 3.1, the area that contributes to a reflection event along a horizon is not the reflection of energy at a single point, but the reflection within the Fresnel zone. Additionally, because in the marine environment the inline sampling is much denser and more consistent than crossline sampling, the only dimension of the Fresnel zone that is of concern for infill evaluation is the crossline dimension. A major benefit of this form of infill analysis is that, like the PSTM forward modeling method, it can be done presurvey based upon knowledge of the geology and, unlike the PSTM method, it can be done with very little computation. An example of the process of Fresnel zone infill evaluation is included in APPENDIX C. This process lacks the consideration of a simple component of the survey, crossline offset. The MATLAB code in APPENDIX D and APPENDIX E was written to visualize the dimensions of a Fresnel zone and test the influence of crossline offset on Fresnel zone size. The code in APPENDIX D required the derivation of the Fresnel zone ellipsoid. Geometrically, the ellipsoid is as shown in Figure 3.7 and Figure 3.8.

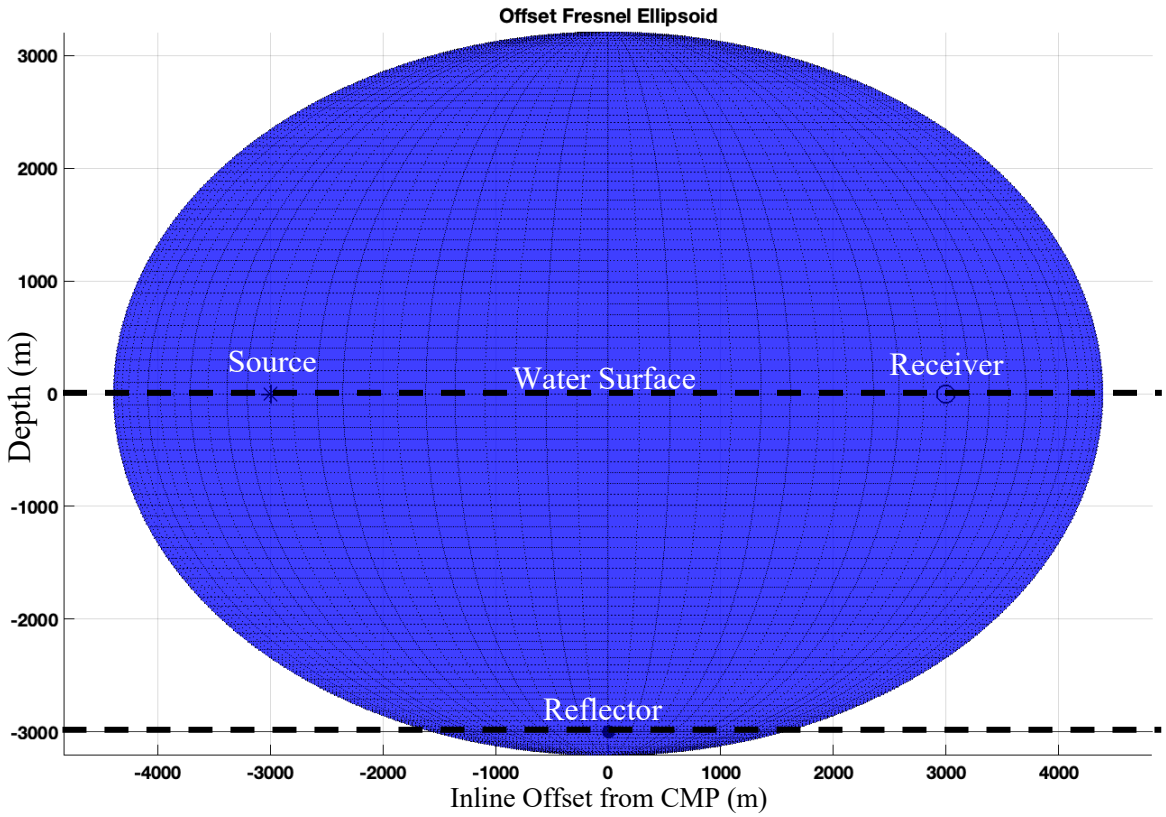

Figure 3.7 Plot of Fresnel Ellipsoid from view across crosslines.

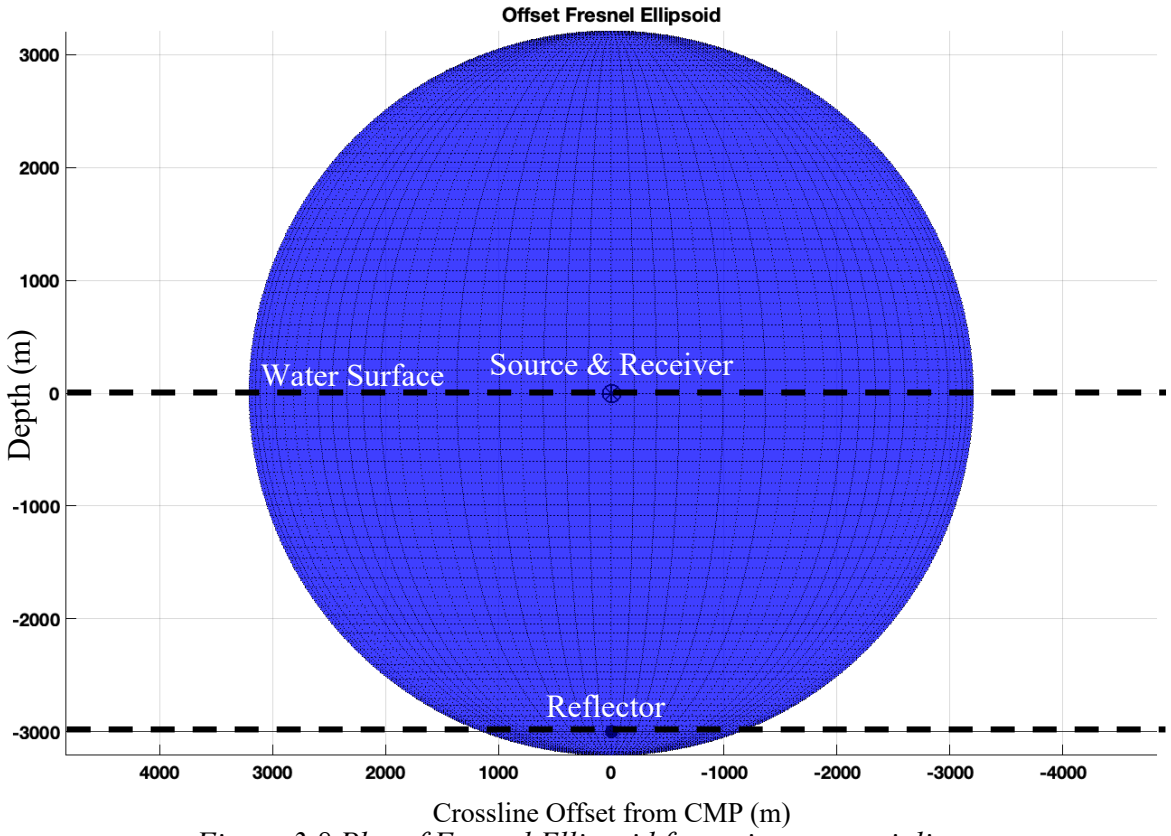

Figure 3.8 Plot of Fresnel Ellipsoid from view across inlines.

In equation form, this ellipsoid is expressed as:

(3.6)

$$\frac{(x*\cos(\theta)+y*\sin(\theta))^2}{\left(\frac{V}{2}*\left(\sqrt{t_0^2+\frac{2h^2}{V^2}+\frac{1}{2f}}\right)\right)^2-h^2}+\frac{(y*\cos(\theta)+x*\sin(\theta))^2}{\left(\frac{V}{2}*\left(\sqrt{t_0^2+\frac{2h^2}{V^2}+\frac{1}{2f}}\right)\right)^2}$$

$$+\frac{z^2}{\left(\frac{V}{2}*\left(\sqrt{t_0^2+\frac{2h^2}{V^2}+\frac{1}{2f}}\right)\right)^2-h^2}=1$$

Where,

$$x = crossline\ dimension;\ y = inline\ dimension;\ z = depth;$$

$$\theta = offset\ angle = \operatorname{atan}\left(\frac{crossline\ offset}{inline\ offset}\right);\ t_0 = zero\ offset\ traveltime;$$

$$V = rms\ velocity;\ f = frequency;\ h = \frac{inline\ offset}{2}$$

This Fresnel zone ellipsoid represents all points in three-dimensions for which the reflection time differs by half a period of the original reflection which occurs at a depth z directly beneath the midpoint of the source and receiver. Intersecting this ellipsoid with a plane at a depth of z gives the two-dimensional ellipse of the Fresnel zone.

To determine the influence of crossline offset, the lateral offset of the receiver was varied and the change in Fresnel zone radius was calculated. The results of this exercise can be seen in Figure 3.9, Figure 3.10, and Figure 3.11. Since there are many variables to consider, the end

member cases were compared, a near offset, shallow reflection (Figure 3.9), and a long offset, deep reflection (Figure 3.10). The inputs to these end-member cases are summarized in Table 3.1. A crossline offset range from 0 to 400m was chosen to over-analyze lateral offsets for a marine seismic acquisition array of 14 streamers with 50m spacing (325m on each side of the center). Figure 3.9 and Figure 3.10 are plots of the FZ diameter calculated using the OFZ function from 1.1.1APPENDIX D with varying inline and lateral offset, the David Monk (2010) crossline Fresnel zone equation with varying inline offset, and the zero offset Fresnel zone equation.

Table 3.1 Variable Inputs for FZ calculations in Figures 3.9-3.10.

	NEAR/SHALLOW (FIG. 3.9)	**FAR/DEEP (FIG. 3.10)**
TIME (S)	2	5
FREQUENCY (HZ)	80	30
RMS VELOCITY (M/S)	1500	2100
INLINE OFFSET (M)	1000	12000
LATERAL OFFSET (M)	0 - 400	0 - 400

The near offset and shallow reflector scenario in Figure 3.9 shows that the Fresnel zone crossline diameter grows rapidly when considering lateral offset. At the point of maximum lateral offset the Fresnel zone crossline diameter is 153.4m without consideration for lateral offset and 176.6m when accounting for lateral offset. This difference, 23.2m, is approximately 15% of the size of the Fresnel zone crossline diameter. While this additional 23.2m of Fresnel zone crossline diameter is smaller than the crossline bin dimension in this configuration, the improved accuracy would contribute to more confident Fresnel zone infill decisions. This is especially true because

the majority of infill occurs between sail lines where the lateral offset is at a maximum. Without consideration for lateral offset, in this scenario, an overly conservative infill evaluation may be carried out.

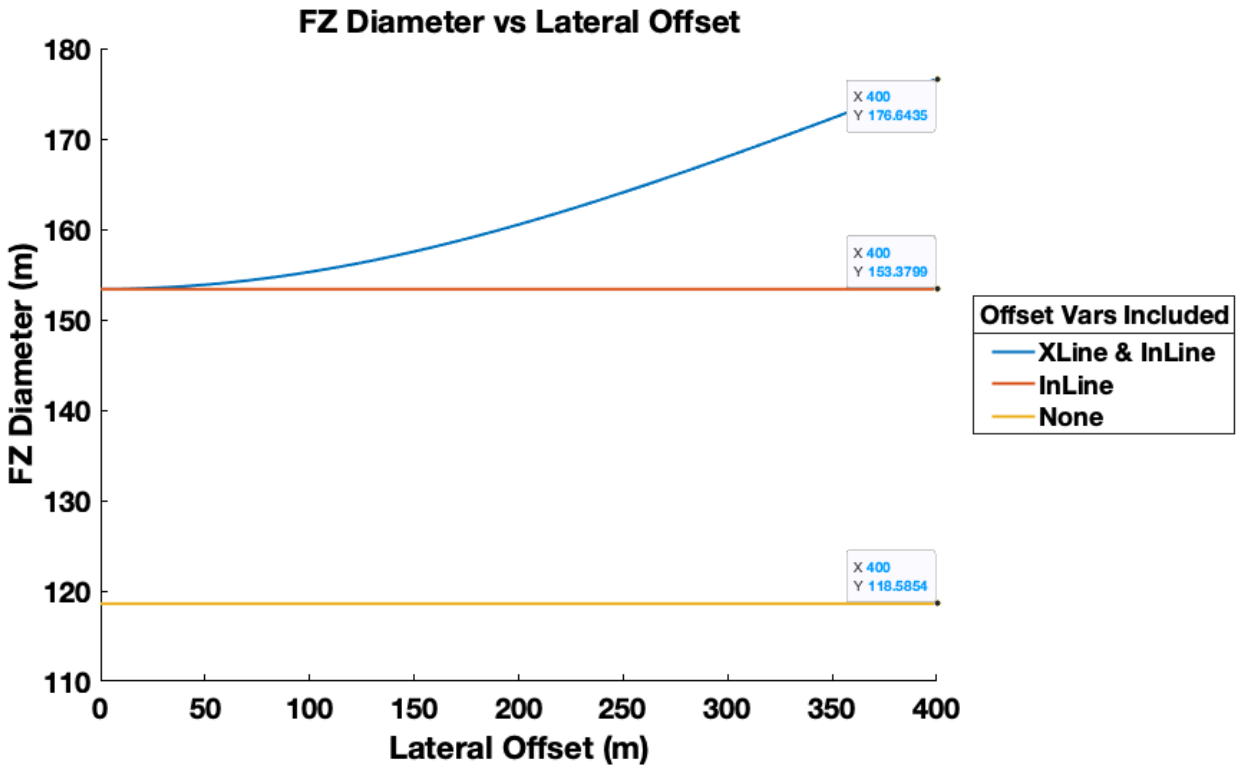

Figure 3.9 Plot of Fresnel zone crossline diameter versus lateral offset for near offset (1000m) and shallow reflector (t=0.5s, v=1500 m/s, f=80 Hz).

The far offset and deep reflector scenario in Figure 3.10 shows that the Fresnel zone crossline diameter grows much more slowly than in the previous, near offset and shallow reflector, scenario. In this case, accounting for lateral offset only increased the Fresnel zone crossline diameter by 1.3m, or 0.1%. Since the angle between the source and the receiver becomes much smaller with longer offsets, the longer offsets are not influenced by lateral offset as much as the

short offsets. For the case of long offset infill analysis, consideration of lateral offset is not necessary.

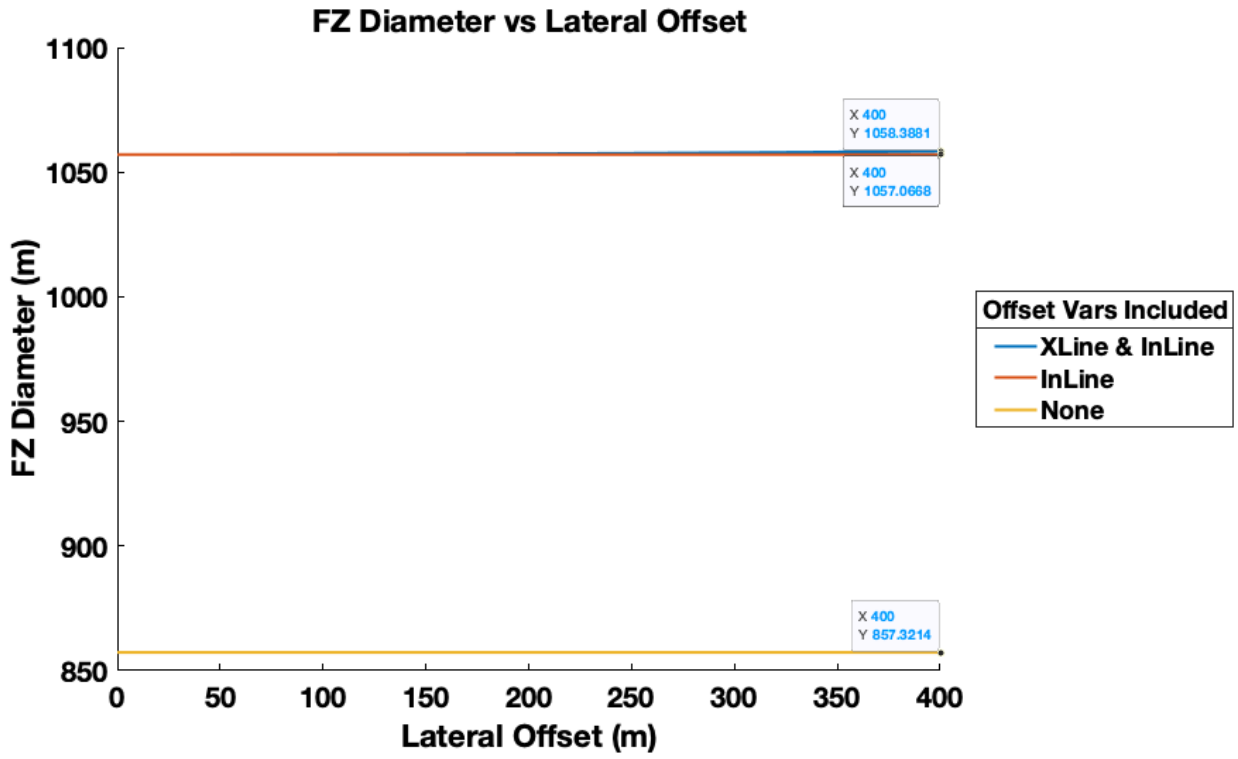

Figure 3.10 Plot of Fresnel zone crossline diameter versus lateral offset for Far offset (12000m) and deep reflector (t=5s, v=2100 m/s, f=30 Hz).

The difference between the Fresnel zone crossline diameters calculated with and without lateral offset for both the near/shallow and far/deep scenarios is shown in Figure 3.11. From this plot, it is clear that the lateral offset has a much greater effect on the Fresnel zone crossline diameter for the near offset and shallow reflector scenario compared to the far offset and deep reflector, which further substantiates the findings that consideration of lateral offset is only necessary to consider in short offset.

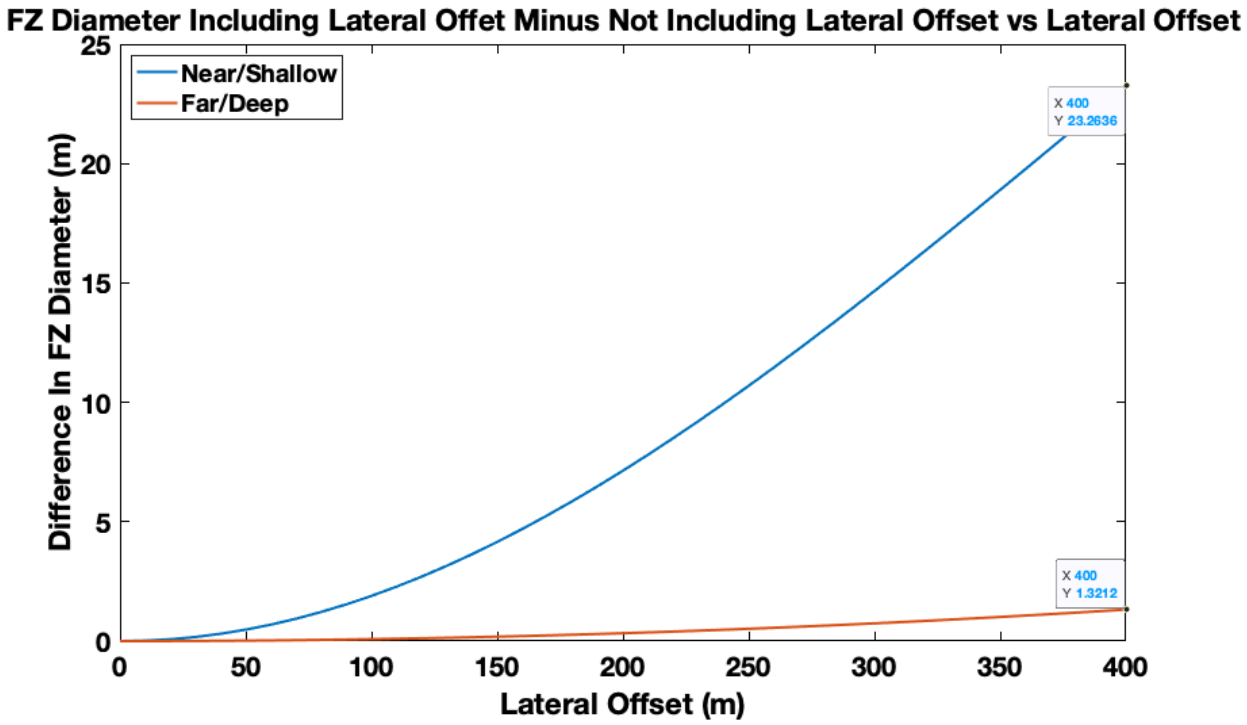

Figure 3.11 Plot of the difference between Fresnel zone crossline Diameter computed with and without lateral offset versus lateral offset for a near offset and shallow reflector scenario and a far offset and deep reflector scenario.

There are situations, however, where lateral offset may be more important. Examples of these include the marine wide azimuth, ocean-bottom node, ocean bottom cable, and land-based surveys. Today, Fresnel zone binning, a novel application of a Fresnel zone ellipse with the weighted contribution to sampling in encompassed bins, is applied in many cases to determine adequate subsurface sampling (Monk and Young, 2009).

A further application of Fresnel zone binning can consider taking the low-frequency limit of the acquired data to determine the adequacy of low-frequency coverage. This application is useful when acquiring a seismic survey with sparse sampling of low frequencies through the use of specialized low-frequency sweeps or low-frequency geophones alongside a conventional seismic acquisition. Significant monetary savings can be realized by reducing the number of more

expensive low-frequency geophones that must be deployed to obtain an adequately sampled low-frequency dataset.

Chapter 4: HD2D FIELD DATA

4.1 Introduction

The acquisition of broadband seismic data is primarily constrained by two mechanisms, the source and the receiver (Maxwell and Lansley, 2011; Winter et al., 2014). The HD2D dataset, acquired by Apache Corporation in January 2017 and generously provided to the University of Houston for use in research projects, lends itself well to the analysis of the source and receiver contributions to extending bandwidth. As described in sections 1.2 and 1.3, this 2D seismic line is comprised of five different types of nodal geophones (Table 1.1) and four different vibroseis source sweeps/configurations. Of the available source and receiver combinations, this research will focus on the data from the FairfieldNodal ZLand and GoK Low-Frequency receivers acquired with the two vibroseis 15-second linear sweep. From this combination, the influence of extended bandwidth gained by utilizing a low-frequency receiver as opposed to a conventional receiver can be analyzed.

This chapter begins with a basic introduction to geophones to familiarize the reader with the mechanics of a geophone and how the resonant frequency changes the output frequency spectrum. Next, the frequency spectra of the conventional and low-frequency geophones are compared from the HD2D line. Then, a simple overview of the processing flow used on each dataset is explained. Finally, frequency spectra and filter panels from the final processed data are compared to determine the difference in low-frequency content in each final dataset. This chapter will conclude with commentary on the significance of the difference in low-frequency content and possible implications for future monitor surveys.

4.2 Geophones

Geophones are highly sensitive ground motion transducers based on an inertial mass (proof mass) suspended on a spring that has been used by seismologists and geophysicists for decades (Brazilai, 1999; Hons, 2008). Modern geophones consist of a magnet fixed to the case with a wire coil as the proof mass as seen in Figure 4.1.

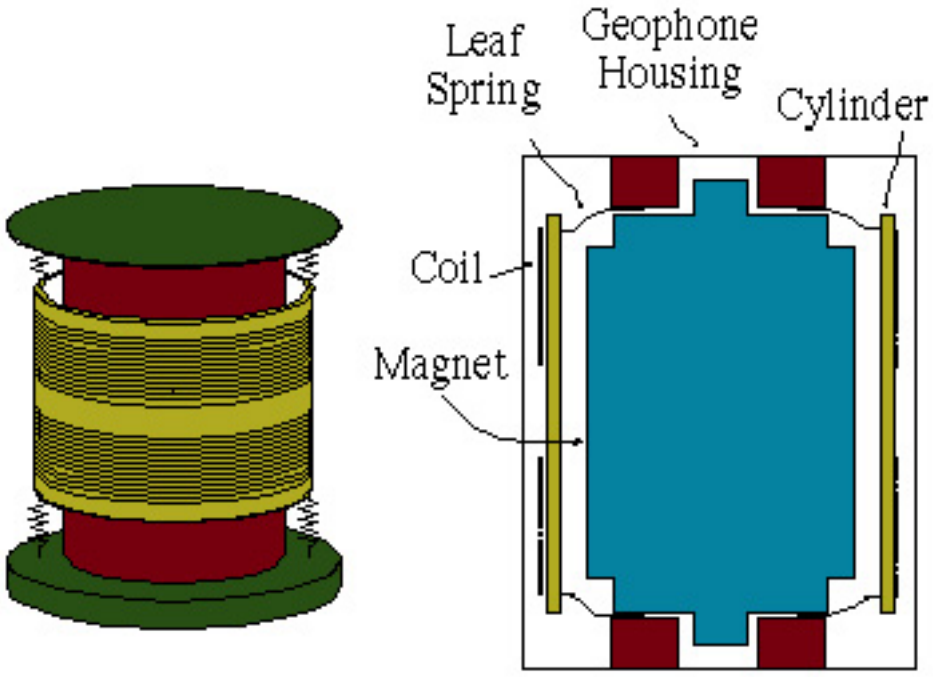

Figure 4.1 An isometric and cross-section view of a geophone. (Barzilai, 1999)

The geophone uses electromagnetic induction to transform the velocity of the proof mass relative to the case into voltage according to Faraday/Lentz Law ((4.1) where v is voltage and x is the displacement of the magnet relative to the coil. Therefore, the recorded values of a geophone are the velocity of the magnet relative to the coil multiplied by a sensitivity constant ((4.2).

(4.1)

$$v \propto \frac{dx}{dt}$$

(4.2)

$$v_g = S_g \frac{\partial x}{\partial t}$$

The forced simple harmonic oscillator equation ((4.3) describes the displacement of the ground (u) relative to its undisturbed position in terms of displacement of the proof mass relative to the case (x), the damping ratio (λ) and the resonant frequency (ω_0).

(4.3)

$$\frac{\partial^2 x}{\partial t^2} + 2\lambda\omega_0 \frac{\partial x}{\partial t} + \omega_0^2 x = \frac{\partial^2 u}{\partial t^2}$$

In the frequency domain, this equation can be written as:

(4.4)

$$X(\omega) = \frac{-\omega^2}{-\omega^2 + 2j\lambda\omega_0\omega + \omega_0^2} U(\omega)$$

Where ω is frequency, j is $\sqrt{-1}$, and X and U are the frequency-domain representations of x and u. Taking the time derivative of both sides ((4.5) and returning to (4.2, arrives at the equation for voltage in terms of ground motion ((4.6).

(4.5)

$$\frac{\partial X(\omega)}{\partial t} = \frac{-\omega^2}{-\omega^2 + 2j\lambda\omega_0\omega + \omega_0^2}\frac{U(\omega)}{\partial t}$$

(4.6)

$$V_g = -S_g\frac{\omega^2}{-\omega^2 + 2j\lambda\omega_0\omega + \omega_0^2}\frac{U(\omega)}{\partial t}$$

From (4.6 the transfer function between voltage and ground displacement can be defined by anything other than V_g and $\frac{U(\omega)}{\partial t}$. This transfer function is defined by the damping factor (λ) and the resonant frequency (ω_0) (Hons, 2008). Considering the pursuit of lower frequency data for the reasons outlined in Chapter 2, the resonant frequency is of particular importance. The datasets selected for investigation out of the 2DHD survey dataset provided by Apache Corporation feature geophones with two different resonant frequencies, 5 Hz and 10 Hz. The modeled response curves of these geophones are plotted in Figure 4.2 with the damping factor specified by the manufacturer of 0.7. Notice the effect of the 0.7 damping factor is a 3dB reduction in amplitude at the resonant frequency and an additional 12-dB/octave below that (Maxwell and Lansley, 2011).

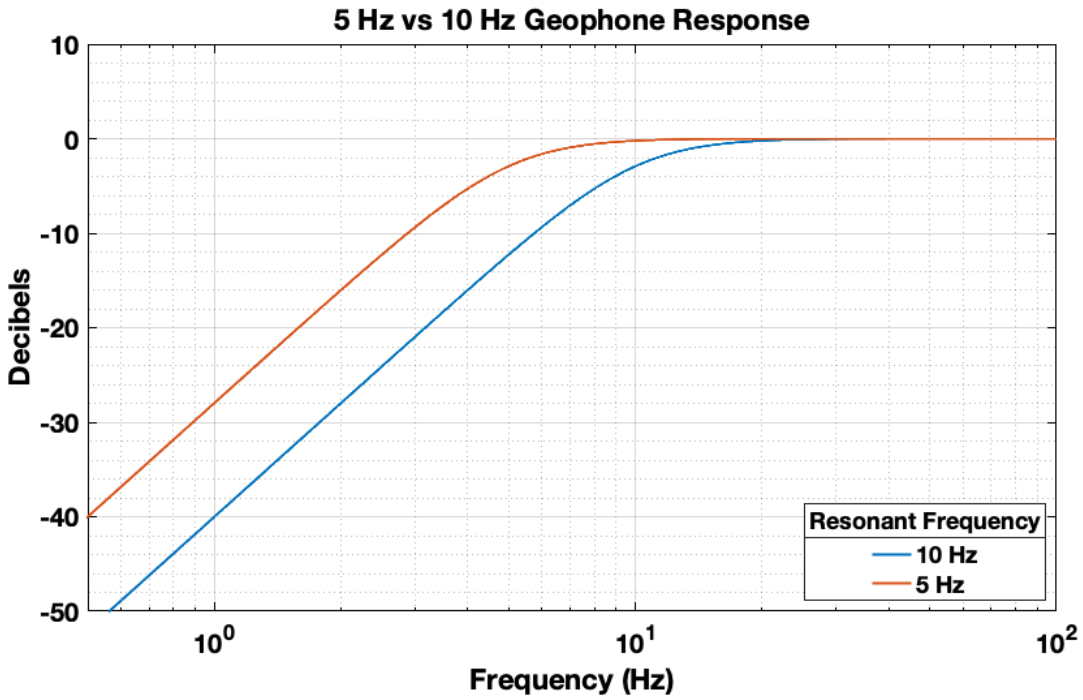

Figure 4.2 Plot of geophone response for 5 Hz and 10 Hz corner frequency and damping ratio of 0.7.

4.3 Synthetic Inversion

Following the synthetic inversions in Section 2.4, a useful analysis in this chapter is the comparison of synthetic impedance inversion results using a 5 Hz and 10 Hz synthetic seismogram. Similar to the inversions in Section 2.4, the following impedance inversion uses a well log from a well (Well A) located near the area of the seismic survey (HD2D) used in this chapter. Figure 2.28 shows the P-wave velocity (m/s) computed from sonic and Density (km/m^3) in a section of Well A from approximately 900m to 1500m (the entirety of sonic and density log in well). The formation of interest is annotated on this well by the red line correlating to an increase in density and p-wave velocity, indicative of a carbonate, at roughly 1330m. The same method for creating

the synthetic seismograms and computing the inversion was used from Section 2.4 and the result is shown in Figure 4.3.

The first thing to notice is the large difference between both the 5 Hz inversion and the 10 Hz inversion. This large difference is caused by the lack of low-frequency content between seismic and the well log. The influence of the additional low-frequency in the 5 Hz inversion can be seen by the slightly reduced difference between the 5 Hz inversion and the well log compared to the difference between the 10 Hz inversion and the well log. Figure 4.4 shows this more directly. Figure 4.4 shows the calculated difference between each synthetic inversion and the well log as a percentage. The largest difference can be seen between approximately 0.2 seconds and the end of the well log. During this time interval, the 5 Hz inversion is nearly 10% closer to the actual well-derived impedance than the 10 Hz inversion. In other words, the 5 Hz inversion is 10% more accurate then the 10 Hz inversion.

Over large fields with little well control or in fields where a very accurate inversion is needed to discern subtle impedance changes, this 10% increase in impedance accuracy is important. While well logs are often used to supply the background low-frequency trend, a low-frequency dataset adds confidence to intervals between wells with real, measured values.

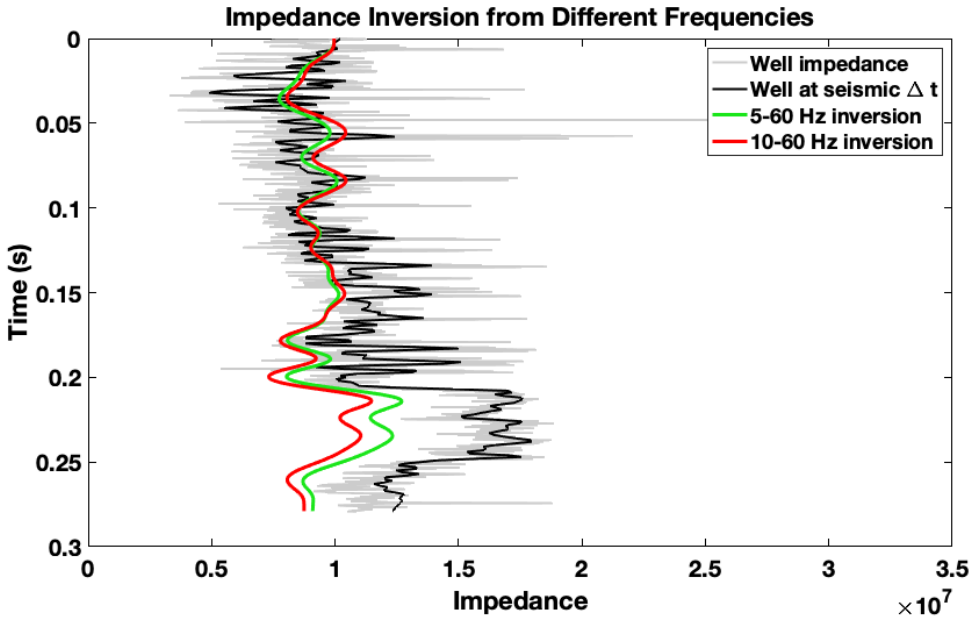

Figure 4.3 Plot of seismic impedance derived from a well log at log sampling rate, from a well log at seismic sampling, from an impedance inversion using a 5-60 Hz well-derived synthetic seismogram, and from an impedance inversion using a 10-60 Hz well-derived synthetic seismogram.

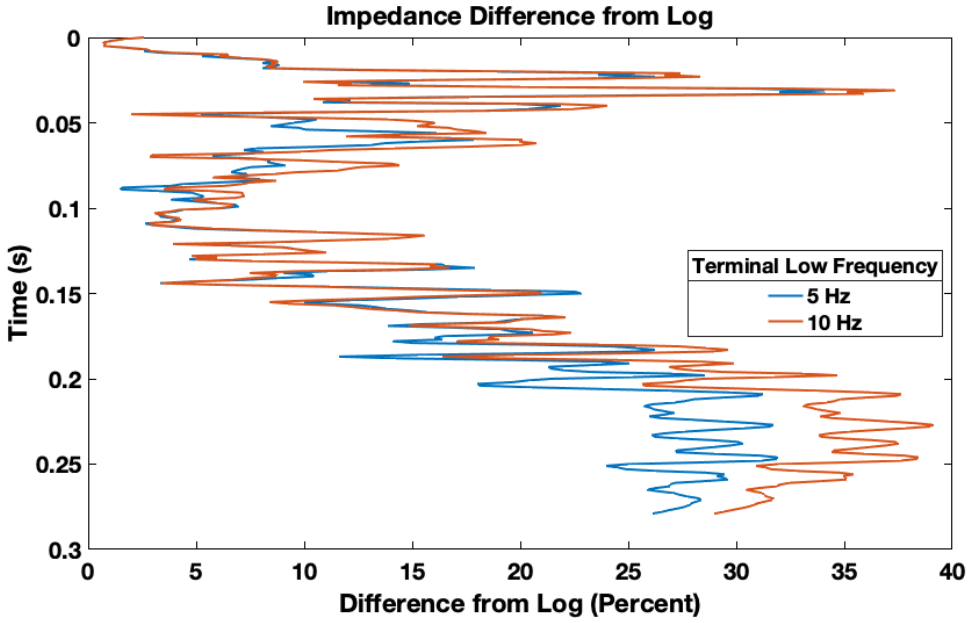

Figure 4.4 Plot of the difference between well-derived impedance and a 5 Hz and 10 Hz impedance inversion as a percentage of well-derived impedance.

4.4 Frequency Spectra (Raw Data)

The frequency spectra in Figure 4.5 and Figure 4.6 represent the average frequency response from the conventional (10 Hz) geophone (green) and low frequency (5 Hz) geophone (blue) for a local shot gather (shot 765) and the global response (all traces) respectively. While there does not appear to be an appreciable difference from these figures in the low-frequency range, a closer examination of the 0-20 Hz range of the local frequency spectra, displayed in Figure 4.7, and the global frequency spectra, displayed in Figure 4.8, reveals a small difference between the conventional and low-frequency geophones under 10 Hz. The maximum difference is approximately 4 decibels at 6 Hz which is less than the expected 7.7 dB difference at 6 Hz from the modeled geophone response in Figure 4.2.

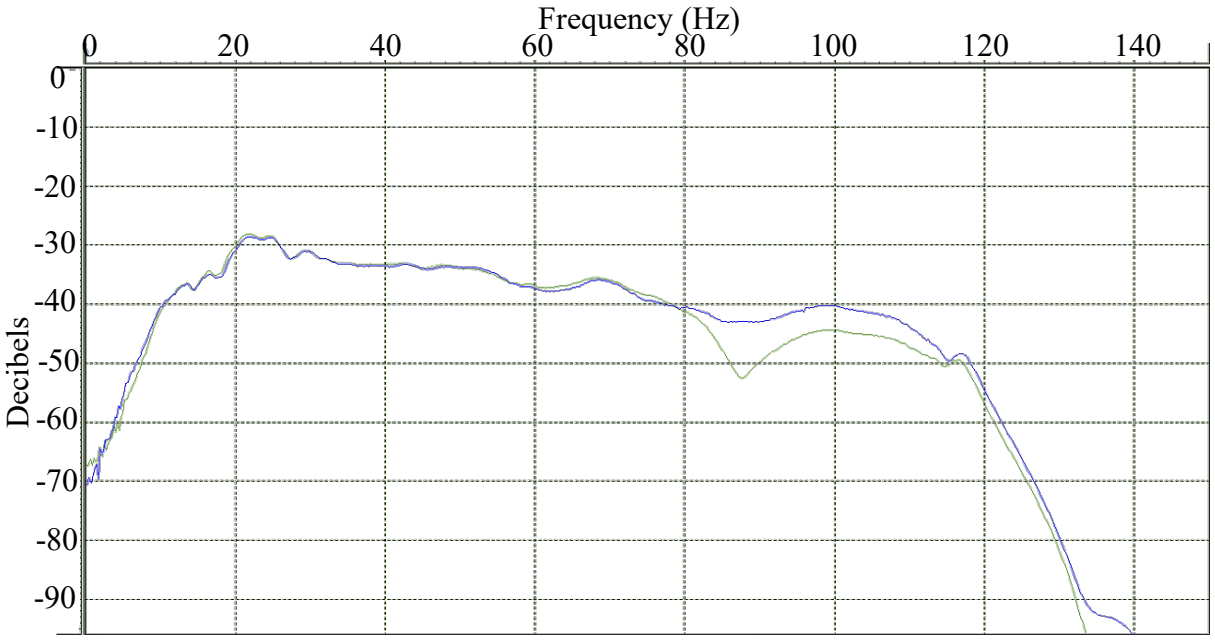

Figure 4.5 Local average frequency response of conventional (10 Hz) geophone (green) versus low frequency (5 Hz) geophone (blue) for a shot gather (shot 765).

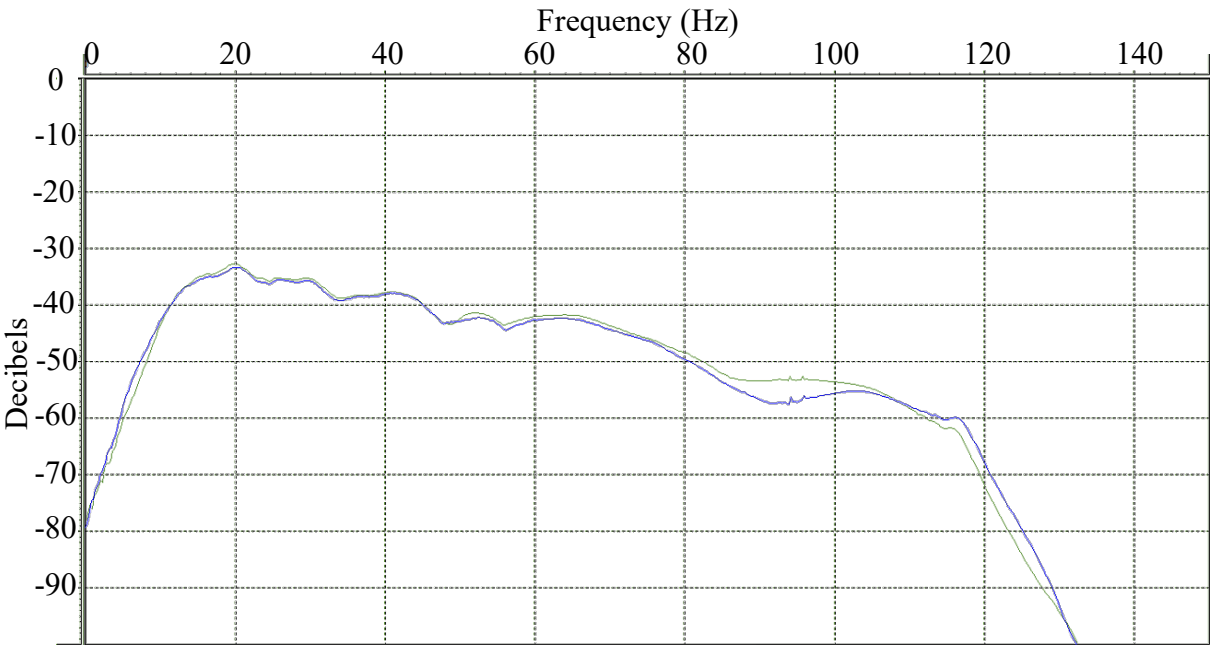

Figure 4.6 Global average frequency response of conventional (10 Hz) geophone (green) versus low frequency (5 Hz) geophone (blue).

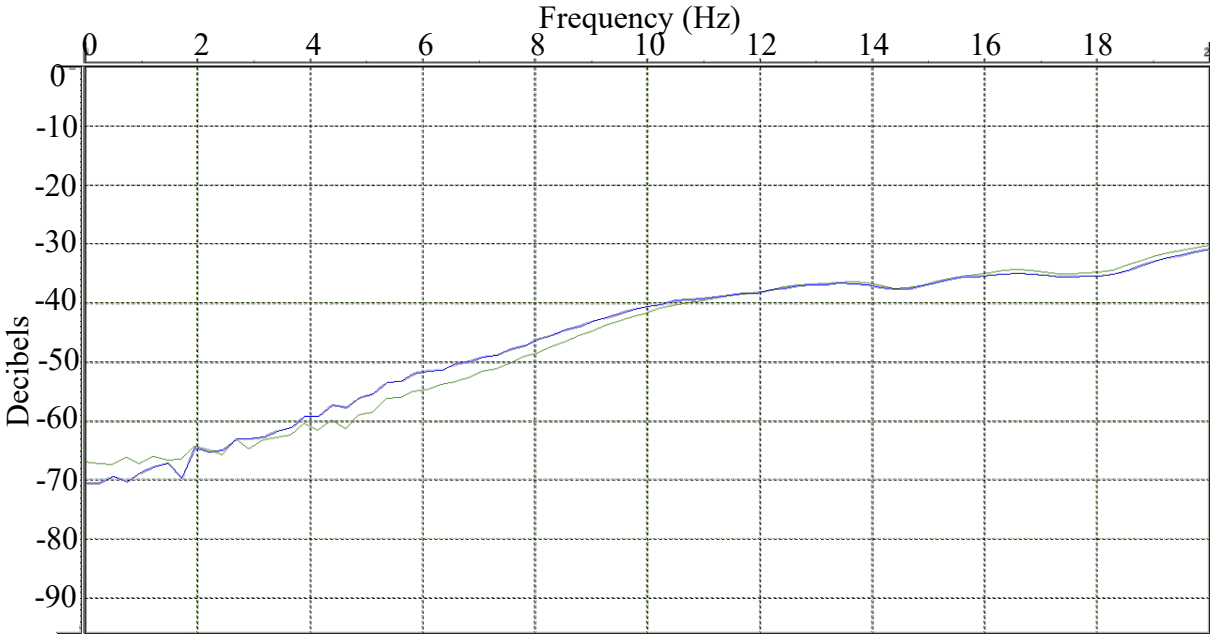

Figure 4.7 0 - 20 Hz of the local average frequency response of conventional (10 Hz) geophone (green) versus low frequency (5 Hz) geophone for a shot gather (shot 765).

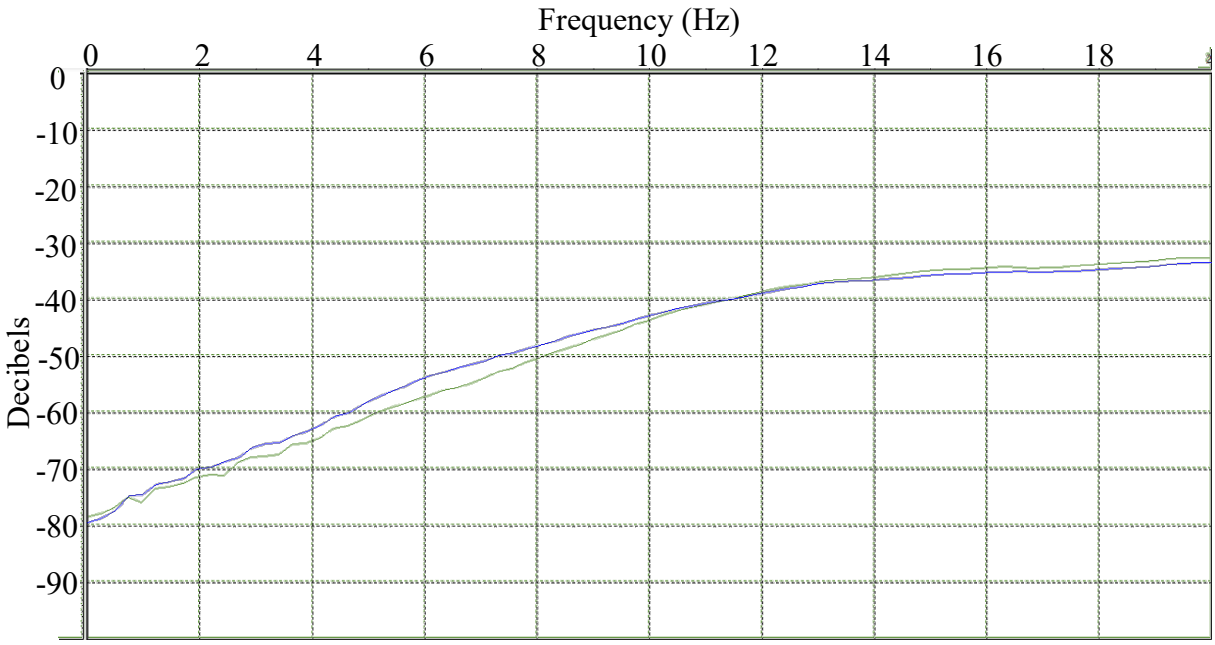

Figure 4.8 0 - 20 Hz of the global average frequency response of conventional (10 Hz) geophone (green) versus low frequency (5 Hz) geophone.

To examine a possible reason for the lack of low-frequency content in the low-frequency geophone frequency spectra, the frequency spectra for the conventional and the low-frequency geophone datasets with the linear source sweep were plotted along with the low-frequency geophone dataset with the low-dwell sweep in Figure 4.11. This plot shows that with more low-frequency energy generated from the source, there is an increase in low-frequency content recorded by the low-frequency geophone. From this observation, a possible reason for the lack of low-frequency content in the dataset can be attributed to a lack of low-frequency source signal.

Another important consideration is the frequency spectrum of the noise. If the amount of signal in the environment is not significantly greater than the noise, it is difficult to suppress the noise to a retrieve coherent signal (Winter et al., 2014). To determine the frequency content of the noise in the acquisition, a windowed frequency spectra was calculated above the first breaks in the

raw data. The resulting frequency spectra of the nosie for the low-frequency and the conventional geophone datasets are shown in Figure 4.10. In both datasets, the amount of noise increases with decreasing frequency. The amount of low-frequency noise in this survey suggests that significant effort must be put into generating low-frequency signal in order to overcome the noise.

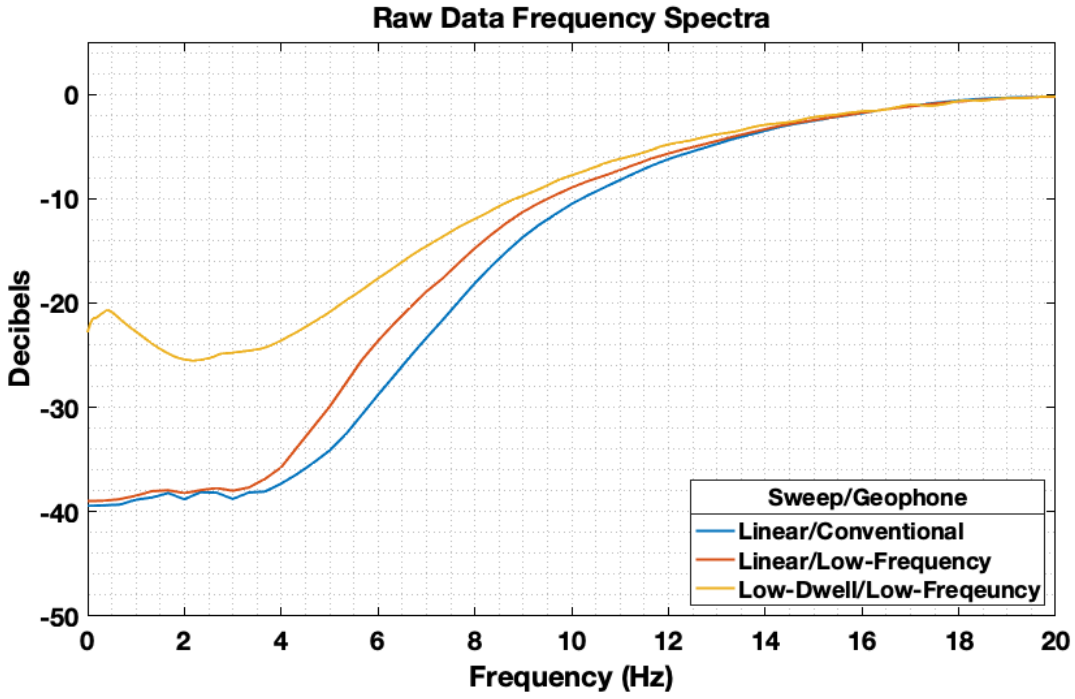

Figure 4.9 Plot of frequency spectra for three different source/receiver combinations (linear/conventional, linear/low-frequency, and low-dwell/low-frequency).

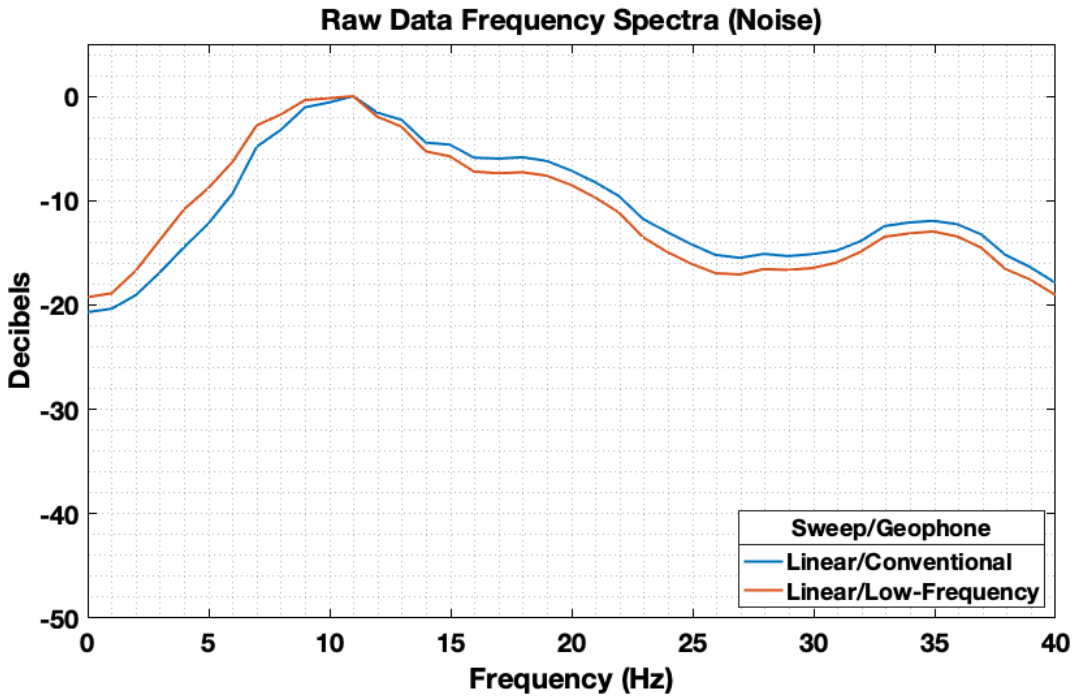

Figure 4.10 Plot of frequency spectra of noise for two difference source/receiver combinations.

4.5 Magnitude Squared Coherence (Raw Data)

Magnitude squared coherence is a measure that can be used to estimate the similarities in frequency content between the two datasets. More specifically, it is a measure that estimates the extent to which one signal can be predicted from another using a linear model (Malekpour et al., 2018). Therefore, the measure of magnitude squared coherence (MSC) between the low-frequency geophone and conventional gophone datasets estimates the similarity between the frequency content in each. The first estimation of MSC in Figure 4.11 is between the two datasets with a time window chosen above the first breaks to represent the noise. The MSC is highest in the low-frequency range here because, as shown in Figure 4.10, the magnitude of noise increases with decreasing frequency. This figure also shows the similarity between the response of the two geophones. While the amplitudes of the low frequencies are damped in the conventional geophone,

the MSC shows that the frequencies are still present, and, therefore may be enhanced to match the response of the low-frequency geophone. Figure 4.12 is another MSC plot between the low-frequency and conventional geophone datasets with a time window chosen below the first breaks to capture the seismic signal (and noise). This figure reiterates the observations from analysis of the MSC of the noise. The MSC is above 0.9 down to 3 Hz and up to 25 Hz. This observation The higher MSC in the second figure is due to the generation of high frequency signal but there is little change in the MSC at low-frequencies, which could be due to lack of low-frequency generation above noise levels. Another interesting feature to note is the fall-off of the MSC at high frequencies. This is likely a result of attenuation in the signal and scattering of the high-frequency wavefield at later times.

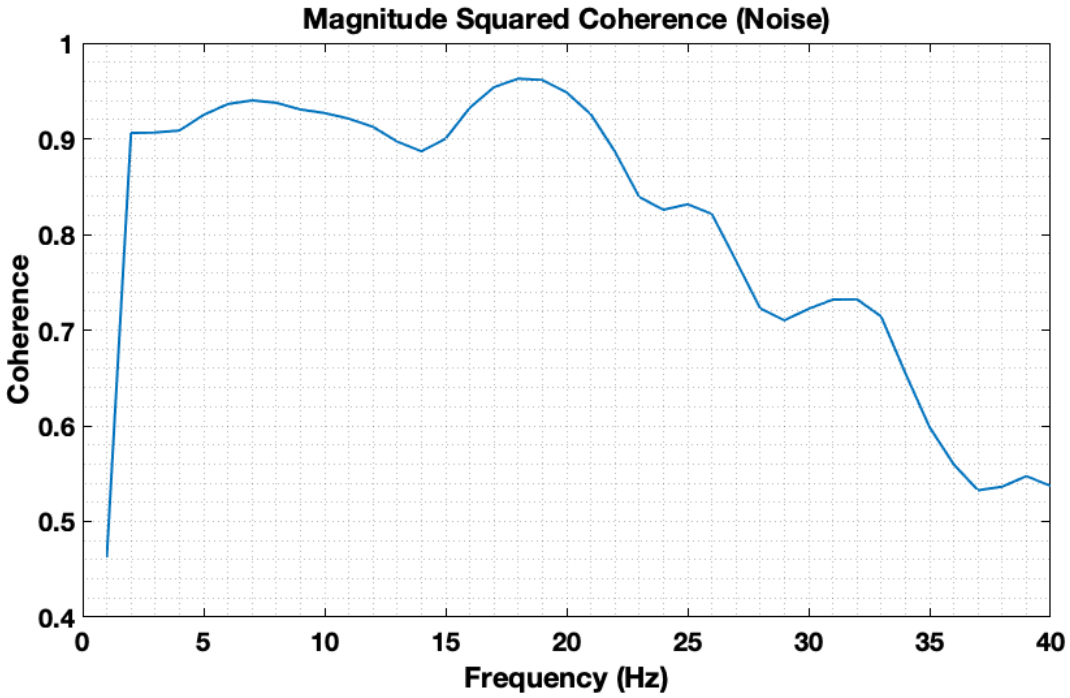

Figure 4.11 Plot of magnitude squared coherence between low-frequency and conventional geophone raw data in the 0-1s window representative of the noise.

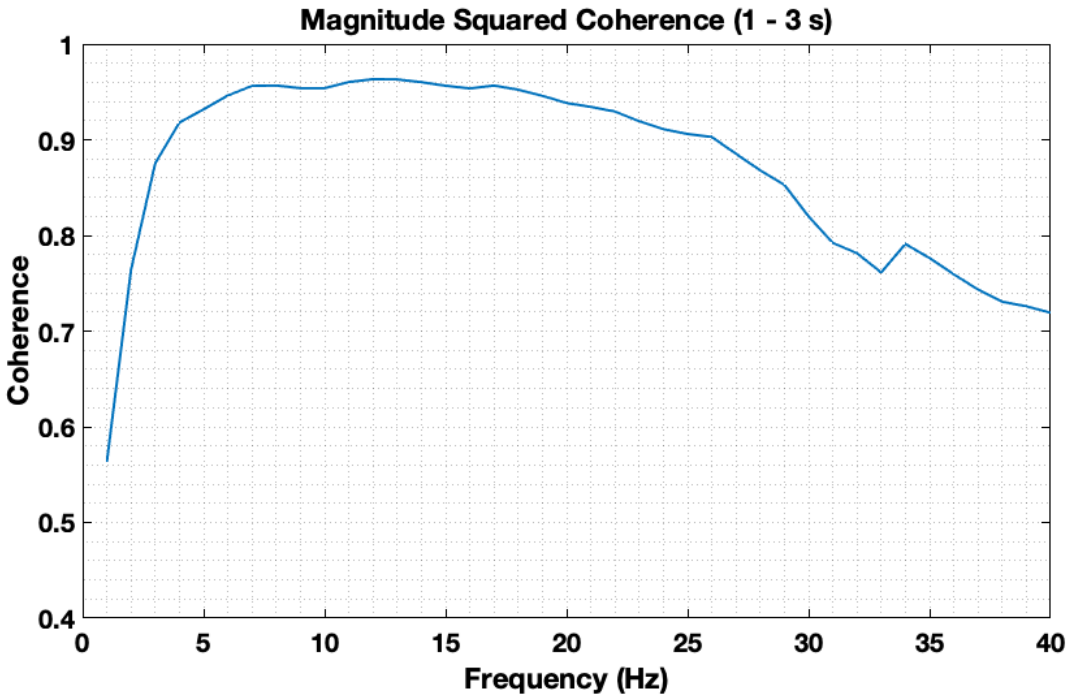

Figure 4.12 Plot of magnitude squared coherence between low-frequency and conventional geophone raw data in the 1-3s window representative of the signal and noise.

4.6 Filter Panels (Raw Data)

Evaluation of filter panels from raw data is another technique that has been used to compare datasets from different collocated receivers to show differences in frequencies within particular bands of interest (Hons, 2008). For the investigation into the coherent signal in the low end of the frequency spectrum, in the range of 2-10 Hz, two different Ormsby bandpass filters were applied to shot gathers (shot 191 and shot 5) for both the conventional and low-frequency geophones. The bandpass filters that were applied to the data are 0/2/4/6 Hz and 0/2/8/10 Hz. The first, lower frequency, bandpass filter was chosen as an end-member case to evaluate the possibility of extension of band beyond the corner frequency of the low-frequency geophone, while the 0/2/8/10 Hz bandpass filter was chosen to directly inspect the result of the difference in the frequency

spectra of the conventional and low-frequency geophones around 6 Hz. Figures 4.7-4.10 and 4.14-4.17 are the results of this exercise. There does not appear to be a noticeable difference between the conventional and low-frequency datasets from these filter panels. This is likely due to the high amount of noise in the data, which can be observed in the unfiltered shot gather in Figure 4.17 and the low frequency well noise annotated in Figure 4.13 and Figure 4.18.

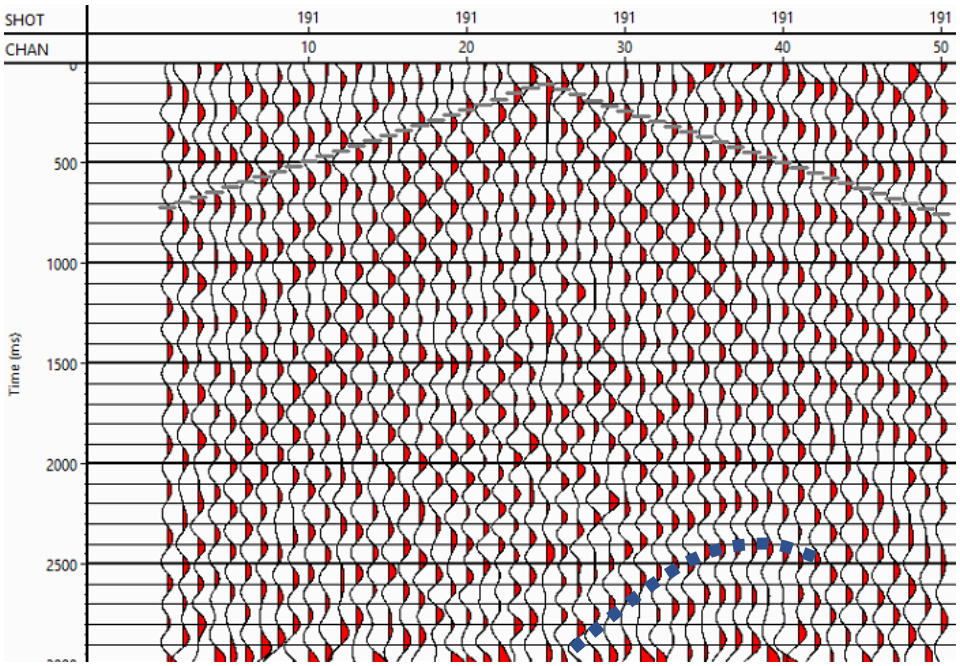

Figure 4.13 Seismic shot gather from shot number 191 into low-frequency (5 Hz) geophones with 500 ms AGC, RMS trace scaling, and 0/2/4/6 Ormsby bandpass filter applied. Gray lines indicate picked first breaks. Well noise is annotated with a blue dashed line.

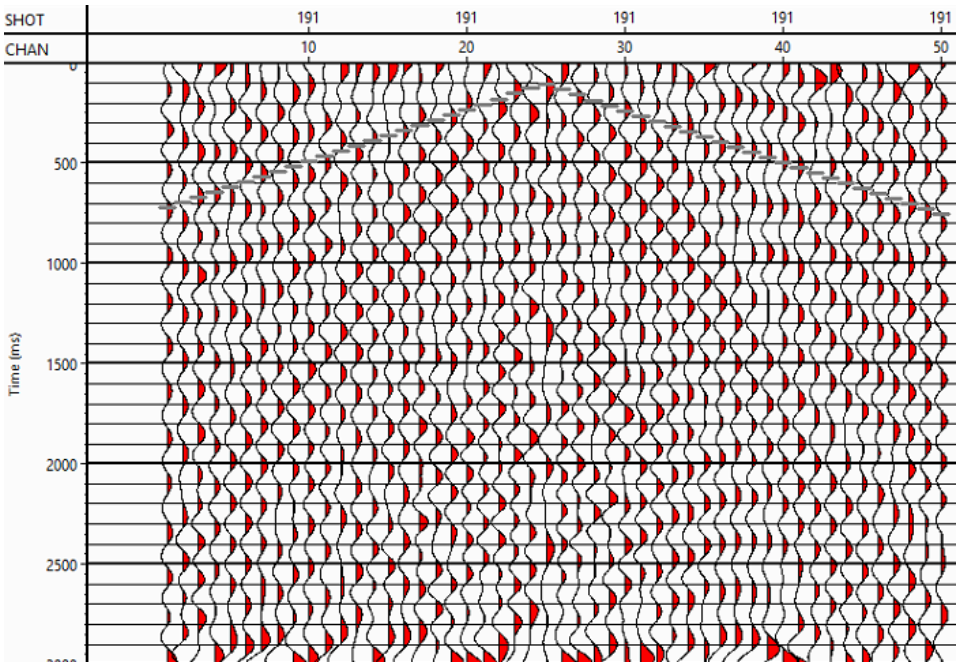

Figure 4.14 Seismic shot gather from shot number 191 into conventional (10 Hz) geophones with 500 ms AGC, RMS trace scaling, and 0/2/4/6 Ormsby bandpass filter applied. Gray lines indicate picked first breaks.

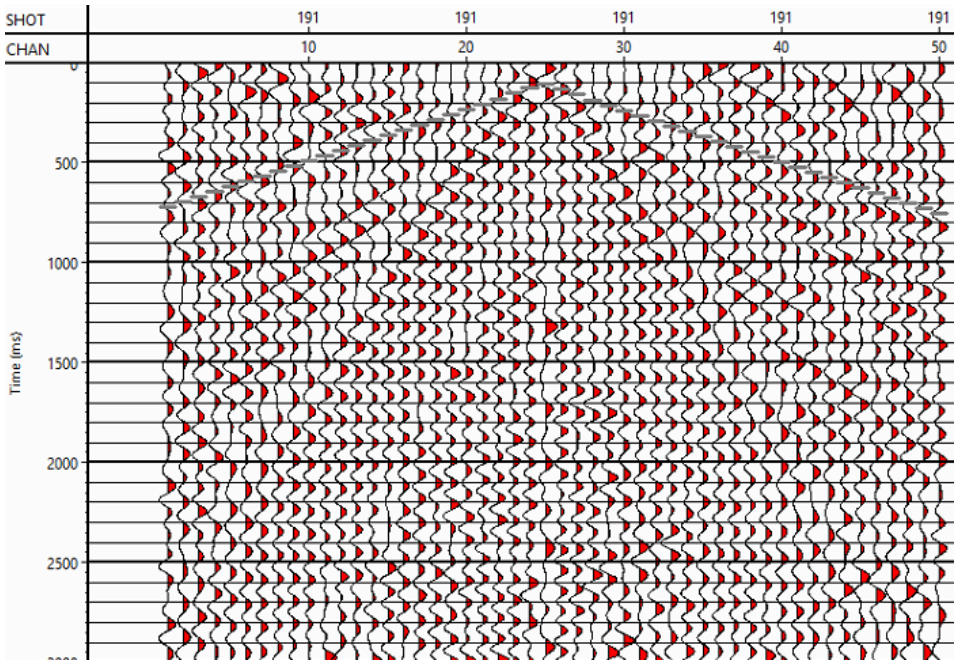

Figure 4.15 Seismic shot gather from shot number 191 into low-frequency (5 Hz) geophones with 500 ms AGC, RMS trace scaling, and 0/2/8/10 Ormsby bandpass filter applied. Gray lines indicate picked first breaks.

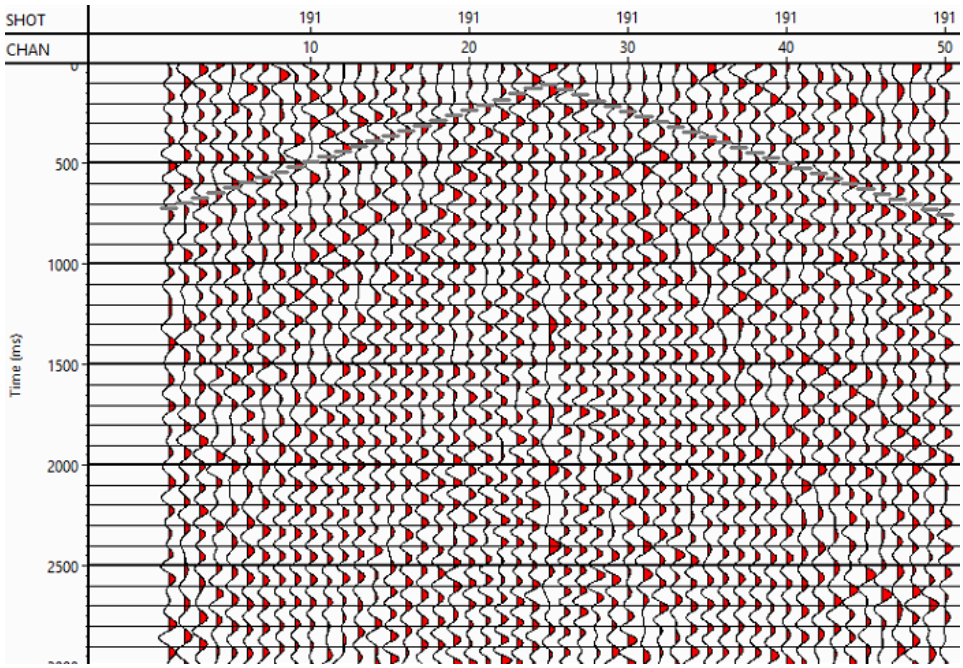

Figure 4.16 Seismic shot gather from shot number 191 into conventional (10 Hz) geophones with 500 ms AGC, RMS trace scaling, and 0/2/8/10 Ormsby bandpass filter applied. Gray lines indicate picked first breaks.

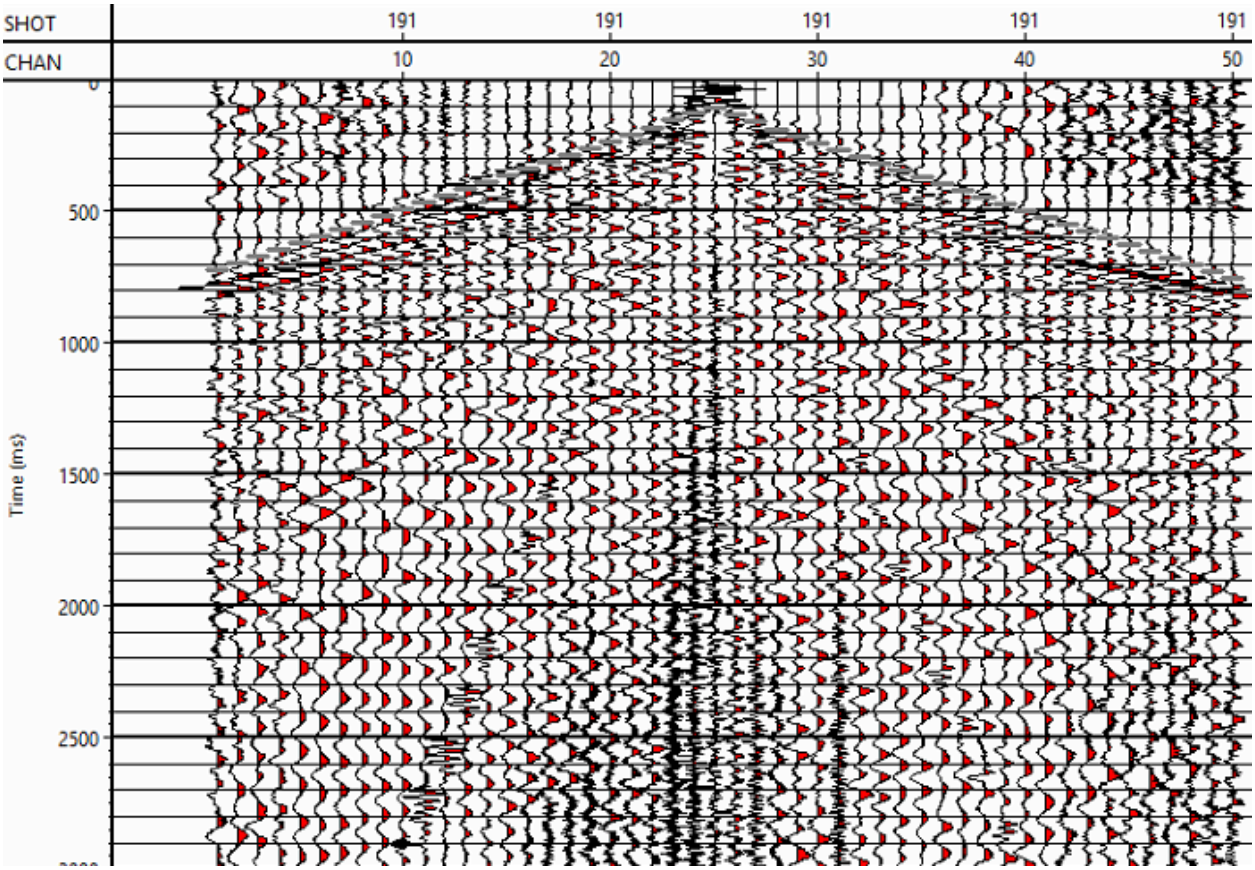

Figure 4.17 Shot gather 191 into low-frequency geophones with 500 ms AGC and RMS trace scaling shows the noisy nature of the raw data.

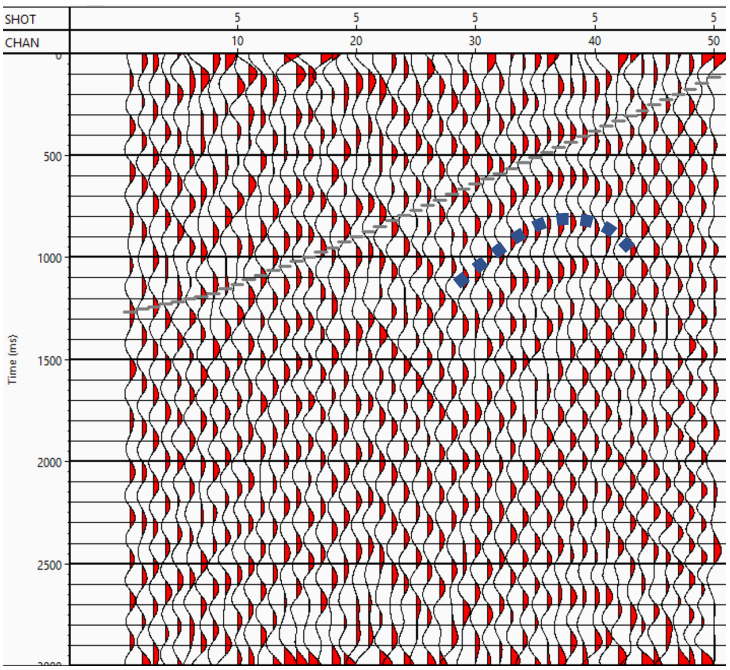

Figure 4.18 Seismic shot gather from shot number 5 into conventional (10 Hz) geophones with 500 ms AGC, RMS trace scaling, and 0/2/4/6 Ormsby bandpass filter applied. Gray lines indicate picked first breaks. Well noise is annotated with a blue dashed line.

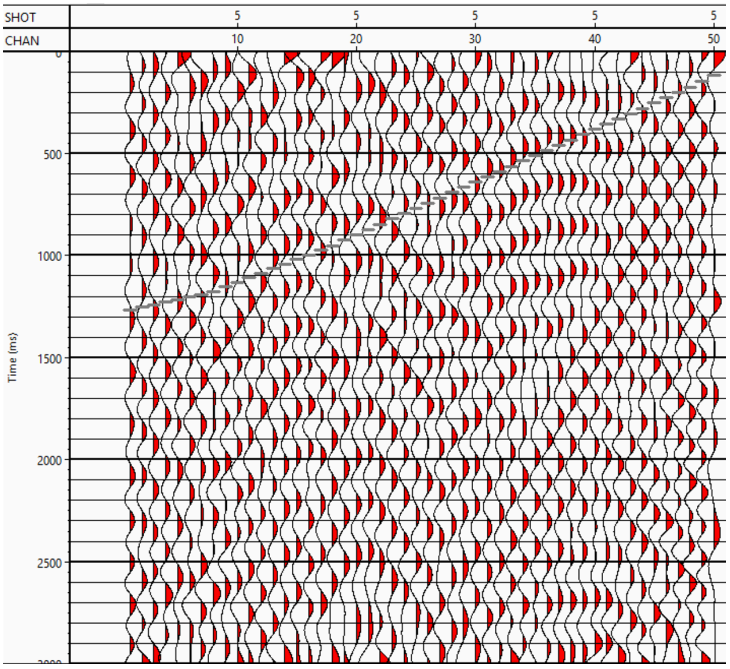

Figure 4.19 Seismic shot gather from shot number 5 into low-frequency (5 Hz) geophones with 500 ms AGC, RMS trace scaling, and 0/2/4/6 Ormsby bandpass filter applied. Gray lines indicate picked first breaks.

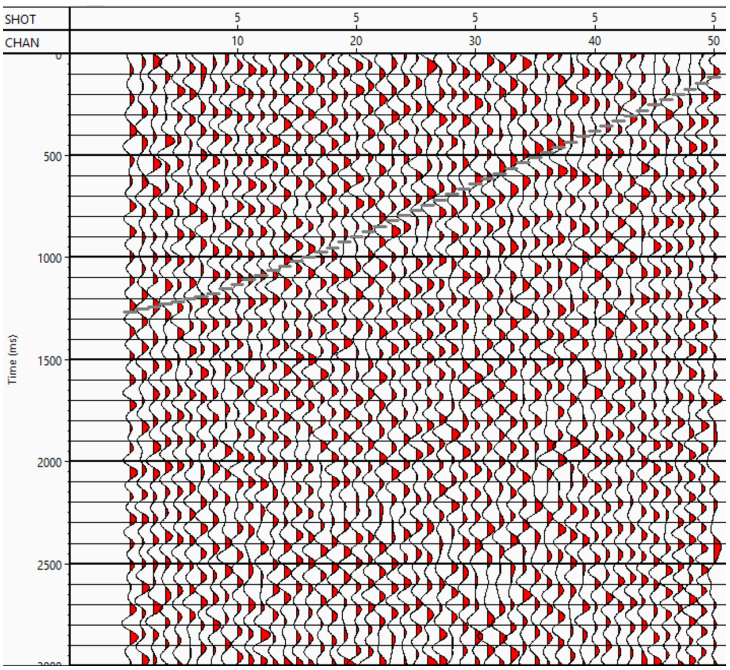

Figure 4.20 Seismic shot gather from shot number 5 into conventional (10 Hz) geophones with 500 ms AGC, RMS trace scaling, and 0/2/8/10 Ormsby bandpass filter applied. Gray lines indicate picked first breaks.

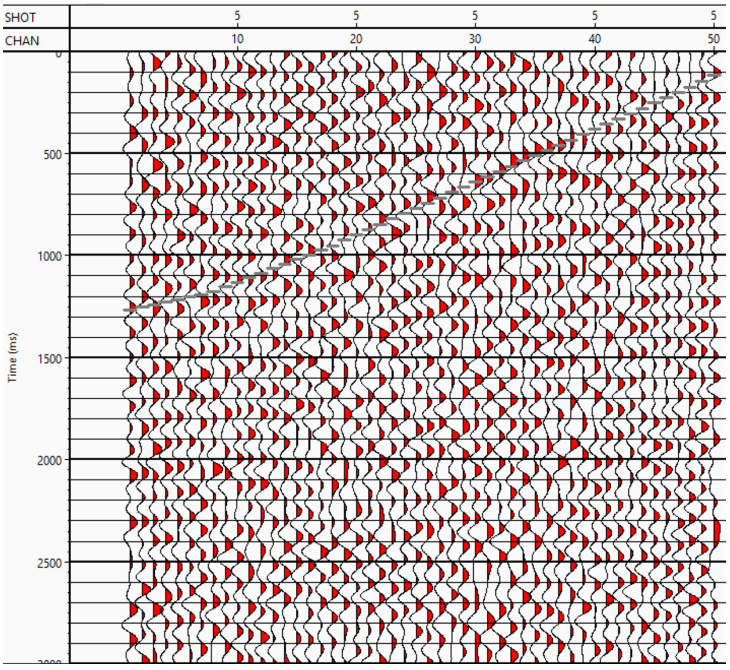

Figure 4.21 Seismic shot gather from shot number 5 into low-frequency (5 Hz) geophones with 500 ms AGC, RMS trace scaling, and 0/2/8/10 Ormsby bandpass filter applied. Gray lines indicate picked first breaks.

4.7 Processing

The processing of these 2D seismic lines was aided by several sources: *Seismic Data Analysis* by Oz Yilmaz (2001), VISTA example 2D seismic processing flows, Schlumberger technical support staff, and early processing reports from Apache Corporation. Due to the exceptionally noisy nature of this seismic data, significantly advanced processing and noise reduction flows were included in the processing report received from Apache Corporation. Unfortunately, the full processing flow carried out by Apache Corporation was too sophisticated for the capabilities of VISTA. Additionally, Apache Corporation was able to apply static corrections and utilize velocity models derived from the high-resolution 3D survey acquired alongside the HD2D survey which was not provided to The University of Houston for use in this research. Nevertheless, the datasets were fully processed according to the flow below. Some of the steps are covered in more detail in the following sections. While the following sections show details and examples form the low-frequency dataset, both datasets were processed according to the same processing flow independently.

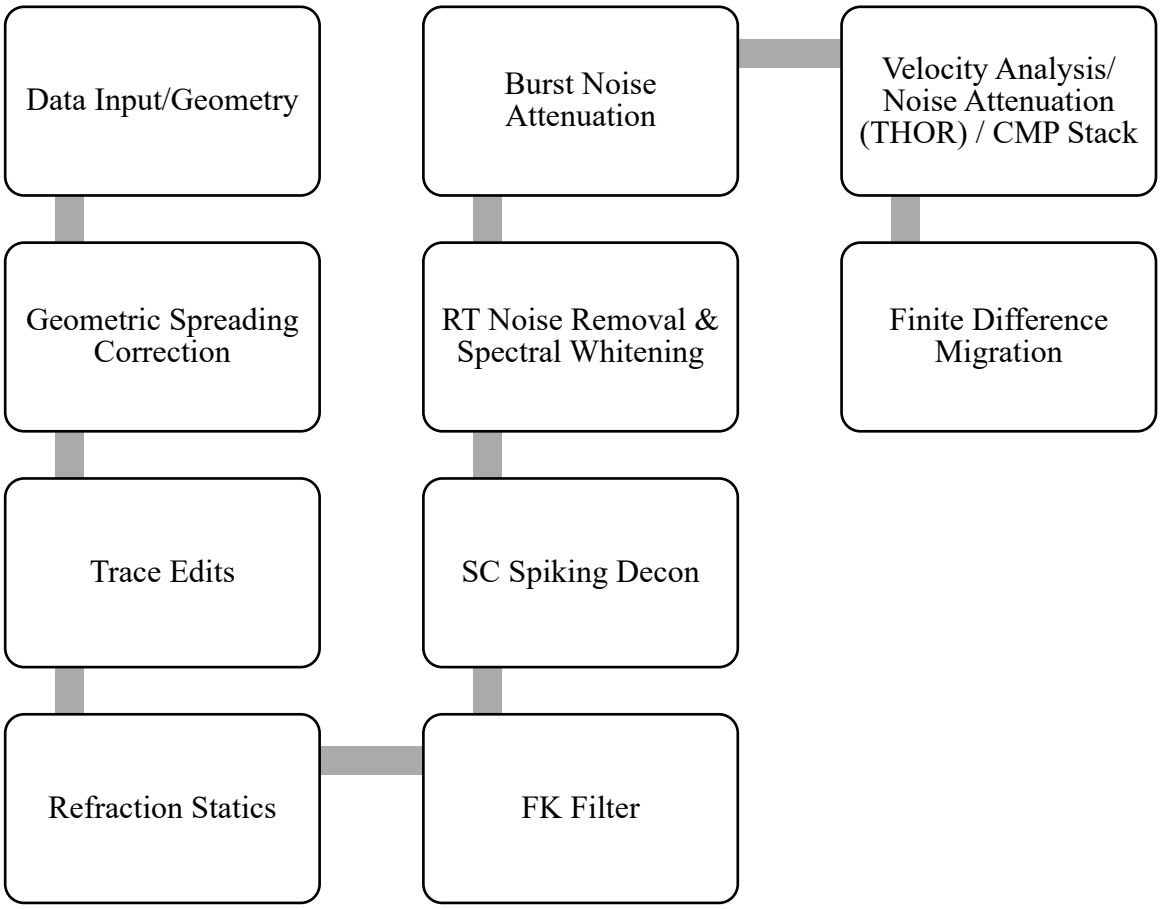

Figure 4.22 Processing flow outline for the 2DHD seismic line.

4.7.1 Data Input & Geometry

The first step in processing this data was loading it into VISTA and reading the SPS files into the geometry window to be saved in trace headers. While seemingly trivial, this task was one of the more tedious in the processing workflow. The complications arose from the lack of header information in most of the supplied datasets and missing ".xps" relational file. Since the survey used several different sources and receivers with identical geometries in either source geometry, receiver geometry, or both, the datasets with existing header information were used to extract

geometry that was then applied to datasets with missing information. Once both of the datasets used in this project had complete geometry information in the headers, the dataset from the conventional geophone was subsampled to only include receiver locations where the low-frequency geophones were collocated to ensure a direct comparison between the two datasets. Figure 4.23 shows the resulting surface geometry display of source locations, receiver locations, CMP bins, and calculated fold.

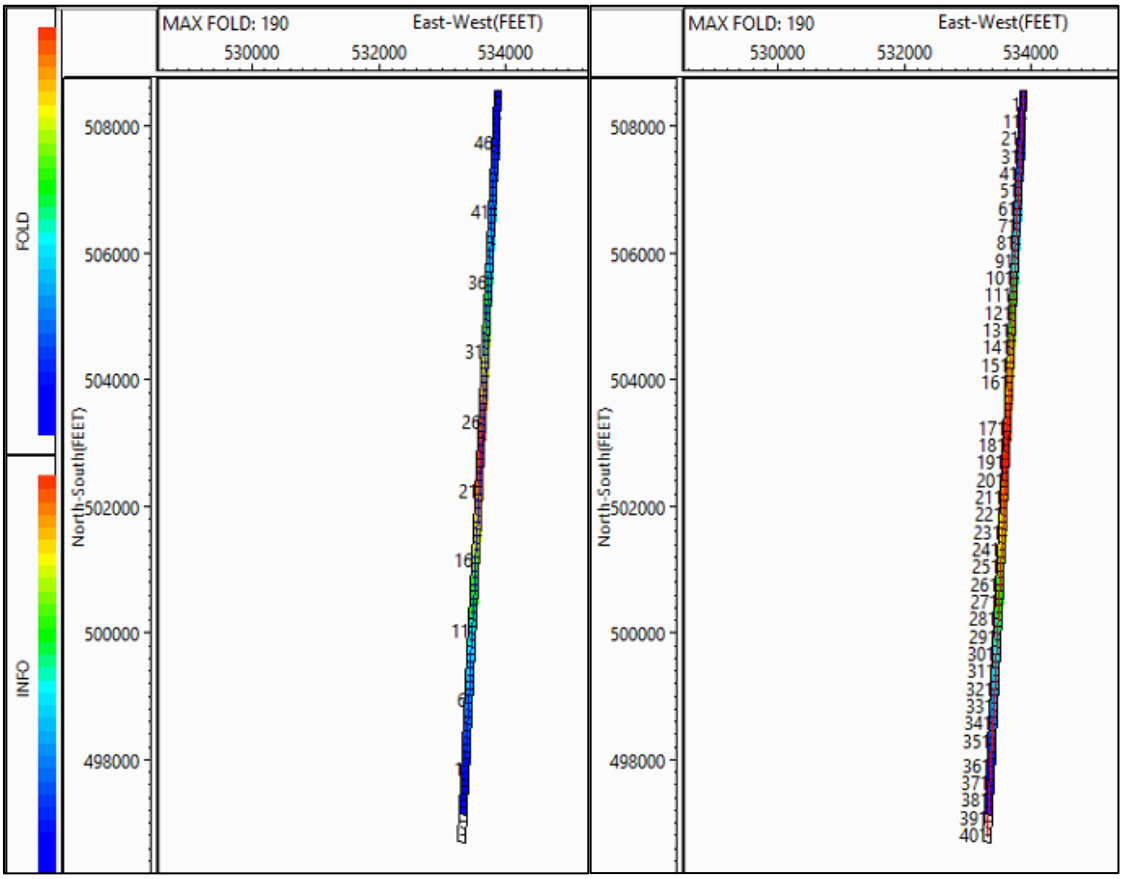

Figure 4.23 Surface geometry display including bins and fold. Receiver locations annotated on the left image. Source Locations annotated on the right image.

4.7.2 Trace Edits

Traces that warranted removal were identified using a plot of calculated trace attributes (RMS Amplitude and Max Frequency) versus source-receiver offset. Traces with markedly high RMS amplitude compared to traces at the same offset were determined to be exceptionally noisy and were killed by the polygon as shown in Figure 4.24. Similarly, traces with strong noise in high or low-frequency ranges, or monochromatic noise with a known frequency value (such as 60 Hz from power lines) can be easily identified in a plot of maximum frequency versus source-receiver offset (Figure 4.25). Max frequency, in this case, is the frequency corresponding to the maximum amplitude in the frequency spectrum.

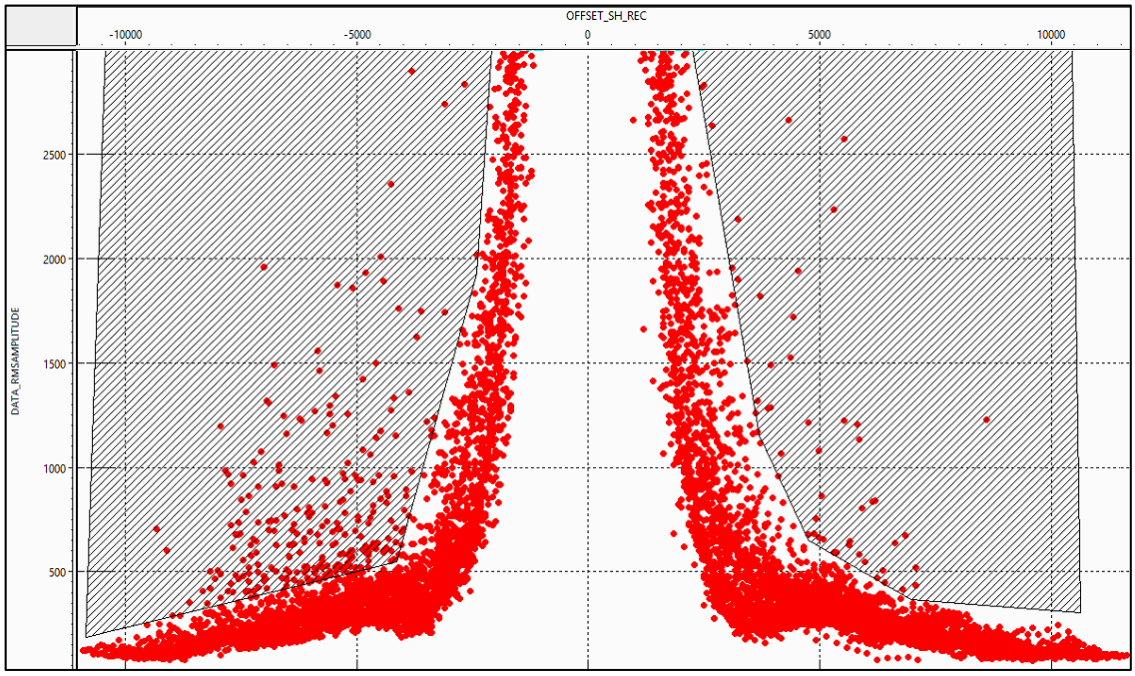

Figure 4.24 Plot of RMS Amplitude versus Source-Receiver Offset. Each red dot indicates the RMS amplitude value for a trace at a source-receiver offset shown along the x-axis. The black polygon indicates the region of traces to kill because of exceptionally high RMS amplitude compared to traces at similar offsets. (Low-frequency geophones)

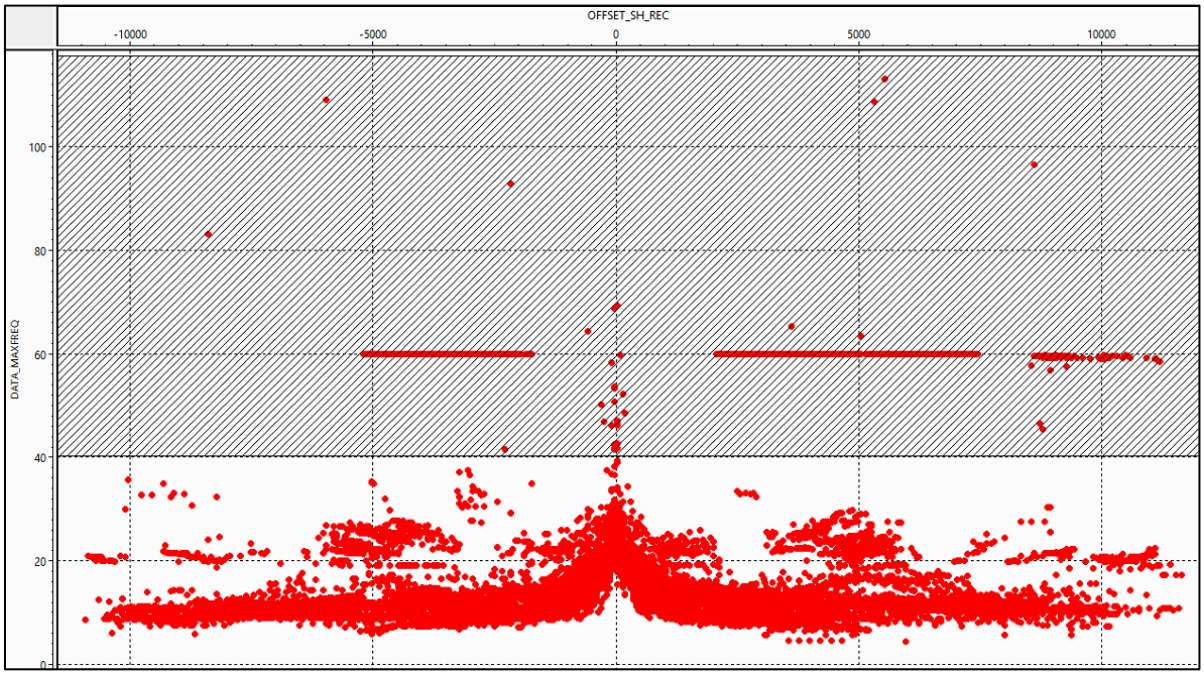

Figure 4.25 Plot of Max Amplitude versus Source-Receiver Offset. Each red dot indicates the maximum frequency value for a trace at a source-receiver offset shown along the x-axis. The black polygon indicates the region of traces to kill because of exceptionally high max frequency values compared to traces at similar offsets. (Low-frequency geophones)

4.7.3 FK Filter

FK filtering is a processing technique that can be used to eliminate coherent linear noise that obscure primary reflections in the recorded data such as ground roll (Yilmaz, 2001). For this study, a conservative FK filter was designed (Figure 4.26) by using the velocity tool in VISTA to preserve as much signal as possible while eliminating much of the coherent noise.

Along with the velocity lines in VISTA's FK filter design window, the seismic sections in Figure 4.27 and Figure 4.28 were used to iteratively test the effect of the filter on the receiver gather. Figure 4.27 shows the raw input receiver gather in the left pane and the filtered receiver gather in the right pane. Notice the removal of steep dipping events that correspond to low-velocity coherent noise. Figure 4.28 also shows the raw input receiver gather in the left pane but the right

pane shows the difference between the filtered receiver gather and the raw receiver gather. The difference section is a critical component of the iterative process used to design an FK filter because it can show if an FK filter is too aggressive. An FK filter that is too aggressive will remove parts of the reflection signal that may not be noticeable by examination of the filtered receiver gather alone.

Through the iterative process of picking velocities of dipping coherent events in the receiver gather, designing a fan filter within the bounds of the picked velocities, and examination of the filtered and difference receiver gathers, an FK filter was chosen that removed significant coherent linear noise while retaining as much signal as possible. This filter was then applied to the dataset sorted in receiver gathers.

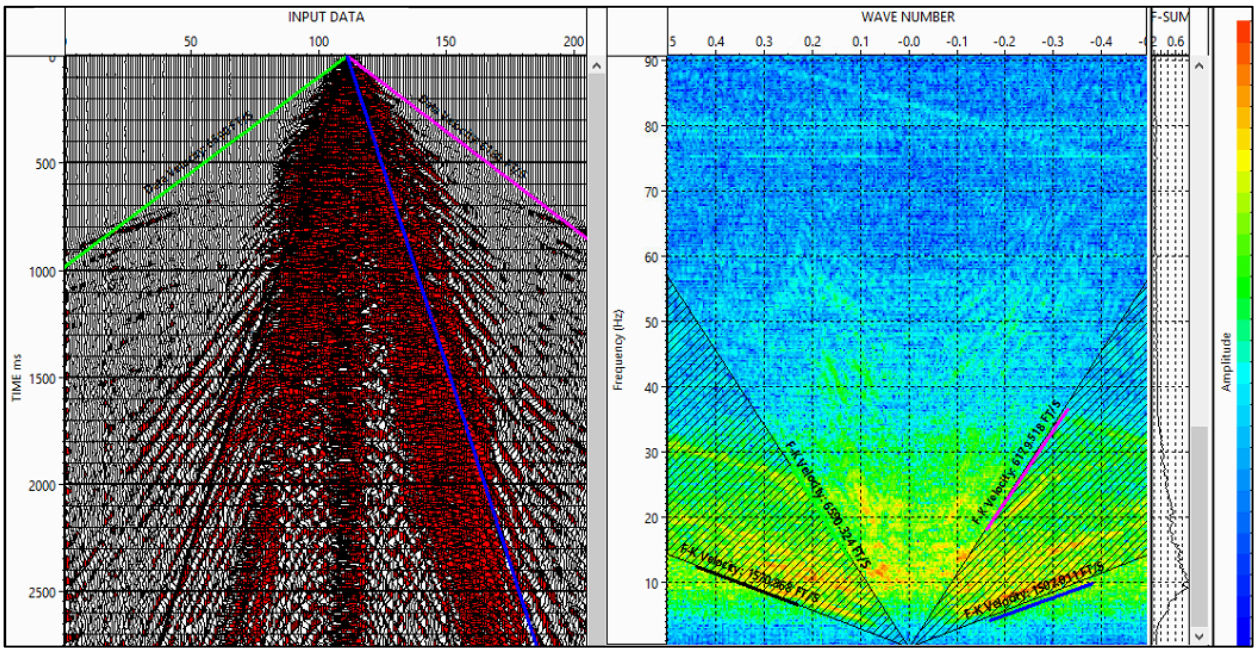

Figure 4.26 FK filter design window from VISTA. The left pane is the raw input receiver gather with velocity lines annotated on top for guides to create the FK filter. The right pane is the FK plot showing amplitude in the frequency and wavenumber domains. The lines annotated on the right plot correspond to the lines on the left representing velocities used as guides to design the dip filter which is indicated by the symmetric fan on the right image. (Low-frequency geophone station number 23)

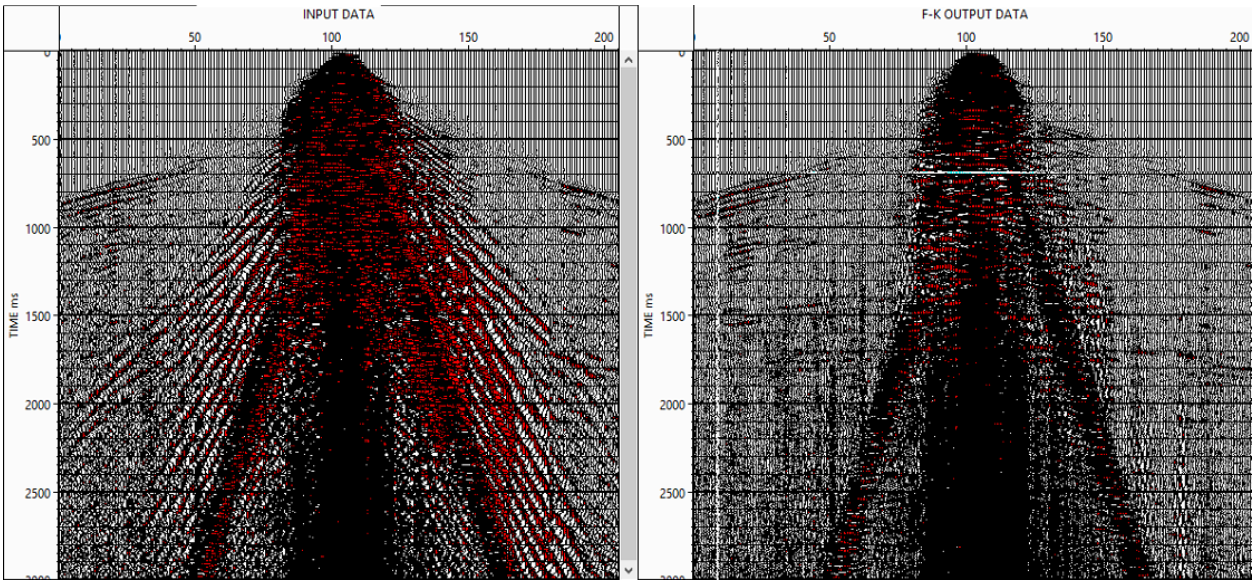

Figure 4.27 FK filter design window from VISTA. Left pane is the raw input receiver gather. The right pane is the receiver gather with the FK filter from Figure 4.26 applied. The FK filter has removed much of the coherent energy with a large dip which corresponds to low-velocity coherent noise. (Low-frequency geophone station number 23)

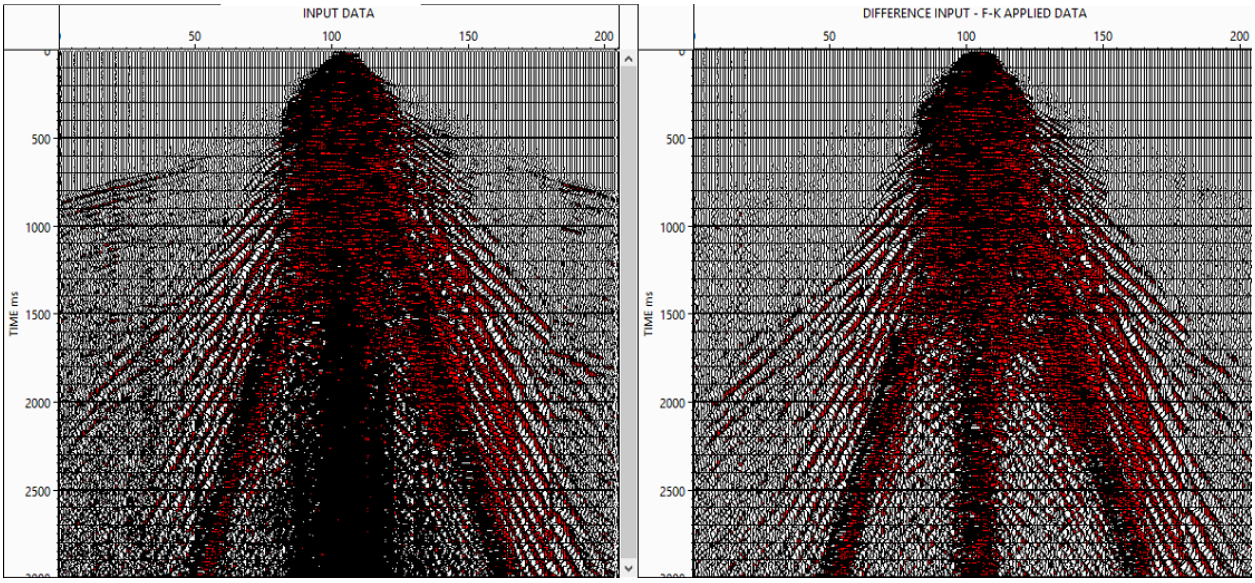

Figure 4.28 FK filter design window from VISTA. Left pane is the raw input receiver gather. The right pane is the difference between the FK filtered receiver gather and the raw receiver gather. The FK filter has removed much of the coherent energy with a large dip which corresponds to low-velocity coherent noise. (Low-frequency geophone station number 23)

4.7.4 Surface Consistent Spiking Deconvolution

Deconvolution is a crucial processing step that compresses the wavelet, attenuates reverberations and short-period multiples, and increases temporal resolution (Yilmaz, 2001). For this research, a spiking deconvolution was applied with a 240 ms operator and 1% pre-whitening, consistent with the parameterization from the Apache Corporation processing report. The result of deconvolution with RT noise removal, spectral whitening, and burst attenuation applied through rank reduction is shown in Figure 4.29. The effect of the aforementioned processing steps on the shot gather in Figure 4.29 is most noticeable in the appearance of hyperbolic reflection events that are not visible before the execution of these steps. Also, the removal of the burst energy through the central channels of the shot gather enhances the image. Finally, as is the purpose of deconvolution, the shot gather after deconvolution has a much sharper and condensed wavelet compared to the input shot gather.

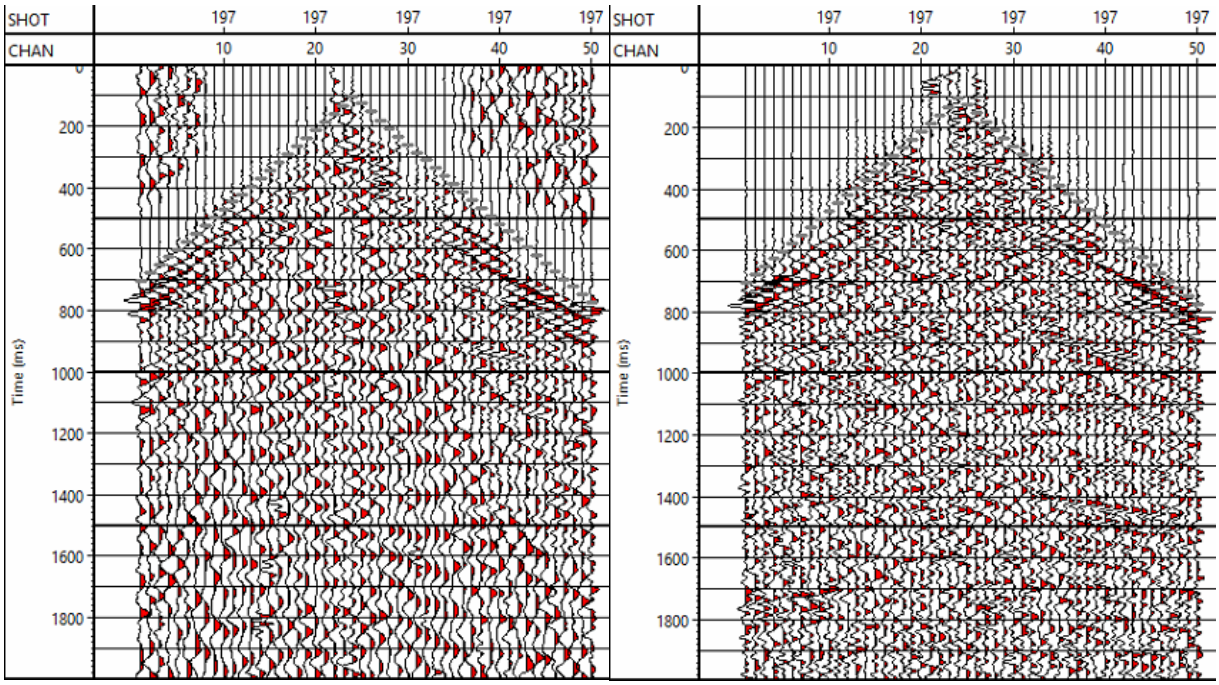

Figure 4.29 The left pane is the shot gather from shot 197 before deconvolution, RT noise removal, spectral whitening, and burst attenuation. The right pane is the shot gather from shot 197 after deconvolution, RT noise removal, spectral whitening, and burst attenuation. (500 ms AGC applied) (low-frequency geophone dataset)

4.7.5 Velocity Analysis

An accurate velocity model is crucial in creating a reliable stacked seismic image. Figure 4.30 is an image of the interactive velocity analysis module of VISTA representative of the velocity analysis that was undertaken during the processing of the conventional and low-frequency datasets being investigated. The total velocity model along the 2D line was derived from semblance plot velocity picks every 10 CDPs resulting in the velocity model shown in Figure 4.31 This velocity model is later used for NMO correction and finite-difference migration to create the final seismic image.

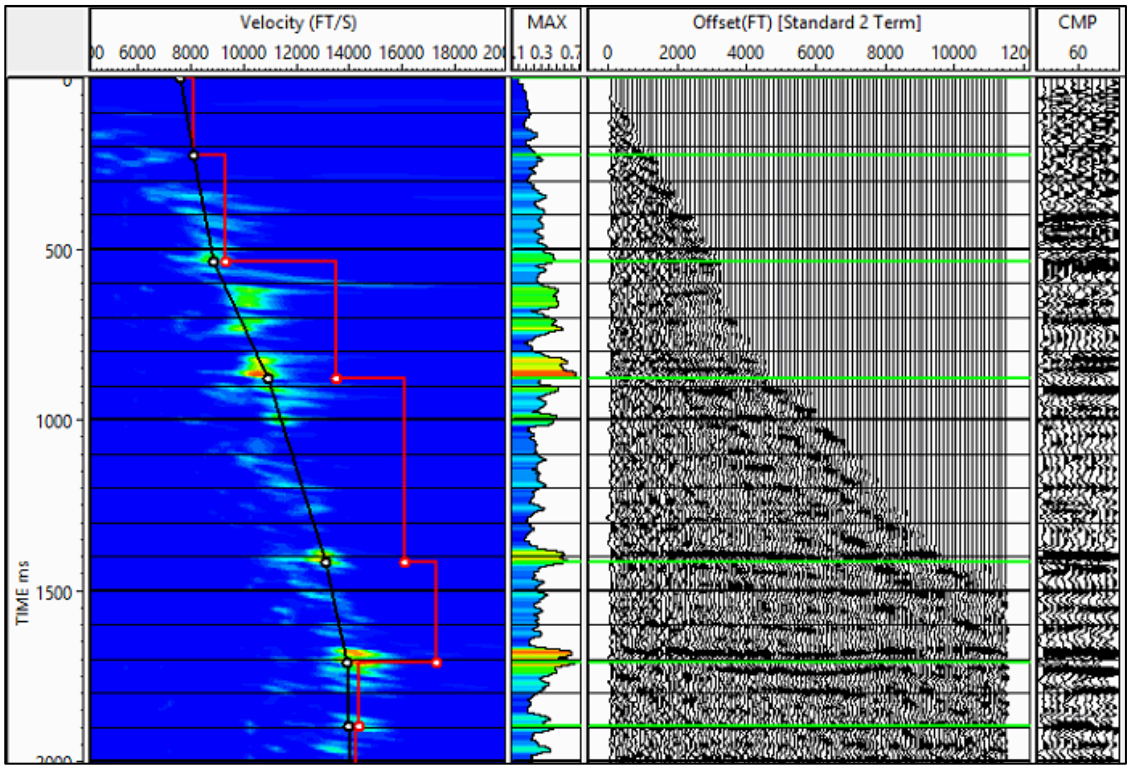

Figure 4.30 The left panel is a semblance plot with picked velocities. The middle right plot is an NMO corrected CMP. The right panel is a segment of the NMO corrected stacked section. (low-frequency geophone dataset)

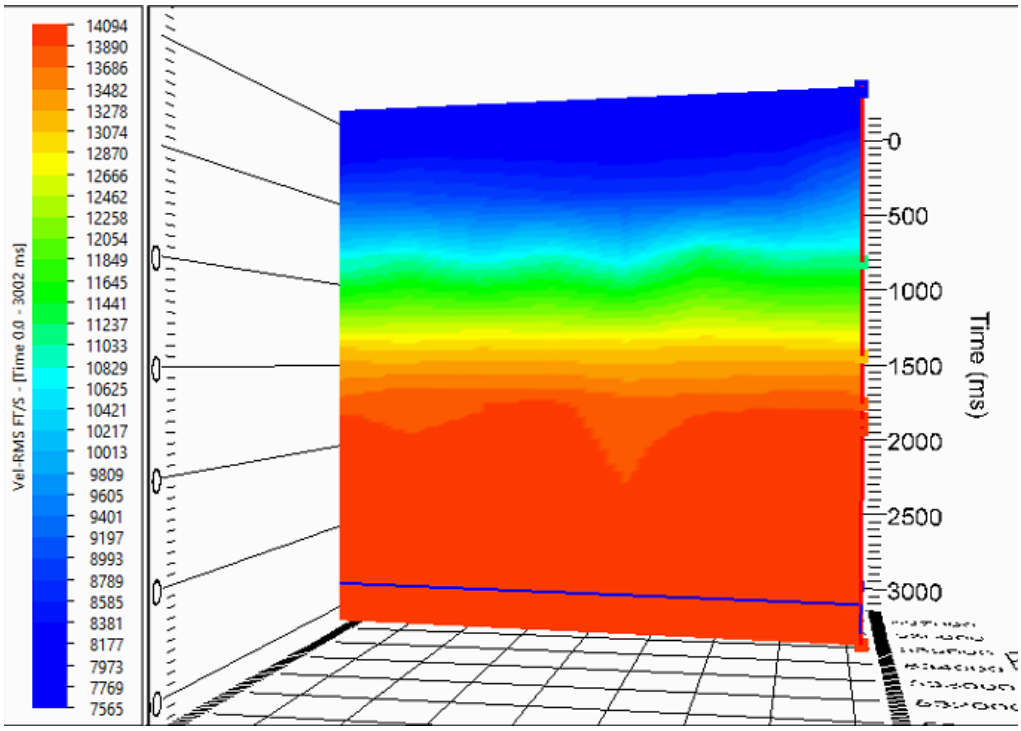

Figure 4.31 2D velocity model from semblance plot velocity picks for low-frequency geophone dataset.

4.7.6 Finite-Difference Migration

A simple 45-degree finite-difference migration was used to migrate the NMO corrected and stacked data in Figure 4.32. The resulting final image is shown in Figure 4.33.

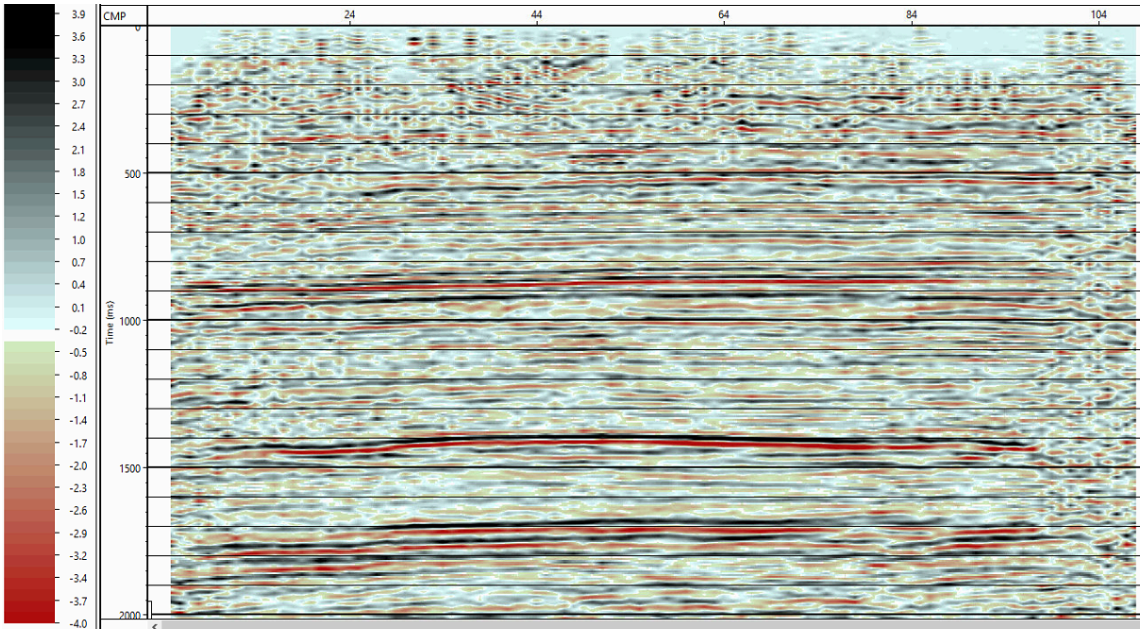

Figure 4.32 Brute Stack of low-frequency geophone dataset.

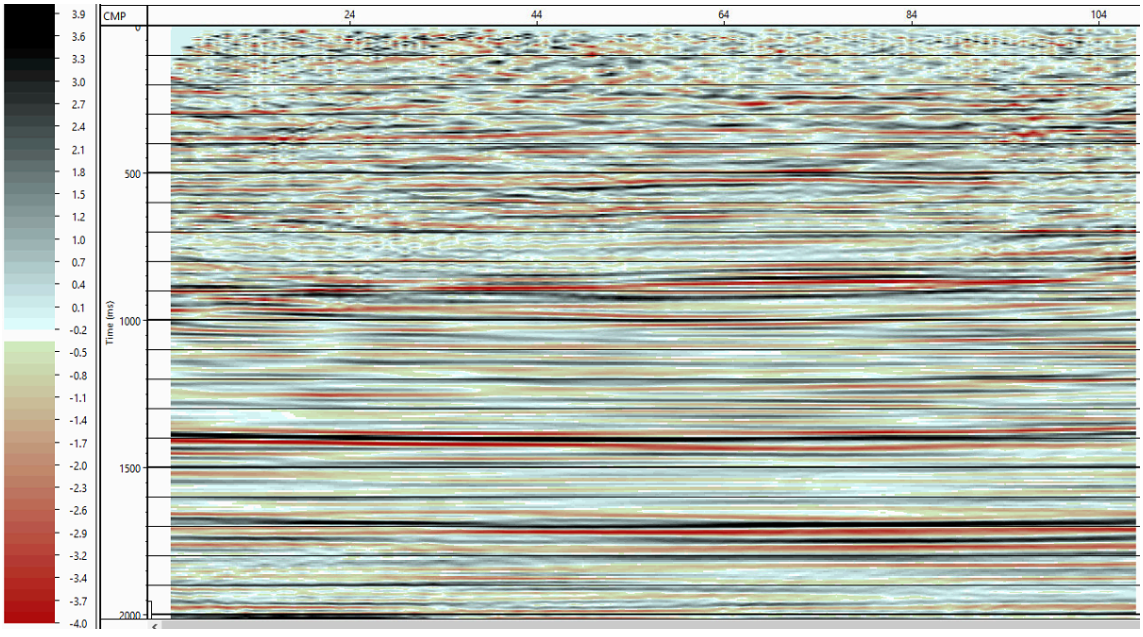

Figure 4.33 Finite-difference migrated final image of low-frequency geophone dataset.

4.8 Field Data Analysis

The purpose of the analysis of the data in this research is to determine the amount of coherent low-frequency signal gained by utilizing a low frequency (5 Hz) geophone compared to a conventional 10 Hz geophone. This analysis will consist of an examination of frequency panels, frequency spectra, and extracted wavelets to determine the minimum frequency that contributes to coherent events in the final processed image.

4.8.1 Frequency Panels

Before examining the frequency panels, it is useful to be oriented with the seismic image without additional frequency filtering. The central portion (CMP 57-97) of the fully processed 2D seismic image for the dataset using the conventional geophones and the low-frequency geophones are displayed in the left and right panes of Figure 4.34 respectively. From observation, there is a strong similarity between the images in Figure 2.24 in the ~700 ms to ~1700 ms range but the quality of the image above and below this range is significantly noisy and incoherent within images, therefore, is dissimilar between images.

Frequency panels with several different bandpass filters (0/2/5/7 Hz, 2/4/8/10 Hz, 3/5/10/14 Hz, and 5/8/16/20 Hz) were created to analyze the coherency of the low-frequency content in each dataset. These filter panels are shown in Figures 4.25-4.28.

Figure 4.35 displays each dataset with a 0/2/5/7 Hz Ormsby bandpass filter applied. In this 2-5 Hz range, there is very little expected coherent signal due to the resonant frequencies of the geophones. Upon inspection, this appears to be the case since there is not any significant lateral continuity in the image from either the low-frequency geophone or conventional geophone images and no continuity between images. Advancing to the next frequency panels in Figure 4.36 with a

2/4/8/10 Hz Ormsby bandpass filter applied, however, there does appear to be some coherent signal. In the filtered images from both datasets, using conventional geophones and low-frequency geophones, there are continuous events with very low amplitude that are also consistent between images. This is an interesting outcome since the frequency range is entirely below the resonant frequency for the conventional geophone. Proceeding with the remaining filter panels in Figures 4.27 and 4.28 the presence of coherent events remains both within and between images as expected since these frequency ranges (5-10 Hz and 8-16 Hz) are above those seen in Figure 2.26.

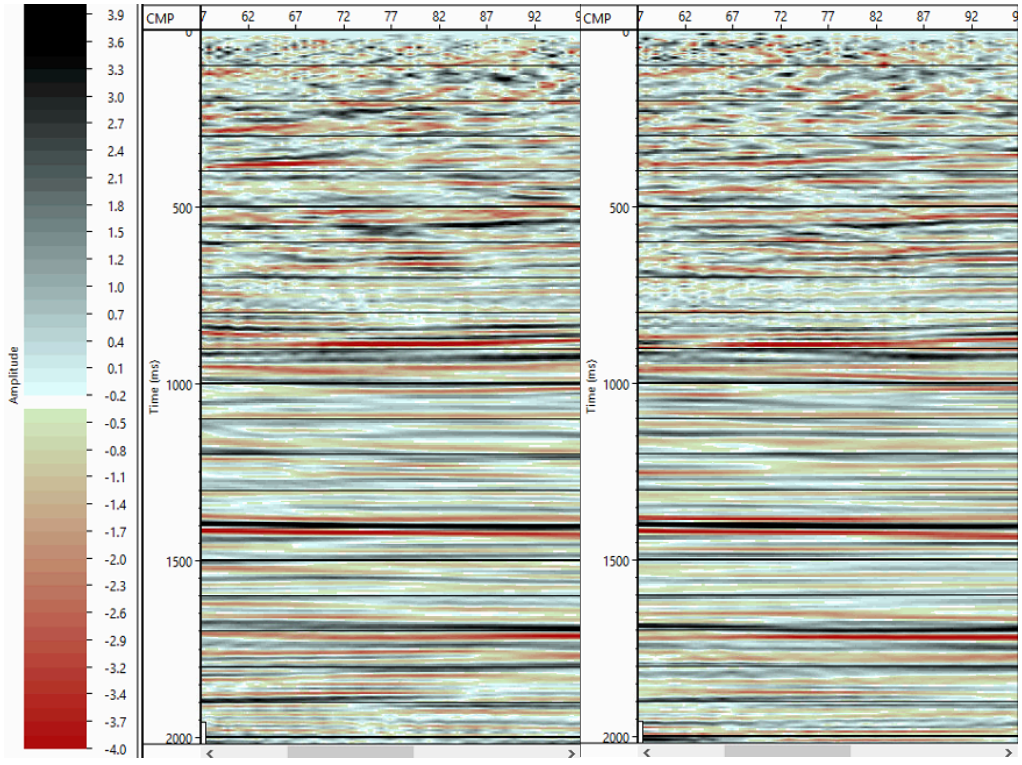

Figure 4.34 The left panel shows the central portion (CMP 57-97) of the fully processed 2D seismic image from the conventional (10 Hz) geophone dataset without any additional frequency filtering. The right panel shows the same central portion of the fully processed 2D seismic image from the low frequency (5 HZ) geophone dataset without any additional frequency filtering.

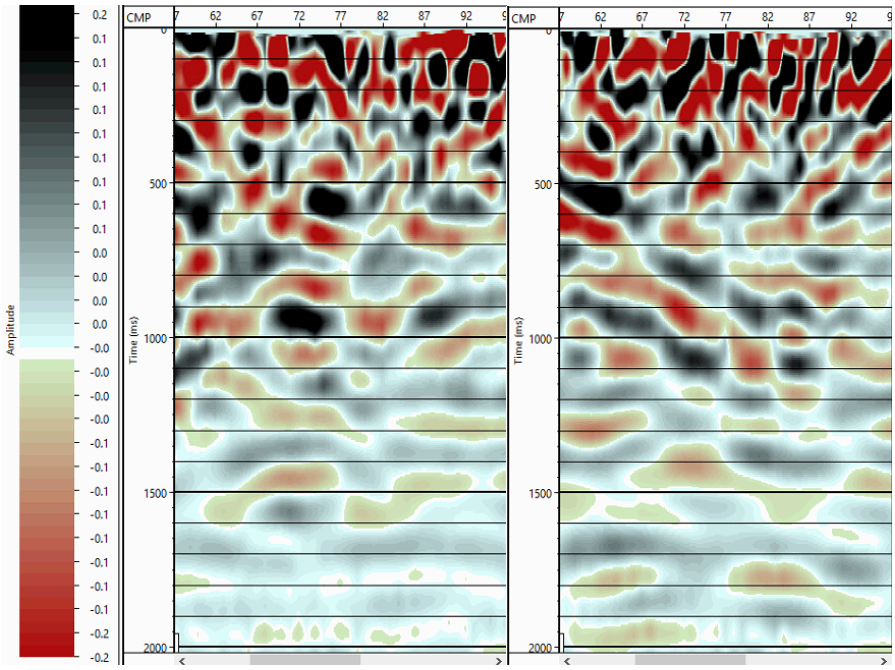

Figure 4.35 The left panel shows the central portion (CMP 57-97) of the fully processed 2D seismic image from the conventional (10 Hz) geophone dataset. The right panel shows the same central portion of the fully processed 2D seismic image from the low frequency (5 HZ) geophone. Both images have a 0/2/5/7 Hz Ormsby bandpass filter applied.

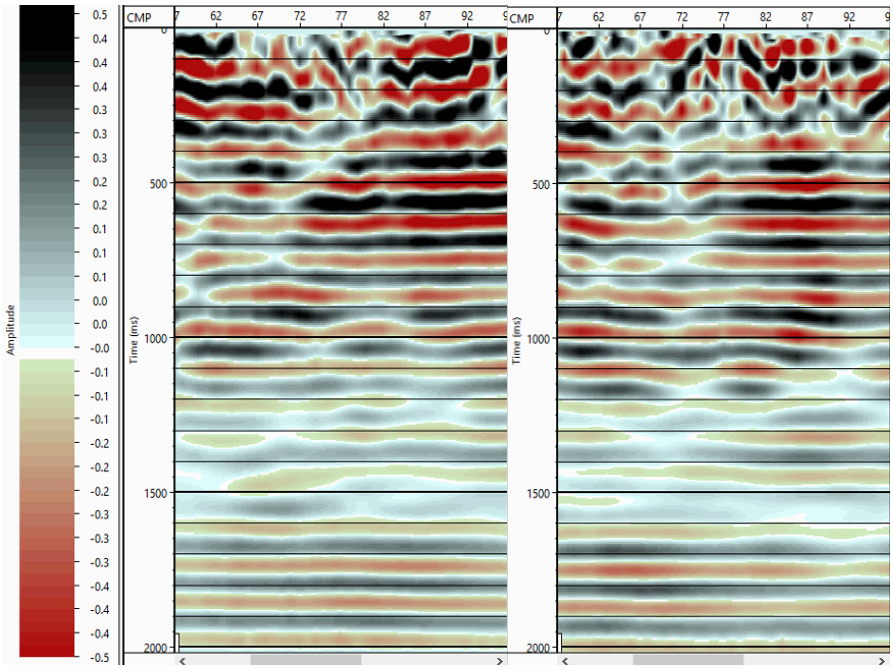

Figure 4.36 The left panel shows the central portion (CMP 57-97) of the fully processed 2D seismic image from the conventional (10 Hz) geophone dataset. The right panel shows the same central portion of the fully processed 2D seismic image from the low frequency (5 HZ) geophone. Both images have a 2/4/8/10 Hz Ormsby bandpass filter applied.

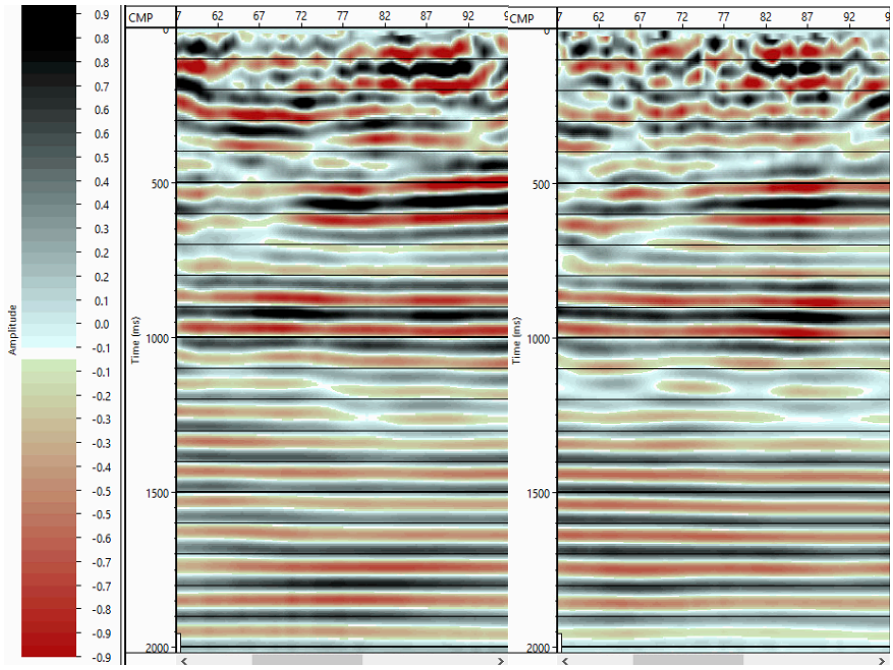

Figure 4.37 The left panel shows the central portion (CMP 57-97) of the fully processed 2D seismic image from the conventional (10 Hz) geophone dataset. The right panel shows the same central portion of the fully processed 2D seismic image from the low frequency (5 HZ) geophone. Both images have a 3/5/10/14 Hz Ormsby bandpass filter applied.

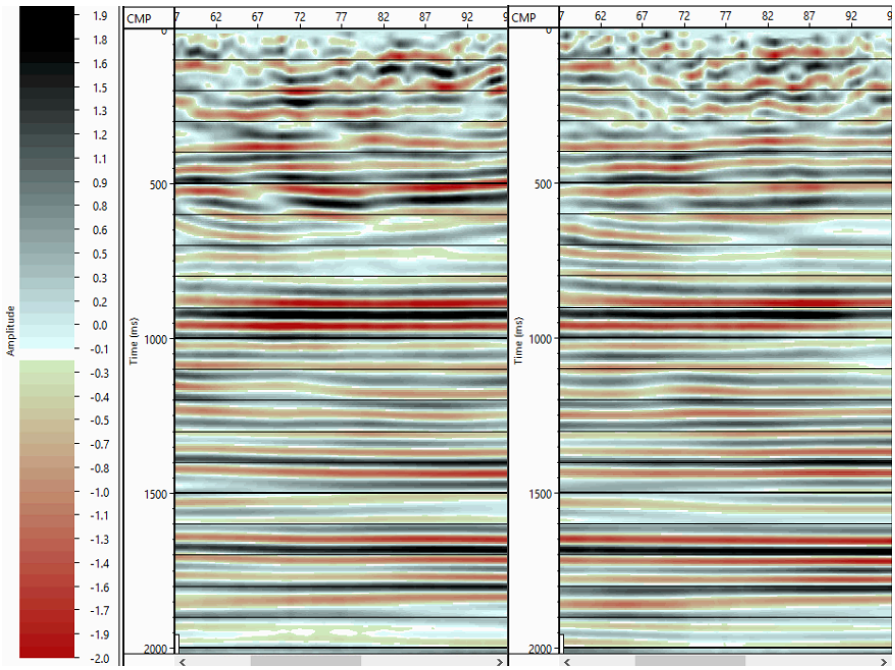

Figure 4.38 The left panel shows the central portion (CMP 57-97) of the fully processed 2D seismic image from the conventional (10 Hz) geophone dataset. The right panel shows the same central portion of the fully processed 2D seismic image from the low frequency (5 Hz) geophone. Both images have a 5/8/16/20 Hz Ormsby bandpass filter applied.

4.8.2 Frequency Spectra

Frequency spectra of the final images with conventional and low-frequency geophones (Figure 4.39) can be compared to directly determine the relative amount of low-frequency content and give insight into the results of the frequency panel tests in section 4.8.1.

Similar to the observations in section 4.4, there does not appear to be a distinct difference between the frequency spectra of the two images, but there is a small difference around the 6 Hz range. At the low-frequency range, below 10 Hz, the image from the low-frequency geophone has a frequency spectrum that is approximately 3 decibels above the frequency spectrum of the conventional geophone. Again, as stated in section 4.3, this is not expected considering the modeled geophones response. Unlike the raw data analyzed in section 4.3, however, the data analyzed here have now undergone significant processing that has likely changed the frequency spectra, leaving uncertainty in this analysis.

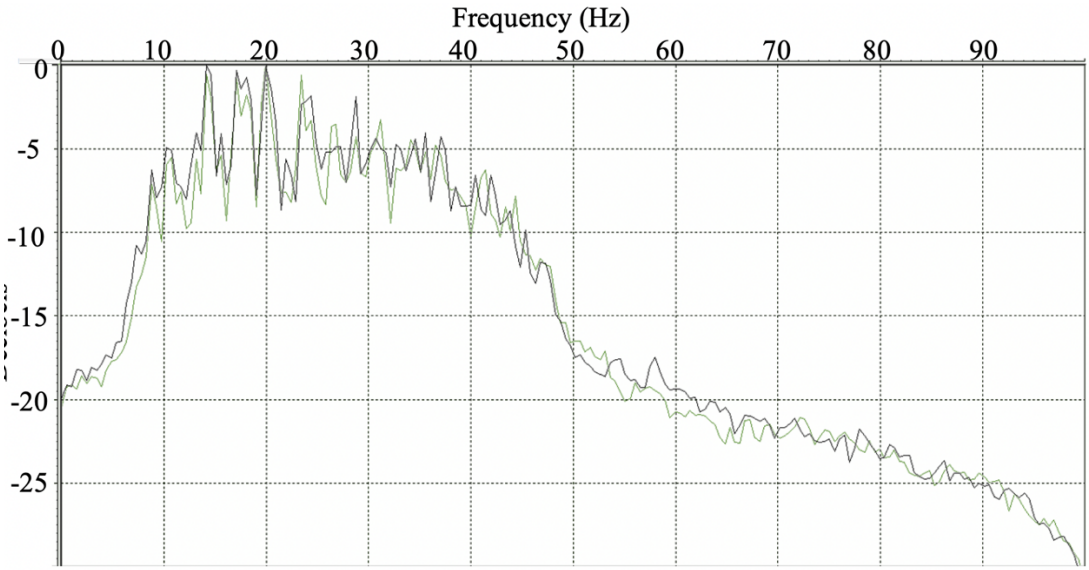

Figure 4.39 Average frequency spectra for conventional (10 Hz) geophone (green) and low frequency (5 Hz) geophone (black).

4.8.3 Wavelet Analysis

Wavelets were extracted in RokDoc from the final processed images of the low-frequency and the conventional geophone datasets to calculate the realized benefit on the wavelet attributes analyzed with synthetic wavelets in Section 2.2. These wavelets are shown in Figure 4.40. The wavelet attributes, peak-to-trough ratio, central lobe width, and central-to-sidelobe energy ratio, are included in Table 4.1. The attributes of the extracted wavelets were as expected. The wavelet extracted from the low-frequency dataset had an increased peak-to-trough ratio and central-to-sidelobe energy ratio while both wavelets had the same central lobe width. The consistency in central lobe width is expected due to its increased dependence upon terminal maximum frequency in comparison to the other wavelet attributes. The increase in peak-to-trough ratio and central-to-sidelobe energy ratio is only about 6% in both cases. This is a relatively small increase when compared to the changes of over 50% in synthetic tests between wavelets with 5 Hz and 10 Hz terminal low frequencies in Section 2.2. This is because of the lack of significant additional coherent low-frequency content in the raw data, as shown in Sections 4.4-4.6, and the final processed datasets, as shown in Section 4.8.

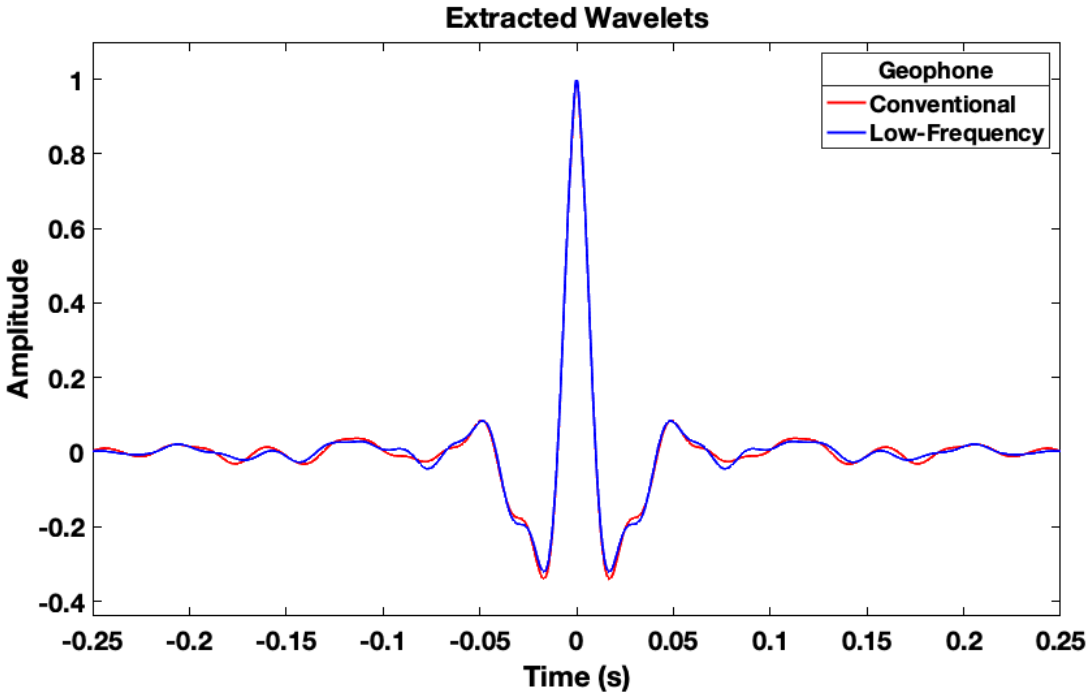

Figure 4.40 Plot of wavelets extracted from the final processed conventional and low-frequency geophone datasets.

Table 4.1 Summary of calculated attributes of the wavelets extracted from the conventional geophone dataset and the low-frequency geophone dataset.

	CONVENTIONAL	LOW-FREQUENCY
PEAK-TO-TROUGH RATIO	2.94	3.12
CENTRAL LOBE WIDTH (MS)	19.7	19.7
CENTRAL/SIDELOBE ENERGY	0.48	0.51

4.9 Discussion

From the inspection of frequency spectra of raw data in Section 4.4, frequency filter panels in Section 4.6, magnitude squared coherence in Section 4.5, and frequency spectra of processed data in Section 4.8.2, there is little evidence that the use of low-frequency geophones has significantly extended the frequency band for this seismic acquisition. This result was unexpected but upon further research may be explained by referring to the first sentence of section 4.1, "The acquisition of broadband seismic data is primarily constrained by two mechanisms, the source, and the receiver". In this study, the independent variable was the receiver, conventional geophones versus low-frequency geophones, but little consideration was given to the source other than a brief description of important characteristics: 15 second, linear, 2 vibes, and 1.5-120 Hz.

In section 2.7 the concept of a low-dwell sweep is introduced to generate a stronger low-frequency source. For low frequencies, the necessary travel of the mass may be larger than the stroke. In other words, the longer the period, the longer the mass has to accelerate. Because of that, according to Winter et al. (2014), the maximum output for a given stroke is proportional to the square of the frequency. This means that in order to obtain an equal force output for low frequencies, more time must be spent generating them, resulting in a low-dwell sweep.

Since the data analyzed had a linear source sweep there may not have been significant enough low-frequency signal generated to produce coherent reflected energy above the noise in the environment. Additional analysis of the available data utilizing conventional and low-frequency geophones with a low-dwell sweep could be done to test this hypothesis.

CONCLUSIONS & FUTURE WORK

This work began with synthetic modeling of Ricker and Klauder wavelets to analyze the effect of changes in band on wavelet properties (peak to trough ratio, central lobe width, and central to sidelobe energy ratio) and stability of those wavelet properties under small changes in band. This analysis resulted in developing relationships between terminal high frequency, terminal low frequency, and/or bandwidth in terms of octaves and the investigated wavelet properties. Most notably, the finding that peak to trough ratio is not dependent upon terminal high frequency or terminal low frequency individually, but octaves of bandwidth. Additionally, the incremental increase in peak to trough ratio grows until 2.7 octaves of band, at which point the incremental increase in peak to trough ratio decreases. This finding suggests that incremental effort in increasing band is rewarded with a greater incremental increase in peak-to-trough ratio below 2.7 octaves, which may be a marker for minimum bandwidth, and that small changes in bandwidth near 2.7 octaves create the largest changes in peak-to- trough ratio (instability of peak to trough ratio).

While there were meaningful results to this synthetic analysis, there is much more that can be done. There remains an opportunity for further analysis through the application of different synthetic sweeps, changes in phase, and addition of random noise. Application and investigation of wavelet properties and stability with the application of these variables could lead to valuable findings and influence thoughts about wavelet stability and optimal seismic frequency band.

The second study of this work pertained to the relationship between signal penetration and frequency. This synthetic modeling demonstrates the importance of low frequencies for long travel paths (deep reflection events) through the inverse relationship of frequency to scattering and

absorption. Expansion of this work could be done in an investigation of long offset diving wave frequency prediction and Q estimation.

The third synthetic modeling exercise of this work aimed at demonstrating the importance of low frequencies investigated the influence of low frequencies on an impedance inversion using a synthetic seismogram generated using a well log from a well near the HD2D line used in the field data analysis. From this exercise, the importance of low frequencies is demonstrated as a lack of low frequencies leads to an impedance inversion lacking the low-frequency trend. This low-frequency trend is often generated synthetically and applied across a field, however, without dense well control, the trend may have a significant error that can propagate into the inversion result.

Further effort into the importance of low frequencies as they pertain to impedance inversion can be done in conjunction with future work with HD2D field data. The field data used in this work involved a low frequency and conventional geophone with a linear vibroseis sweep. In future work, a dataset with a low dwell vibroseis sweep and low-frequency geophone and a dataset with a linear vibroseis sweep and a conventional geophone can be processed, inverted, and compared. Additionally, the work from the Fresnel zone analysis in the fourth independent analysis performed in chapter 3 can be included to determine if a low-frequency trend can be generated across a line with sparse sampling, and if so, is the what is the minimum sampling limit?

Continuing the discussion of the Fresnel zone, Chapter 4 served as a tangential connection to frequency involving the analysis of infill evaluation methods for marine seismic streamer acquisitions. The PSTM forward modeling and Fresnel zone analysis methods of infill evaluation were introduced and discussed. Then the zero offset Fresnel zone equation was expanded to include inline offset and lateral offset in a 3D visualization. Next, the influence of lateral offset was investigated as it pertains to a typical marine seismic streamer acquisition. From this analysis,

the conclusion was that lateral offset is not a significant factor to consider in Fresnel zone-based marine seismic streamer infill evaluation. Finally, to conclude the examination of Fresnel zone applications the possibility of utilizing Fresnel zone analysis for designing a low-frequency acquisition with sparse sampling was discussed.

There is significant work that can be done investigating or applying Fresnel zone resolution concepts to survey design. The most appealing application of the Fresnel zone in extension and continuation of this work is through subsampling low-frequency receiver stations to determine the sampling needed to deliver a low-frequency seismic volume and compare the sampling to Fresnel zone sampling requirements for full coverage at the frequency of interest. Investigation of this could have far-reaching implications into the design of outrageously expensive ocean bottom fiberoptic cable installations or simultaneous ocean bottom node and streamer marine acquisitions.

The final undertaking of this work was the processing and analysis of simultaneously acquired datasets with different conventional (10 Hz) and low frequency (5 Hz) geophones. The first objective in this chapter was to familiarize the reader with the mechanics of a geophone and model the response of the conventional and low-frequency geophones from manufacturer specifications. Next, the frequency spectra of the raw data were analyzed. The results from this analysis did not agree well with the modeled geophone response, but there was a slight increase in low-frequency content below 10 Hz on the low-frequency geophone relative to the conventional geophone. Concluding the analysis of the raw seismic was the calculation of magnitude squared coherence between the datasets. This calculation revealed similar frequency content (MSC$\approx$ 0.9) in both the low-frequency and conventional geophone datasets down to about 3 Hz. After analysis of the raw data, both datasets were processed individually to create the best image possible and retain as much low-frequency content as possible. Finally, the low-frequency content of the final

processed images was compared through filter panels and frequency spectra. The filter panels showed coherent signal within and between the images of both datasets in the 4-8 Hz frequency range and above. This was unexpected since the 4-8 Hz frequency range is below the resonant frequency for the conventional geophone. Additionally, if the conventional geophone image produced a coherent signal in this range, it would be expected that the low-frequency geophone image would produce a coherent signal in the 2-4 Hz range and it did not. Following the analysis of the frequency panels, the analysis of the frequency spectra from the processed data yielded similar results as the analysis of the raw data. From the observation of frequency spectra of raw data in section 4.3, frequency filter panels in section 4.5.2 and frequency spectra of processed data in section 4.5.2, there is little evidence that the use of low-frequency geophones has significantly extended the frequency band for this seismic acquisition. This result is discussed in the final section of the chapter and hypothesized to be a result of insufficient low-frequency source input.

As mentioned, several times throughout the entirety of this work, the HD2D dataset donated to the University of Houston by Apache Corporation is immense and full of possibilities. The most direct extension of this work involving the HD2D field data and the investigation into low frequencies is to test the hypothesis that the low-frequency energy of the source was insufficient to produce coherent reflected energy above the noise in the environment. This could be done by processing the dataset that uses the low-dwell sweep and low-frequency geophone and comparing that result to the result of the linear sweep and low-frequency geophone. Other extensions of this work include investigations into sampling intervals for source and receiver, one vibroseis versus two vibroseis or 8-second versus 15-second vibroseis configuration, and sampling requirements for low-frequency acquisition. Investigations into any of these topics will be valuable to geophysical operations and survey design.

BIBLIOGRAPHY

Baan, M. v. d. 2012, Importane of wavelet phase stability in seismic interpretation.

Bale, R. A., and R. R. Stewart, 2002, The impact of attenuation on the resolution of multicomponent siesmic data: CREWES Research Report, **14**, 1-21.

Barzilai, A., 1999, Geophone Research, http://micromachine.stanford.edu/projects/geophones/GeophoneResearch.html, accessed January 18 2020.

Batzle, M., and Z. Wang, 1992, Seismic properties of pore fluids: GEOPHYSICS, **57**, no. 11, 1396-1408. http://dx.doi.org/10.1190/1.1443207.

Bourbie, T., O. Coussy, and B. Zinszner, 1987, Acoustics of Porous Media: Gulf Publishing Company.

Castagna, J. P., M. L. Batzle, and R. L. Eastwood, 1985, Relationships between compressional-wave and shear-wave velocities in clastic silicate rocks: GEOPHYSICS, **50**, no. 4, 571-581. http://dx.doi.org/10.1190/1.1441933.

Cui, T., and G. F. Margave, 2014, Seismic wavelet estimation: CREWES Research Report, **26**, 1-16.

Day, A., and T. o. Rekdal, 2005, Determining infill specifications based on geophysical criteria, SEG Technical Program Expanded Abstracts 2005, 80-83.

Dey, A. K., 1999, An Analysis of Seismic Wavelet Estimation, University of Calgary.

Dragoset, B., and J. Gabitzsch, 2007, Introduction to this special section: Low-frequency seismic: The Leading Edge, **26**, no. 1, 34-35. http://dx.doi.org/10.1190/1.2431829.

Eide, K. E., 2012, CO2 Sequestration: The effect of carbonate dissolution on reservoir rock integrity, Norwegian University of Science and Technology.

Google, 2019, Google Earth, earth.google.com/web, accessed April 15 2019.

Han, D.-h., and M. L. Batzle, 2004, Gassmann's equation and fluid-saturation effects on seismic velocities: GEOPHYSICS, **69**, no. 2, 8.

Han, D.-h., and M. Sun, 2012, Velocity and density of CO2 -oil miscible mixtures: SEG Annual Meeting.

Hirscha, W. K., G. Sedgwick, and Z. Wang, 1990, Seismic Monitoring In Enhanced Oil Recovery: Annual Technical Meeting, 14.

Hons, M. S., 2008, Seismic Sensing: Comparison of geophones and accelerometers using laboratory and field data, University of Calgary.

Jinping, X., H. Lixin, L. Bin, Z. Guoyong, and Z. Jian, 2018, Design and application of nonlinear sweep signal for vibroseis, International Geophysical Conference, Beijing, China, 24-27 April 2018, 98-101.

Kallweit, R. S., and L. C. Wood, 1982, The limits of resolution of zero-phase wavelets: GEOPHYSICS, **47**, no. 7, 1035-1046. http://dx.doi.org/10.1190/1.1441367.

Karslı, H., and D. Dondurur, 2013, A procedure to reduce side lobes of reflection wavelets: A contribution to low frequency information: Journal of Applied Geophysics, **96**, 107-118. http://dx.doi.org/10.1016/j.jappgeo.2013.07.002.

Kjartansson, E., 1979, Constant Q-Wave Propagation and Attenuation: Journal of Geophysical Research, **84**, no. B9, 4737-4748.

Kumar Ray, A., and S. Chopra, 2016, Building more robust low-frequency models for seismic impedance inversion: First Break, **34**, no. 2118. http://dx.doi.org/10.3997/1365-2397.2016005.

Ludwig-Maximilians-University. 2006, Scattering and Attenuation.

Malekpour, S., J. A. Gubner, and W. A. Sethares, 2018, Measures of generalized magnitude-squared coherence: Differences and similarities: Journal of the Franklin Institute, **355**, no. 5, 2932-2950. http://dx.doi.org/https://doi.org/10.1016/j.jfranklin.2018.01.014.

Martin, N., and R. Stewart, 1994, The effect of low frequencies on seismic analysis.

Mavko, G., T. Mukerji, and J. Dvorkin, 2009, The Rock Physics Handbook. Second ed: Cambridge University Press.

Maxwell, P., and M. Lansley, 2011, What receivers will we use for low frequencies?, SEG Technical Program Expanded Abstracts 2011, 72-76.

Michel, L., Y. Lafet, P. Doyen, A. Smith, and CGGVeritas. 2015, Benefits of Broadband Sesimc Data for Rock Property Inversion.

Miller, R. D., A. E. Raef, A. P. Byrnes, and W. E. Harrison. 2006, 4-D High-Resolution Seismic Reflection Monitoring of Miscible CO2 Injected intoa Carbonate Reservoir. University of Kansas Center for Research and Kansas Geological Survey.

Monk, D., and P. Young, 2009, METHOD FOR DETERMINING ADEQUACY OF SEISMIC DATA COVERAGE OF A SUBSURFACE AREA BEING SURVEYED AND ITS APPLICATION TO SELECTING SENSOR ARRAY GEOMETRY.

Monk, D. J., 2010, Reducing infill requirements using Fresnel zone binning and steerable streamers, SEG Technical Program Expanded Abstracts 2010, 3802-3806.

Neelima, S., A. Saritha, K. S. Ramesh, and S. K. Rao. 2018, Application of klauder wavelet for generation of synthetic seismic signals.

Padhy, S., and N. Subhadra, 2013, Separation of intrinsic and scattering seismic wave attenuation in Northeast India: Geophysical Journal International, **195**, no. 3, 1892-1903. http://dx.doi.org/10.1093/gji/ggt350.

Ruppel, S. C. 2006, SUBREGIONAL DEVELOPMENT OF RESERVOIR POROSITY AT A MAJOR PERMIAN UNCONFORMITY.

Smith, M. L., T. L. Fischer, and J. A. Scales, 1991, Inverse modeling and global search methods, SEG Technical Program Expanded Abstracts 1991, 738-741.

Smith, T. M., C. H. Sondergeld, and C. S. Rai, 2003, Gassmann fluid substitutions: A tutorial: GEOPHYSICS, **68**, no. 2, 430-440. http://dx.doi.org/10.1190/1.1567211.

SPE, 2016, Gassmann's equation for fluid substitution, http://petrowiki.org/Gassmann's_equation_for_fluid_substitution, 2016.

Tellier, N., and F. Ollivrin, 2019, Low Frequency Vibroseis: current achievements and the road ahead?: First Break, **37**, 49-54.

ten Kroode, F., S. Bergler, C. Corsten, J. W. de Maag, F. Strijbos, and H. Tijhof, 2013, Broadband seismic data — The importance of low frequencies: GEOPHYSICS, **78**, no. 2, WA3-WA14. http://dx.doi.org/10.1190/geo2012-0294.1.

Toksöz, M. N., D. H. Johnston, and Society of Exploration Geophysicists, 1981, Seismic Wave Attenuation: Society of Exploration Geophysicists.

United States Department of Energy, 2011, Enhanced Oil Recovery, https://www.energy.gov/fe/science-innovation/oil-gas-research/enhanced-oil-recovery, accessed January 10 2020.

Wei, Z., 2018, Vibroseis controllers: Are your low-frequency sweeps in phase?, SEG Technical Program Expanded Abstracts 2018, 211-215.

Winter, O., A. Leslie, F. Lin, P. Maxwell, and CGG, 2014, Acquiring low frequencies onshore: sweep, sensors, sampling and stories: CSEG Recorder, **39**, no. 06, 36-41.

Yilmaz, O., 2001, Seismic Data Analysis. Edited by M. R. Cooper. 2 vols. Vol. I-II,

Investigations into Geophysics: Society of Exploration Geophysics.

Zeng, H., and M. Backus, 2005, Interpretive advantages of 90°-phase wavelets: Part 1 — Modeling: GEOPHYSICS, **70**, C7-C15. http://dx.doi.org/10.1190/1.1925740.

APPENDICES

APPENDIX A– FLUID SUBSTITUTION

Investigation of change in seismic response due to CO2 saturation by Gassmann fluid substitution

INTRODUCTION

Synthetic velocity models for limestone and sandstone are manipulated, using Gassmann's equations, to investigate the seismic response of CO_2 saturation. These manipulations produce results defining the relationship between % change in reflectivity and % CO_2 saturation with varying initial fluids for each model. The relationship between % change in reflectivity and % CO_2 saturation is investigated theoretically through acoustic impedance changes driven by bulk modulus and bulk density changes. The results of this exercise serve as a base simulation that will evolve in complexity and accuracy with real data and future work to account for violated assumptions in the manipulation.

Objective

The objective of this study is to investigate and quantify the effect of CO_2 injection on seismic data through fluid substitution modeling. As seen in equation (9), acoustic impedance is directly affected by change in bulk modulus and change in fluid density. Utilizing Gassmann's equations, these changes are accounted for to compute estimated velocities for a rock matrix saturated with fluids of different properties. From the computed velocities and known densities, acoustic impedance can be calculated. Acoustic impedance change can then be used to quantify the amount of CO_2 saturation, or similarly, the amount of reservoir swept between time-lapse seismic surveys.

Caveats

Gassmann fluid substitution models have several assumptions (SPE, 2016):

- Porous material is isotropic, elastic, monomineralic, and homogeneous
- Pore space is well connected and in pressure equilibrium (zero frequency limit)

- Medium is a closed system with no pore fluid movement across boundaries
- No chemical interaction between fluids and rock frame (shear modulus remains constant)

In this model, these assumptions will be upheld for simplicity. In a more realistic model, pressure deviations will be present due to the injection, there will likely be anisotropy, and in some formations there will be changes in porosity due to chemical interaction between the CO_2 and the rock frame (especially in carbonates). (Eide, 2012)

This model also applies a simplifying assumption to the properties of CO_2. In this model, CO_2 is mixed with other fluids immiscibly, when in reality, at the reservoir temperature and pressure used in this model, the CO_2 would be miscible with oil and therefore require a more complicated fluid property model.

With these caveats in mind, this model serves as a base investigation that will evolve in complexity and accuracy with future work.

SYNTHETIC DATA GENERATION

The first task in this investigation was to generate synthetic velocity logs for clean sandstone and clean limestone with porosity ranging between 4% and 14% (These porosity values were selected based on porosity values of a formation of interest in West Texas).

Sandstone Model

For the sandstone velocities, the Castagna relation was applied.

Castagna Relation (Castagna et al., 1985):

P-wave velocity $\left(V_p \text{ in } \frac{\text{m}}{\text{s}}\right)$ and S-wave velocity $\left(V_s \text{ in } \frac{\text{m}}{\text{s}}\right)$ empirical relation with porosity (ϕ) for brine saturated siliciclastics.

$$V_p = 5.81 - 9.42\phi$$

$$V_s = 3.89 - 7.07\phi$$

Following the Castagna relation, the sandstone model used water as the in-situ fluid, and quartz as the matrix mineral (properties shown in Table A.1).

Table A.1 – Properties of sandstone model matrix and in-situ fluid. Bulk modulus (K) and density (ρ).

	Material	K (Pa)	$\rho\left(\frac{\text{kg}}{\text{m}^3}\right)$
Matrix	Quartz	3.7E10	2650
Fluid	Water	2.2E9	1000

With these parameters, the velocities ranged from 4491 $\frac{\text{m}}{\text{s}}$ at 14% porosity to 5433 $\frac{\text{m}}{\text{s}}$ at 4% porosity. These values fall well within the proposed maximum (5520 $\frac{\text{m}}{\text{s}}$) and minimum (3130 $\frac{\text{m}}{\text{s}}$) velocities given in **THE ROCK PHYSICS HANDBOOK** (Mavko et al., 2009) which gives increased confidence to the suitability of the model.

Limestone Model

For the limestone velocities, an empirical relation from Han and Batzle was applied.

Limestone Relation (Han and Batzle, 2004):

P-wave velocity $\left(V_p \text{ in} \frac{\text{m}}{\text{s}}\right)$ and S-wave velocity $\left(V_s \text{ in} \frac{\text{m}}{\text{s}}\right)$ empirical relation with porosity (ϕ) for dry limestone.

$$V_p = 6.19 - 9.80\phi$$

$$V_s = 3.20 - 4.90\phi$$

Following the limestone relation from Han and Batzle (2004), this model used air as the in-situ fluid, and calcite as the matrix mineral. After this initial model was created, a fluid substitution was performed to change the in-situ fluid to water because air was not expected in the reservoir. This also standardized the model starting conditions. The properties of the model components are shown in Table A.2.

Table A.2 – Properties of limestone model matrix, initial in-situ fluid, and final model in-situ fluid. Bulk modulus (K) and density (ρ).

	Material	K (Pa)	$\rho\ \left(\frac{\text{kg}}{\text{m}^3}\right)$
Matrix	Calcite	7.3E10	2650
Fluid 1	Air	1.4E5	1.2
Fluid 2	Water	2.2E9	1000

With these parameters, the velocities ranged from 4851 $\frac{\text{m}}{\text{s}}$ at 14% porosity to 5838 $\frac{\text{m}}{\text{s}}$ at 4% porosity. The maximum value is near the upper limit of the proposed maximum velocity (5800 $\frac{\text{m}}{\text{s}}$) and minimum value is well above the proposed minimum velocity (3130 $\frac{\text{m}}{\text{s}}$) given in **THE ROCK PHYSICS HANDBOOK** (Mavko et al., 2009). While the maximum velocity of the model was higher than expected, it exceeded the proposed maximum by less than 1%. This deviation was regarded as acceptable and the model was finalized.

Shale Model

In order to give an example in terms of change in reflectivity, a shale model was used as the formation overlying the sandstone or carbonate formation. The shale formation was unchanged

and not involved in the fluid substitution. The properties of this model are shown in Table A.3. These properties were taken from average velocities of shale published in **ACOUSTICS OF POROUS MEDIA** (Bourbie et al., 1987).

Table A.3 – Shale model velocity (V_p), density (ρ), and acoustic impedance (AI).

Formation	$V_p \left(\frac{\mathrm{m}}{\mathrm{s}}\right)$	$\rho \left(\frac{\mathrm{kg}}{\mathrm{m}^3}\right)$	AI
Shale Model	1800	2200	3.96E6

METHODS

Both models were manipulated according to the same methods. For simplicity, "the model" refers to both the sandstone and limestone model in this section.

Changing Porosity and Fluid

In order to investigate the influence of porosity on velocity and acoustic impedance for different fluid types, the model was manipulated using Gassmann's equations for fluid substitution. Gassmann's equation provides a relatively simple estimate of the change in bulk modulus, described previously in the background portion of the introduction as dK, with changing fluids. The equations are composed of two parts. First, the bulk modulus of the dry rock frame must be calculated. Second, the bulk modulus of the desired fluid saturated rock is computed.

Gassmann's Equations (Smith et al., 2003):

Equation (10) is the basic concept behind Gassmann's equations. The bulk modulus of the fluid

saturated rock $\left(K_{sat_2}\right)$ is related to the bulk modulus of the dry rock frame $\left(K_{dry}\right)$ and the change in bulk modulus from saturating the dry rock frame with a new fluid (dK_{d2}).

$$K_{sat_2} = K_{dry} + dK_{d2} \tag{10}$$

Equation (11) is the Gassmann equation for bulk modulus of the dry rock frame $\left(K_{dry}\right)$ in terms of the bulk modulus of the in-situ fluid saturated rock $\left(K_{sat_1}\right)$, porosity (ϕ), bulk modulus of the mineral composing the rock matrix (K_{ma}), and the bulk modulus of the in-situ fluid $\left(K_{fl_1}\right)$.

$$K_{dry} = \frac{K_{sat_1}(1-\phi) + \frac{\phi K_{sat_1} K_{ma}}{K_{fl_1}} - K_{ma}}{\frac{K_{sat_1}}{K_{ma}} + \frac{\phi K_{ma}}{K_{fl_1}} - (1+\phi)} \tag{11}$$

Equation (12) is the Gassmann equation for bulk modulus of the new fluid saturated rock frame $\left(K_{sat_2}\right)$ in terms of the bulk modulus of the dry rock frame $\left(K_{dry}\right)$, porosity (ϕ), bulk modulus of the mineral composing the rock matrix (K_{ma}), and the bulk modulus of the desired fluid $\left(K_{fl_2}\right)$.

$$K_{sat_2} = K_{dry} + \frac{\left(1 - \frac{K_{dry}}{K_{ma}}\right)^2}{\frac{\phi}{K_{fl_2}} + \frac{1-\phi}{K_{ma}} - \frac{K_{dry}}{K_{ma}^2}} \tag{12}$$

To relate the equation (10) to the change in bulk modulus between two different fluid saturations and eliminate the K_{dry} term, equation (13) can be applied to arrive at equation (14) and

more simply, equation (15).

Equation (13) relates K_{dry} to the K_{sat_1} and change in bulk modulus between the dry rock and fluid saturated rock (dK_{1d}).

$$K_{dry} = K_{sat_1} + dK_{1d} \tag{13}$$

Equation (14) substitutes equation (13) into equation (10) relating K_{sat_2} to K_{sat_1}, the change in bulk modulus between the in-situ fluid saturated rock and the dry rock (dK_{1d}), and the change in the bulk modulus between the dry rock and the new fluid saturated rock (dK_{d2}).

$$K_{sat_2} = K_{sat_1} + dK_{1d} + dK_{d2} \tag{14}$$

Combining $dK_{1d} + dK_{d2}$ in equation (14) into one change in bulk modulus between fluid saturated rocks (dK_{12}) and rearranging terms gives equation (15).

$$dK_{12} = K_{sat_2} - K_{sat_1} \tag{15}$$

This change in bulk modulus along with the known changes in density allows Gassmann fluid substitution to calculate velocities for different fluid saturations. Equation (3) shows the dependence of velocity on these parameters.

The resulting velocities of the model saturated with different fluid types were plotted against porosity and analyzed.

The bulk density was then calculated using equation (4) at different porosities for the different fluids and applied to the model to create acoustic impedance values. The resulting model acoustic impedance values from the model, saturated with different fluid types, were plotted against porosity and analyzed.

Fluid Mixing at Constant Porosity

In order to investigate the influence of fluid mixtures on velocity and acoustic impedance, the starting model was altered to constant porosity and therefore constant velocity for several in-situ fluids: Oil, Gas, and Water. The porosity in this model was 10% and the velocities for the in-situ fluids at 10% porosity were obtained from the previous model manipulation. From the 100% in-situ fluid saturated rocks, Gassmann fluid substitution was performed for mixtures of in-situ fluid and CO_2 with increasing CO_2 content from 0% to 100%. When mixing the fluids, the fluid density was calculated using a simple weighted average and the bulk modulus of the fluid mix $\left(K_{fl_{mix}}\right)$ was calculated using an inverse weighted average also known as Wood's equation (Batzle and Wang, 1992):

$$K_{fl_{mix}} = \frac{1}{\frac{\Phi_1}{K_1} + \frac{\Phi_2}{K_2}} \tag{16}$$

The resulting model velocities and acoustic impedance values with different fluid mixtures were plotted against CO_2 saturation and analyzed.

DATA ANALYSIS AND INTERPRETATION[1]

Sandstone: Changing Porosity and Fluid

From the plot of velocity vs. porosity, (Figure A-1) the relative velocities of the rock saturated with different fluids. The velocities of the rock in terms of fluid are in the following order from fastest to slowest: Water, Oil, Gas, and CO_2. The difference of velocities between rocks of different fluid saturations increases with increasing porosity. This is consistent with expectations because as porosity increases, the influence of the pore fluid properties increases.

When analyzing the acoustic impedance response of different fluid saturated rocks at varying porosity, (Figure A-2) a slightly different story unfolds. The velocities of the rock in terms of fluid are, from fastest to slowest: Water, Oil, CO_2, and Gas. The difference between the acoustic impedance and velocity output is that in the velocity output, the CO_2 case is slower than the Gas case, while in the acoustic impedance output, the acoustic impedance of the CO_2 case is higher than the Gas case. This isn't directly apparent due to the fact that acoustic impedance is velocity multiplied by bulk density. This difference, however, can be accounted for in the lower density of the Gas compared to the CO_2 having a large influence on the relationships. This result is consistent with the expected result from equation (7). The low density of the gas would increase velocity since the density term is in the denominator of the velocity equation (equation (1)), and conversely decrease acoustic impedance since density is in the numerator for the acoustic impedance equation (equation (7)).

Sandstone: Fluid Mixing at Constant Porosity

The plot of velocity vs. CO_2 saturation (A.3) details a complicated relationship. The form

[1] From this point forward, "velocities" refers to P-wave velocities.

of these lines, representing different starting fluids, varies due to the difference in bulk modulus and bulk density of the associated fluids and their different impacts on the velocity equation.

After examining the change in bulk modulus (Figure A-4) and bulk density (Figure A-5) with CO_2 saturation for different fluids and inspecting the velocity equation, (equation (2)) the relationship can be more adequately understood. The velocity equation is dependent upon $\sqrt{(K + dK)}$ and $\frac{1}{\sqrt{(\rho_b + d\rho_b)}}$. The K and ρ_b are most important in determining the initial velocity, however, as the model is saturated with different fluid mixtures, the changes in bulk modulus and change in bulk density determine the shape of the line. Figure A-5 shows the relationship between bulk modulus and CO_2 saturation. As CO_2 saturation increases, the change in bulk modulus, or slope of the line, decreases for Water and Oil and increases for Gas. Figure A-4 shows the relationship between bulk density and CO_2 saturation. As CO_2 saturation increases, the change in bulk density, or slope of the line, remains constant for every type of fluid saturation. Revisiting the velocity vs. CO_2 saturation plot, it is now possible to understand the relationships for the different initial fluid saturations in terms of dK and $d\rho$. The presence of a minimum in Figure A-3 can also be interpreted from this relationship. The minimum is a result the change in bulk modulus is of equal weight to the velocity as the change in density.

When analyzing the acoustic impedance response (Figure A-6) of the same manipulation, a similar and expected result is achieved. The acoustic impedance response resembles the velocity vs. CO_2 saturation plot adjusted by multiplying the values by bulk densities for varying fluid saturations. To more easily understand the acoustic impedance, it is useful to convert acoustic impedance to reflectivity (equation (18)) using a synthetic overlying formation. The shale model was used for this exercise (See Shale Model).

Reflectivity:

The reflectivity is a measure of the predicted amplitude of a reflection of a normal incidence wave from impedance contrast. Here, Z_a is the impedance of the a layer, numbered in increasing order with depth. Impedance is the product of bulk density of the a layer multiplied by the velocity of the a layer (equation (17)).

$$Z_a = \rho_{b_a} V_a \tag{17}$$

$$R = \frac{Z_2 - Z_1}{Z_1 + Z_2} \tag{18}$$

From the reflectivity vs. CO_2 saturation plot, (Figure A-7) it is easier to see the magnitude of the change in reflectivity with changing CO_2 saturation. This can be further simplified by quantifying the percent change in reflectivity with increasing CO_2 saturation (Figure A-8). From Figure A-8, the change in reflectivity can be directly related to change in fluid saturation in a reservoir with a known in-situ fluid.

Limestone: Changing Porosity and Fluid

For the limestone model, the velocity vs. porosity plot (Figure A-9) yields a similar result to that of the sandstone model. The velocities of the rock in terms of fluid are in the following order from fastest to slowest: Water, Oil, Gas, and CO_2. Just as in the sandstone model, the difference of velocities between rocks of different fluid saturations increases with increasing

porosity. Again, this is consistent with expectations because as porosity increases, the influence of the pore fluid properties increases.

When analyzing the acoustic impedance response of different fluid saturated rocks at varying porosity (Figure A-10), again, the same response is observed in the limestone model as the sandstone model.

Limestone: Fluid Mixing at Constant Porosity

The fluid mixing at constant porosity exercise performed on the limestone model also yielded similar results to that of the sandstone model. Figures A-11 to A-13 convey the results of this exercise.

Delving into much detail regarding the results of this exercise will be avoided due to the large uncertainty involved with the possible change in porosity in CO_2 saturated carbonates. This change will be covered in the discussion and future work sections.

DISCUSSION

With the presented data, it is necessary to comment on the legitimacy of the relations and provide general insight into areas of potential error.

To address the legitimacy of the data presented, several parameters must be investigated. These parameters include the initial velocity models, the bulk modulus and density constants applied for each material, and the equations used to perform the manipulations.

Models

The initial velocity models were vetted by comparison to typical ranges in velocities their

respective rock types, however, the relations used were still empirical. The velocity models, therefore, may be improved by utilizing a theoretical relation. Ideally, the synthetic velocity models would be replaced with borehole sonic logs combined with core analysis to convert this synthetic investigation into a model that could be applied to real data. With the incorporation of real borehole seismic data, however, there may be discrepancies between the velocities seen by a borehole sonic tool of relatively high frequency and surface seismic at lower frequencies.

Despite the opportunity to incorporate other models or real data to replace the models used in this paper, there is little evidence to suggest the models used compromise the legitimacy and efficacy of the results.

Constants

The bulk modulus and density constants for this paper were obtained through various sources and material property calculators. When using a material property calculator, the input pressure and temperature conditions were 3720 psi and 200°F respectively. These pressure and temperature conditions are estimates based on a reservoir at 8000 ft. TVD. The bulk modulus and density constants could be improved by integrating a single material property calculator or laboratory measurements on real materials from core samples into the exercise. There is also a possibility of error due to inaccurate temperature and pressure assumptions. The bulk modulus of some materials used are very sensitive to pressure and temperature variations and, therefore, could alter the output. Unfortunately, since the data used is entirely synthetic, there is no way to determine error in the bulk modulus and densities used in this particular exercise. Therefore, while there may be more accurate constants, there is no evidence to suggest the values used compromised the legitimacy or efficacy of the results.

Equations

There were a number of equations presented in this paper that must be addressed. Many of the equations were simple derivations to show relations between variables underlying the basic equations governing seismic velocity and acoustic impedance. These equations do not present concerns when addressing the legitimacy of the results. The equations that present the greatest concern are constituents of Gassmann's equations, as well as the equation used for the estimated bulk modulus of fluid mixtures. The problem with the application of Gassmann's equations in this exercise comes in several forms, previously addressed in "Caveats". The most blatant violation warrants repeating: chemical interaction between CO_2 and carbonates changes porosity and other physical properties of the formation that are not supported by Gassmann's equations. The issue with the equation used for the estimated bulk modulus of a fluid mixture (equation (16)) is that the properties of CO_2 under the pressure and temperature conditions at which this exercise was performed were not accounted for adequately. At the pressure and temperature conditions this exercise was performed, CO_2 is in a supercritical state and is miscible with the fluids used. The miscibility further complicates the calculation since it is a function of the properties into which it dissolves. For example, miscibility of CO_2 in Oil varies, not only by temperature and pressure, but also with Oil API or specific gravity.

The potential errors from the equations used could have the greatest influence on the manipulations that varied CO_2 saturation in both models, and all manipulations utilizing the limestone model. These errors require additional investigation and should caution the reader when viewing results of manipulations that may have significant error.

SUMMARY AND FUTURE WORK

The objective of this exercise, as outlined in the beginning of the paper, was to "investigate and quantify the effect of CO_2 injection on seismic data through fluid substitution modeling". By utilizing two synthetic models, sandstone and limestone, this objective was achieved. The results are most easily observed in Figure A-8 and Figure A-9. These figures directly relate the % change in acoustic impedance to the % CO_2 saturation for different initial fluid saturations. From this figure, time-lapse seismic data may be quantitatively interpreted to determine the fluid saturation in a formation of interest due to the observed reflection amplitude change. It is important to understand that these figures are not applicable to all seismic time-lapse interpretations and should be adjusted to fit the parameters of the formation of interest using real data. These figures do, however, provide a useful result to a base investigation that will evolve in complexity and accuracy with real data and future work.

As mentioned in the *"Discussion*" section, there are several aspects of the exercise that need to be adjusted to reduce the potential error in the results. These adjustments are:

- Adapt Gassmann's equations to account for changing porosity and rock frame stiffness
- Derive and apply a fluid property model to account for miscibility of CO_2

There is some work being done to quantify the change in porosity due to CO_2 injection by Eide and USGS (Eide, 2012). These values are highly dependent upon the chemical structure of the formation of interest and, therefore, are not able to be well characterized as a generalization. In order to account for the change in porosity and rock frame stiffness, laboratory measurements should be performed on samples from the formation of interest. These measurements will provide the best estimates of the change in porosity and rock properties of the matrix. Even with these

estimates, however, the assumption must be made that the formation is homogeneous. This assumption is almost certainly violated and could cause further issues in interpreting the effect of CO_2 in seismic data.

A significant amount of effort has been dedicated to investigating the properties of CO_2 under varying conditions by Han and Sun. These investigations have yielded "preliminary velocity and density models… within measured conditions of$40°\mathrm{C} \leq T \leq 100°C,\ 20MPa \leq P \leq 100MPa, and\ GOR < 310\mathrm{L/L}$" (Han and Sun, 2012). These models can be applied to more adequately determine constants, such as bulk modulus, for fluid mixtures.

With the modifications outlined above, the manipulations, utilizing real data, may deliver results, accurate enough to predict changes in reflectivity or reflection amplitude based on CO_2 saturation, which can be utilized in the interpretation of time-lapse seismic data.

REFERENCES

Batzle, M., and Wang, Z., 1992, Seismic properties of pore fluids: GEOPHYSICS, v. 57, no. 11, p. 1396-1408.

Bourbie, T., Coussy, O., and Zinszner, B., 1987, Acoustics of Porous Media, United States, Gulf Publishing Company.

Castagna, J. P., Batzle, M. L., and Eastwood, R. L., 1985, Relationships between compressional-wave and shear-wave velocities in clastic silicate rocks: GEOPHYSICS, v. 50, no. 4, p. 571-581.

Eide, K. E., 2012, CO2 Sequestration: The effect of carbonate dissolution on reservoir rock integrity [Master of Earth Sciences and Petroleum Engineering: Norwegian University of Science and Technology, 108 p.

Han, D.-h., and Batzle, M. L., 2004, Gassmann's equation and fluid-saturation effects on seismic velocities: GEOPHYSICS, v. 69, no. 2, p. 8.

Han, D.-h., and Sun, M., 2012, Velocity and density of CO2 -oil miscible mixtures, SEG Annual Meeting: Las Veegas, SEG.

Mavko, G., Mukerji, T., and Dvorkin, J., 2009, The Rock Physics Handbook, Cambridge, United Kingdom, Cambridge University Press.

Smith, T. M., Sondergeld, C. H., and Rai, C. S., 2003, Gassmann fluid substitutions: A tutorial: GEOPHYSICS, v. 68, no. 2, p. 430-440.

SPE, 2016, Gassmann's equation for fluid substitution, PetroWiki, Volume 2016.

FIGURES

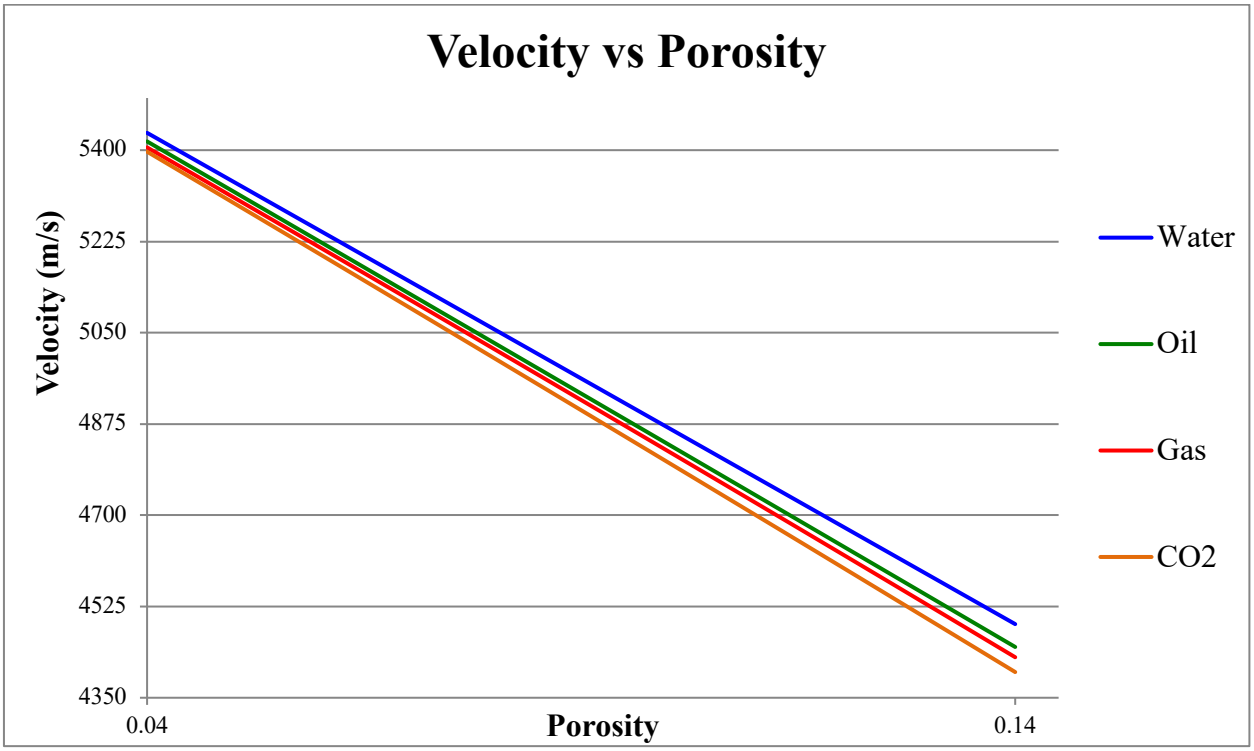

Figure A-1– Sandstone model velocity vs. porosity for several fluids: Water, Oil, Gas, and CO_2.

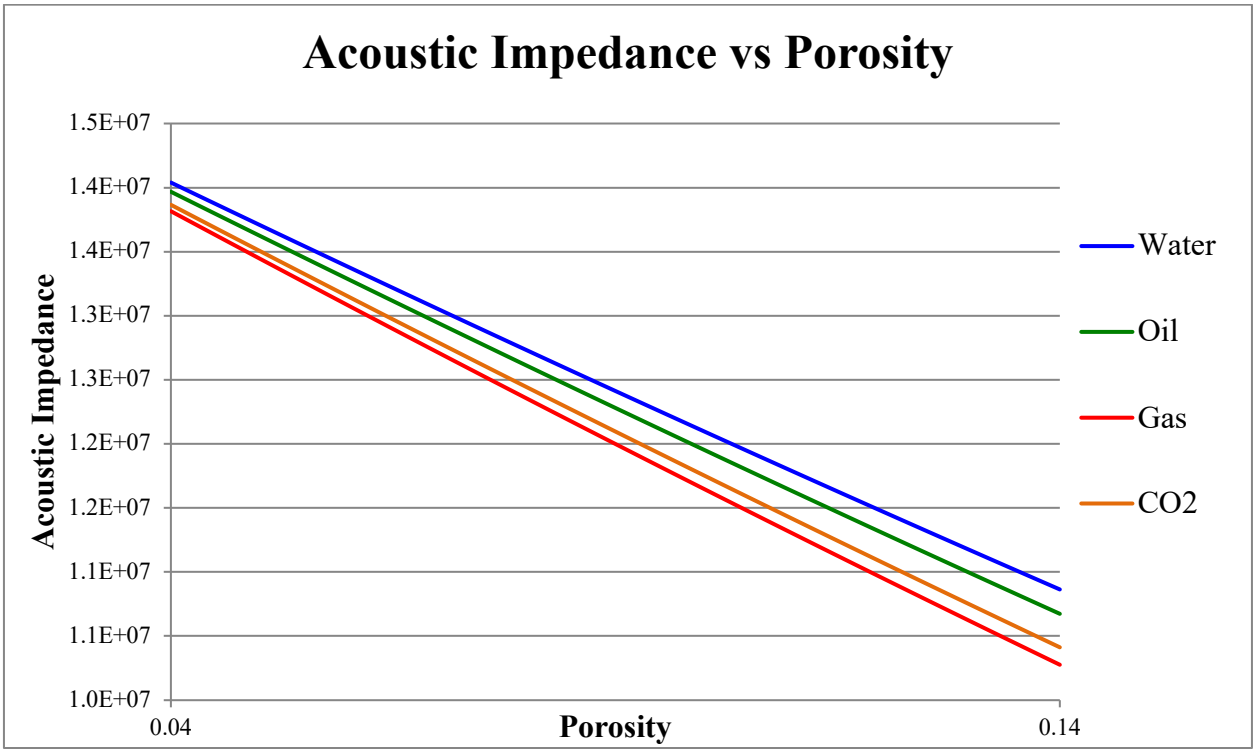

Figure A-2 – Sandstone model acoustic impedance vs. porosity for several fluids: Water, Oil, Gas, and CO_2.

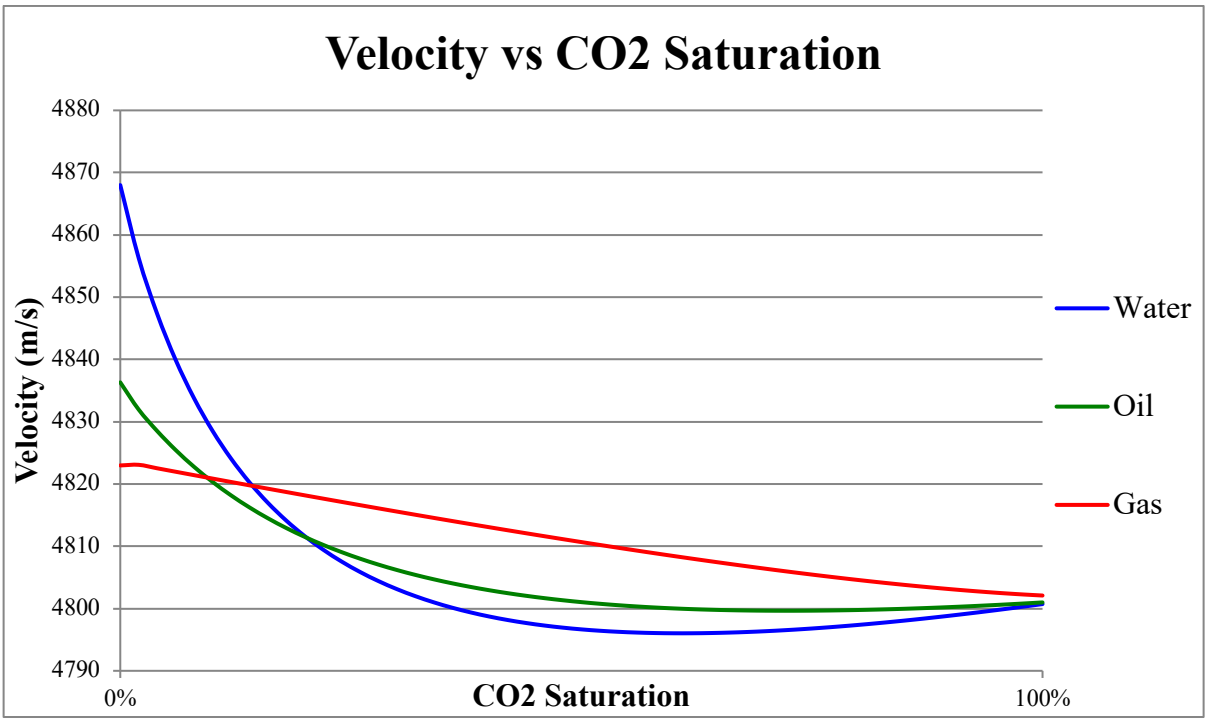

Figure A-3– Sandstone model velocity vs. CO_2 saturation for several initial fluid saturations (Water, Oil, Gas) at constant, 10%, porosity.

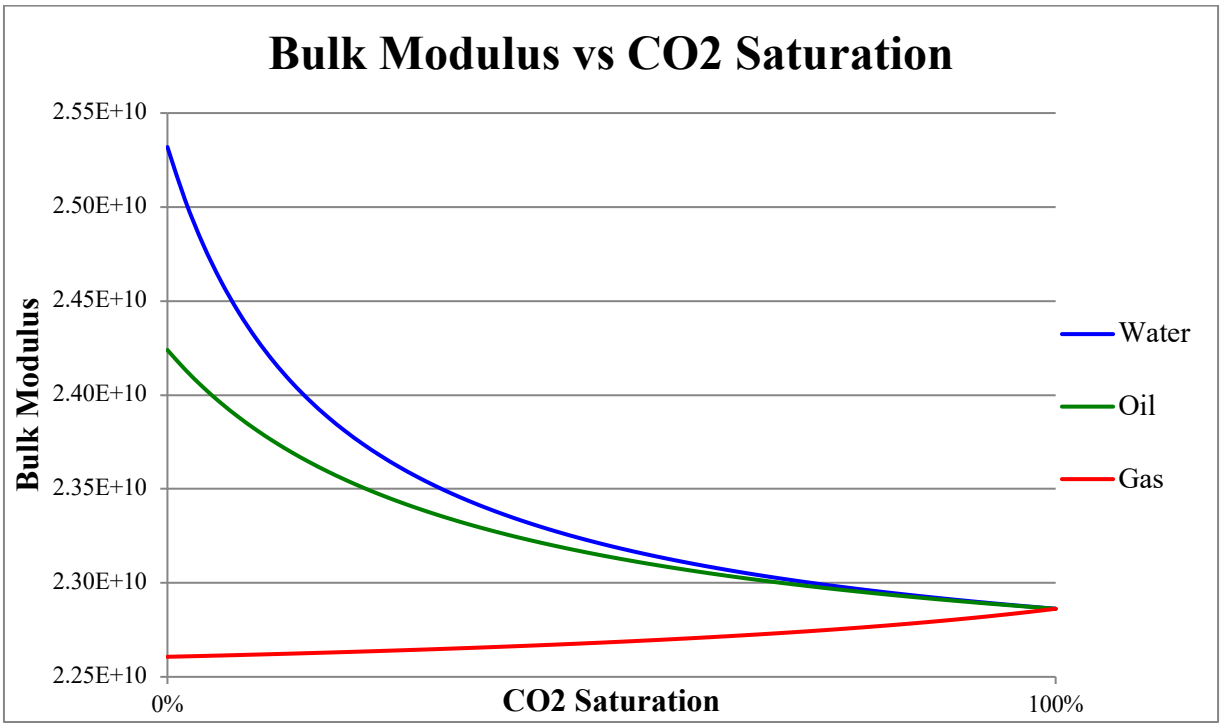

Figure A-4– Sandstone model bulk modulus vs. CO_2 saturation for several initial fluid saturations (Water, Oil, Gas) at constant, 10%, porosity.

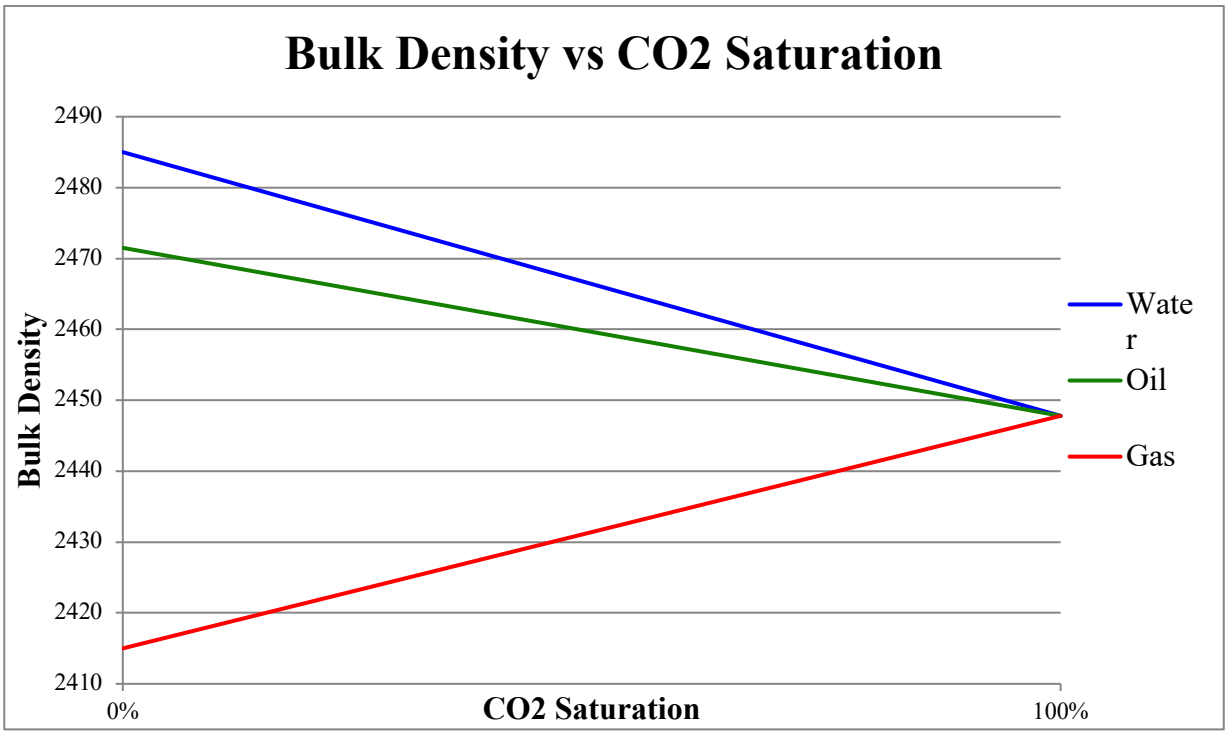

Figure A-5 – Sandstone model bulk density vs. CO_2 saturation for several initial fluid saturations (Water, Oil, Gas) at constant, 10%, porosity.

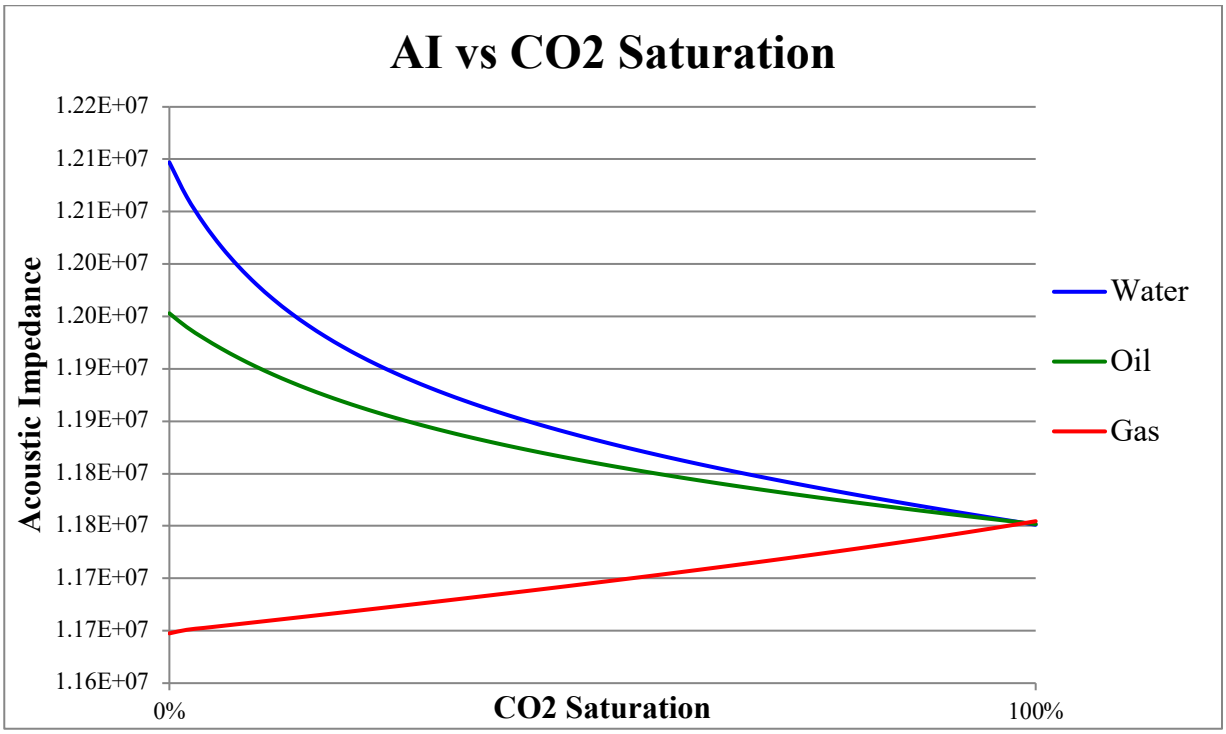

Figure A-6 - Sandstone model acoustic impedance vs. CO_2 saturation for several initial fluid saturations (Water, Oil, Gas) at constant, 10%, porosity.

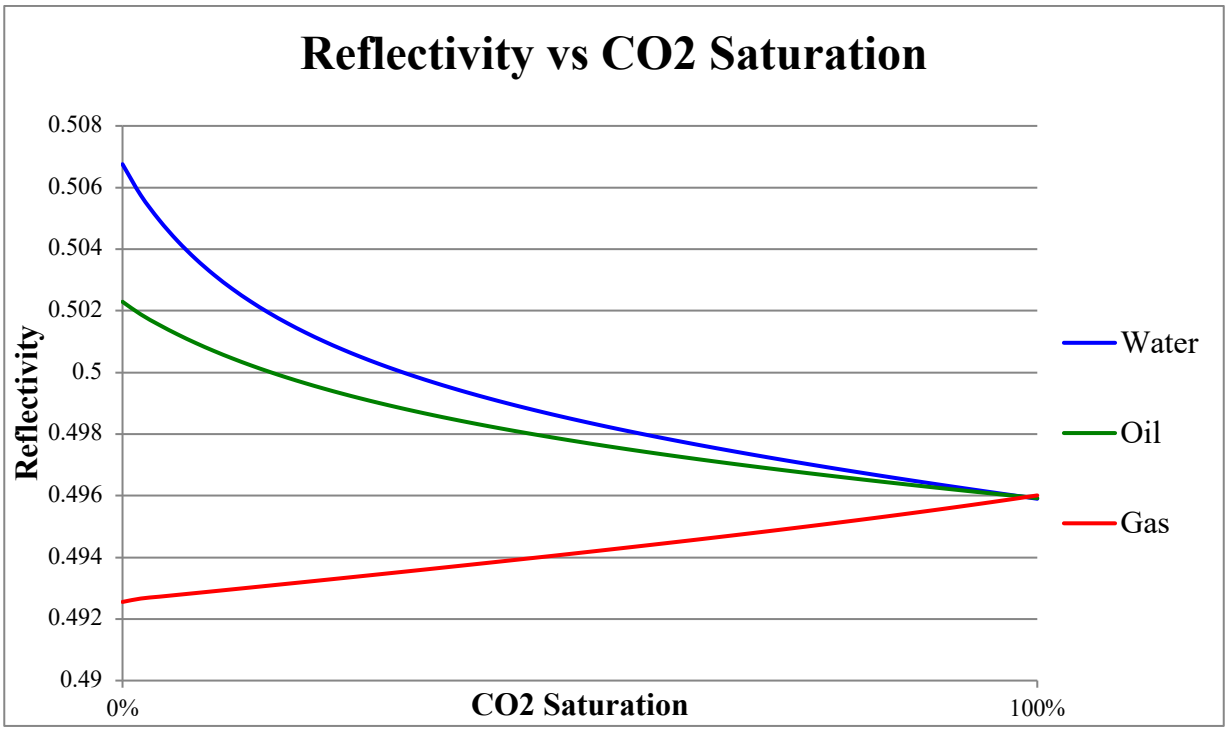

Figure A-7 - Sandstone model reflectivity vs. CO_2 saturation for several initial fluid saturations (Water, Oil, Gas) at constant, 10%, porosity. Overlying formation follows the parameters of the Shale Model.

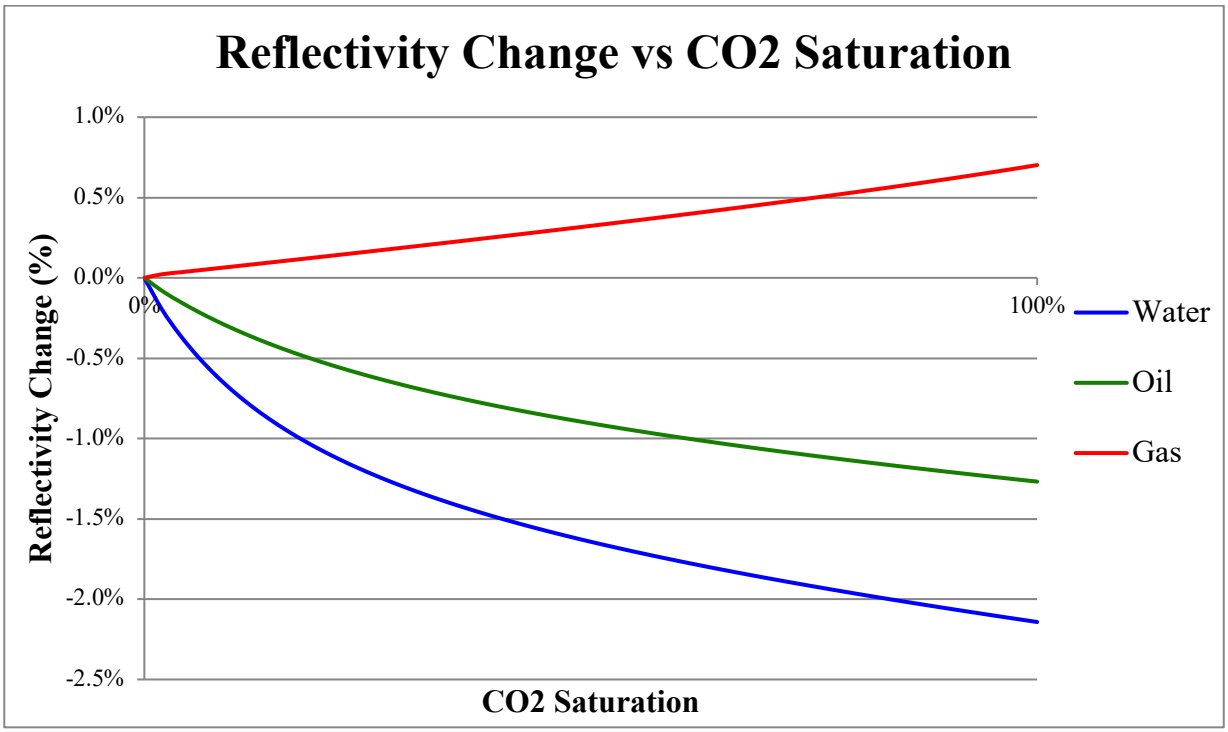

Figure A-8 - Sandstone model reflectivity change (%) vs. CO_2 saturation for several initial fluid saturations (Water, Oil, Gas) at constant, 10%, porosity. Overlying formation follows the parameters of the Shale Model.

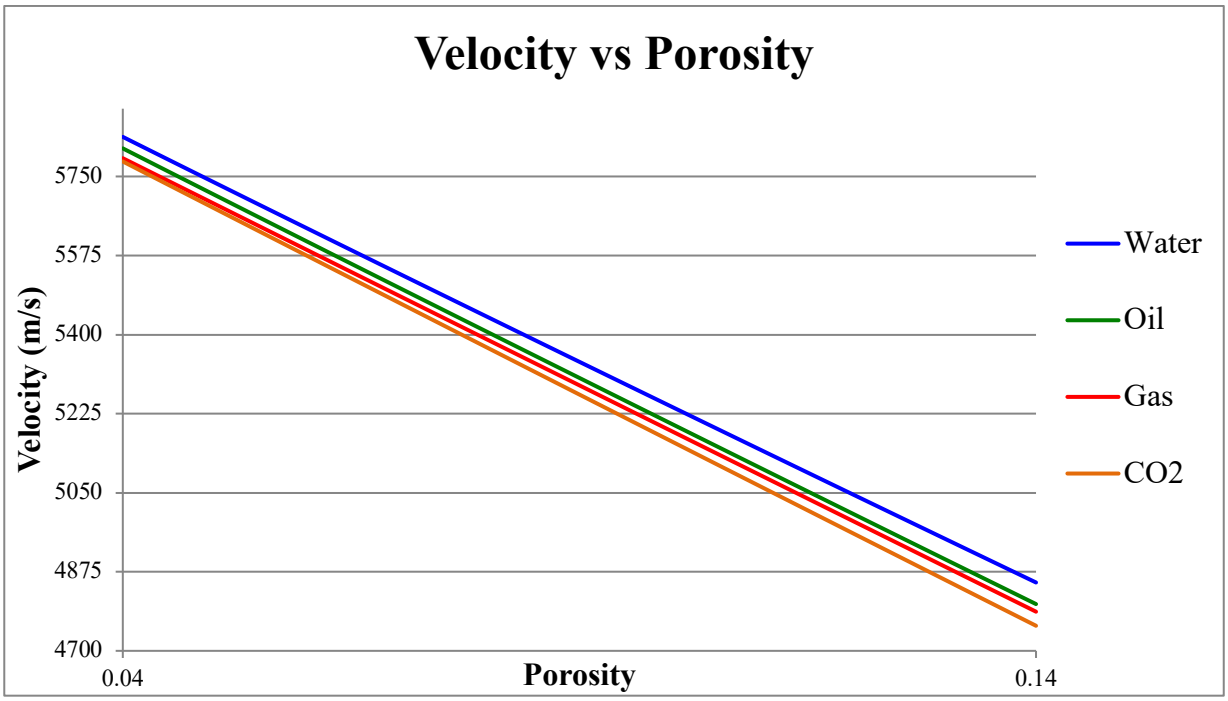

Figure A-9 – Limestone model velocity vs. porosity for several fluids: Water, Oil, Gas, and CO_2.

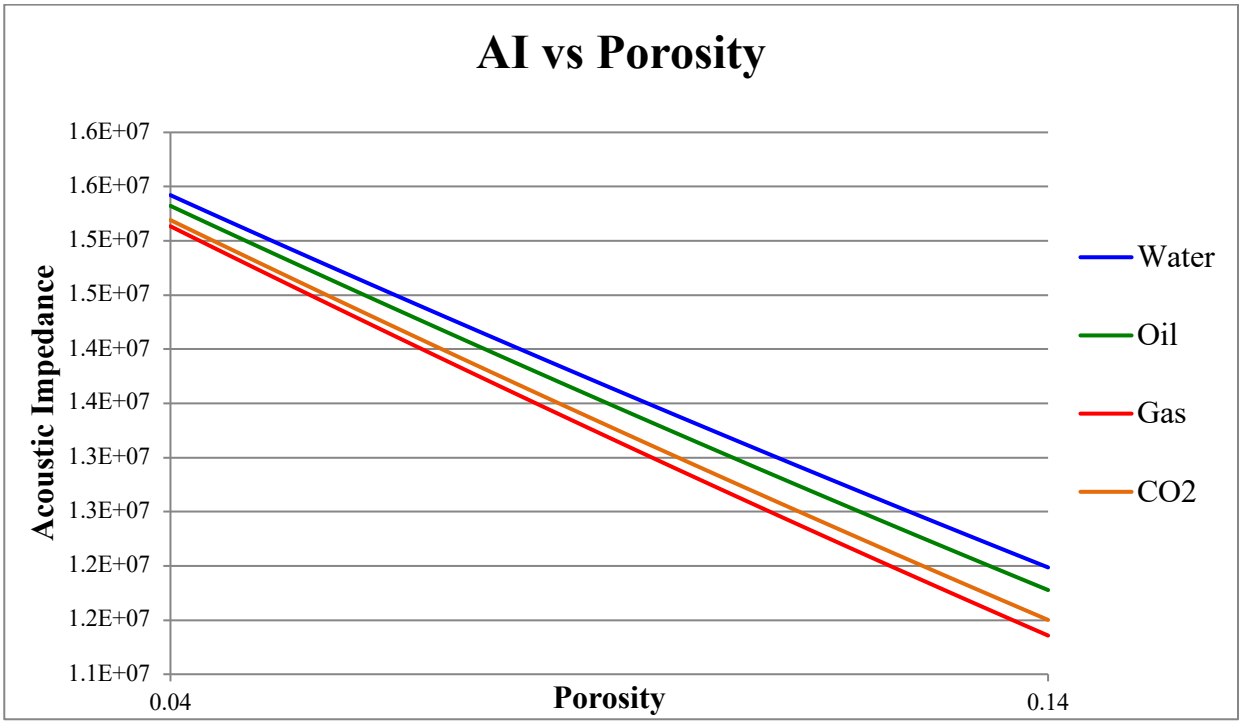

Figure A-10 - Limestone model acoustic impedance vs. porosity for several fluids: Water, Oil, Gas, and CO_2.

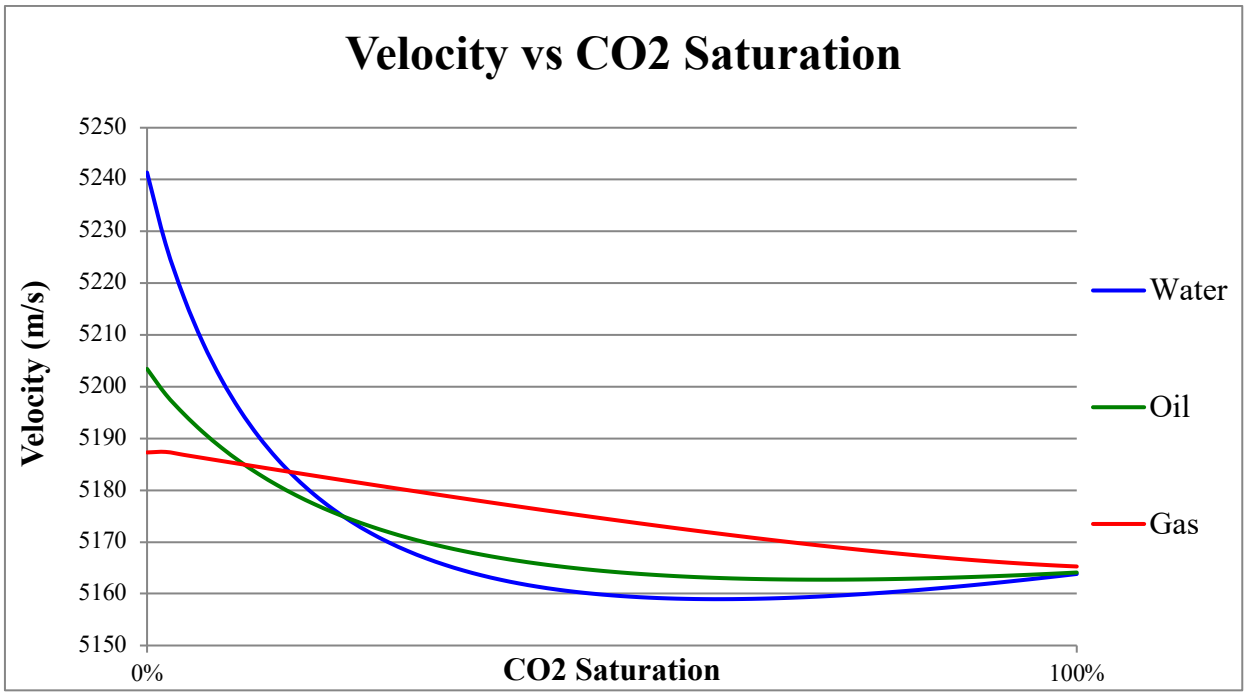

Figure A-11 – Limestone model velocity vs. CO_2 saturation for several initial fluid saturations (Water, Oil, Gas) at constant, 10%, porosity.

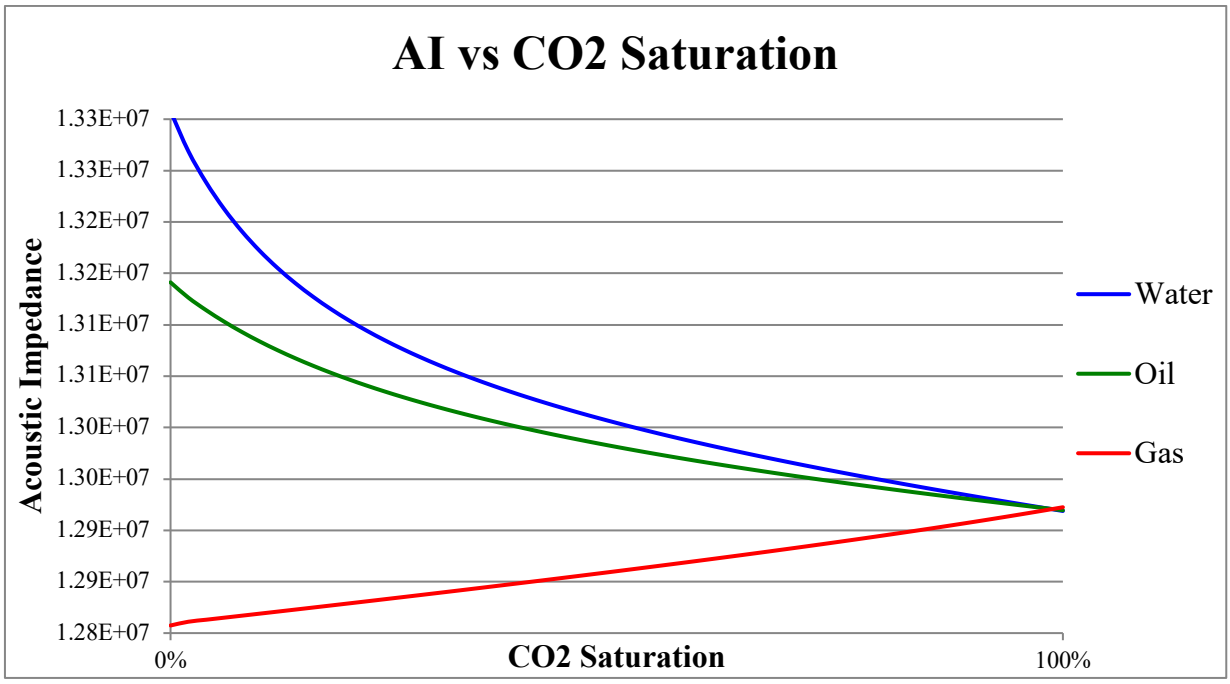

Figure A-12 – Limestone model velocity vs. CO_2 saturation for several initial fluid saturations (Water, Oil, Gas) at constant, 10%, porosity.

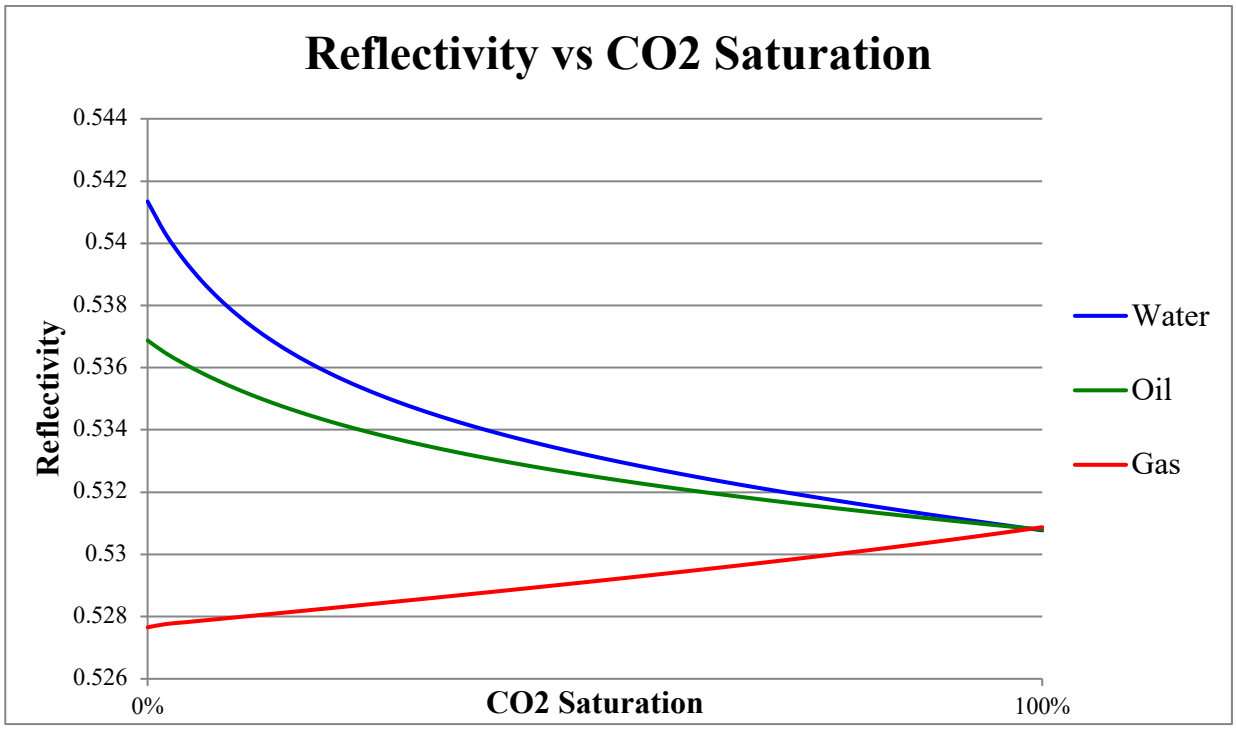

Figure A-13 – Limestone model reflectivity vs. CO_2 saturation for several initial fluid saturations (Water, Oil, Gas) at constant, 10%, porosity. Overlying formation follows the parameters of the Shale Model.

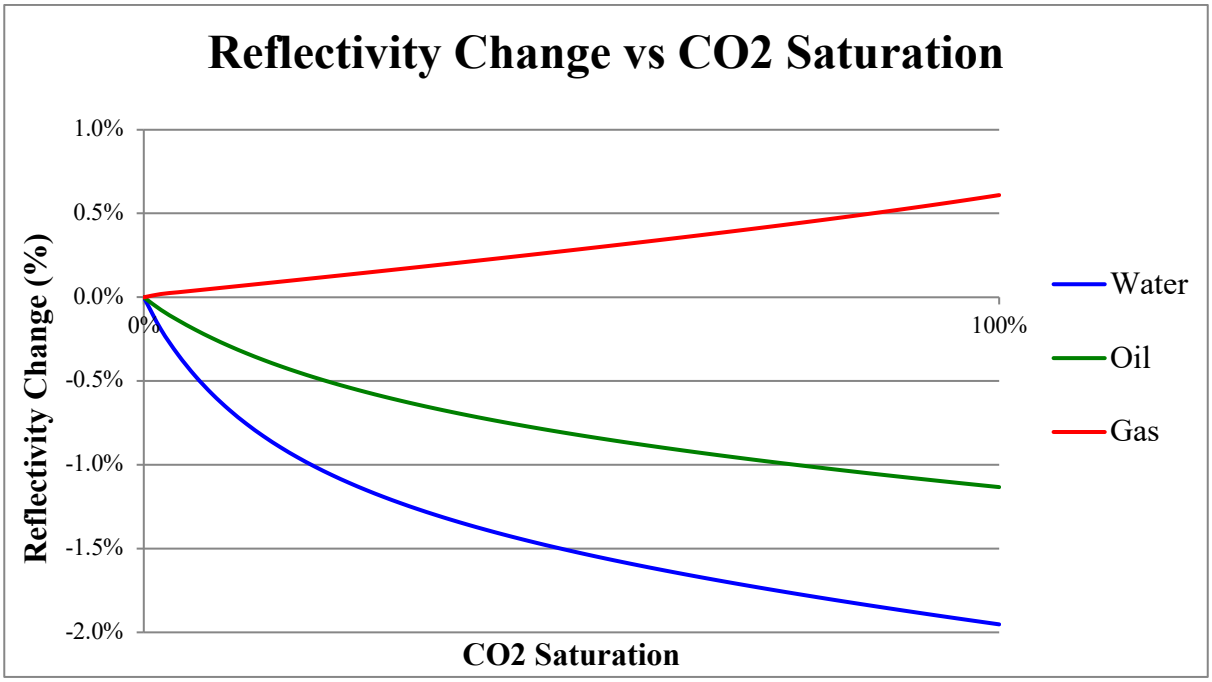

Figure A-14 - Limestone model reflectivity change (%) vs. CO_2 saturation for several initial fluid saturations (Water, Oil, Gas) at constant, 10%, porosity. Overlying formation follows the parameters of the Shale Model.

APPENDIX B – PSTM FORWARD MODELLING

These forward modelling PSTM tests were conducted to support Section 3.2.1. The MATLAB code below along with the CREWES package created the images in Section 3.2.1 and the images in this appendix.

```
%%%%%%%%%%%%%%%%%%%%%%%%%%%%%%%%%%
%%%%%%       PSTM Tests       %%%%%%
%%%%%%%%%%%%%%%%%%%%%%%%%%%%%%%%%%

%Ricker, event_dip, plotimage, kirk_mig, and sectconv from CREWES MATLAB
%PACKAGE

%define sampling and dependent variables
dt=.001;dx=5;tmax=2;xmax=4000;v1=1500;v2=3000;
%input wavelet
[w,tw]=Ricker(dt,40);
x=0:dx:xmax;
t=0:dt:tmax;
nx = length(x);
nt = length(t);
amat=zeros(nt,nx);
%create hole endpoints
x1=1990:-20:1910;
x2=2010:20:2090;
%Create velocity model
vmodel=v1:(v2-v1)/(tmax/dt):v2;
vmodel=vmodel.';
vmodel2=vmodel.*ones(size(amat));
tarray = t.'.*ones(size(amat));
t1=1.4;
%hole sizes
holesz=abs(x1-x2);
% Event
for i = x1
    for j = x2
        if (i==x1)==(j==x2)
            %Create event
            amat=event_dip(amat,t,x,[t1 t1],[0 i],1);
            amat=event_dip(amat,t,x,[t1 t1],[j 10000],1);
            %convolve wavelet with event
            amat=sectconv(amat,t,w,tw);

            %plot before migration
            plotimage(amat,t,x);
            titlestring = ['Hole Width: ',num2str(holesz(x1==i)),' Before
Migration'];
            title(titlestring)
            xlim([1500 2500]);
            ylim([1 1.6])

            %Migrate
```

```
            [arymig,tmig,xmig]=kirk_mig(amat,vmodel2,dt,dx,nan);
            %Plot aftermigration
            plotimage(arymig,t,x)
            titlestring = ['Hole Width: ',num2str(holesz(x1==i)),' After
Migration'];
            title(titlestring)
            xlim([1500 2500]);
            ylim([1 1.6])

            %Store information for plotting amplitude and timeshift
            migampmax(x1==i,:) = max(arymig);
            teventmig(x1==i,:) = tarray(arymig==(migampmax(x1==i,:)));
            amat = zeros(nt,nx);
        end
    end
end

%Calc time shift
tshift = abs(1.397-teventmig);
%Plot amge change
figure;
plot(x,100*((migampmax-8.211161179156775e-04)/8.211161179156775e-04))
xlim([1500 2500]);
title('Amplitude Change vs Hole Size')
xlabel('Distance (m)')
ylabel('Amplitude Change (%)')
lgd1=legend(string(holesz),'location','southeast');
title(lgd1,'Hole Size (m)')
prepfig

%Plot time Shift
figure;
plot(x,tshift*1000)
xlim([1500 2500]);
title('Time shift vs Hole Size');
xlabel('Distance (m)');
ylabel('Time Shift (mS)');
lgd2=legend(string(holesz),'location','northeast');
title(lgd2,'Hole Size (m)');
prepfig
```

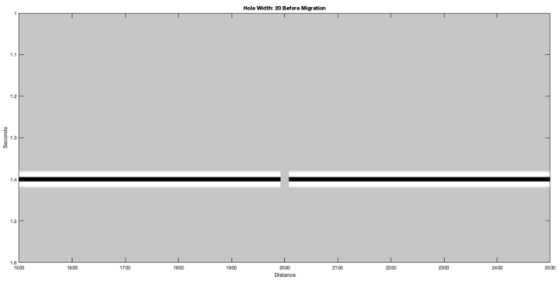

Figure B.1 20m hole before migration.

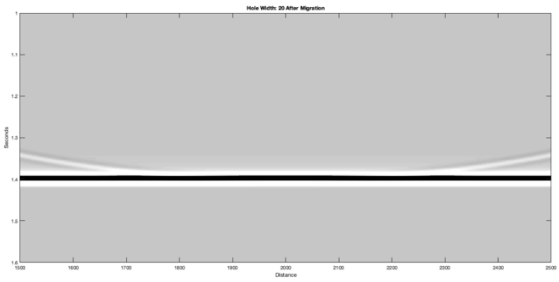

Figure B.2 20m hole after migration.

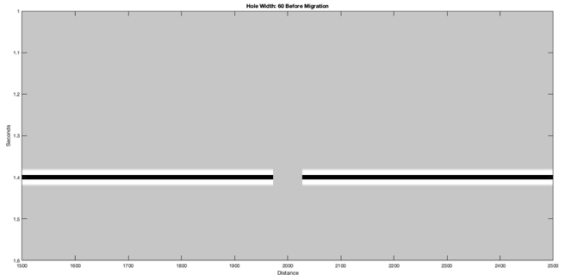

Figure B.3 60m hole before migration.

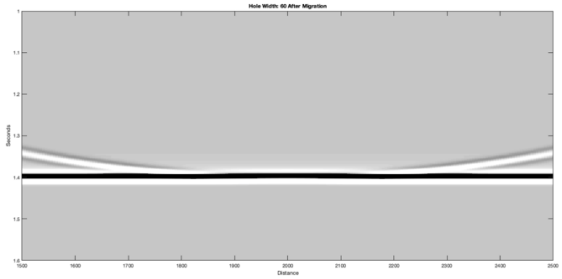

Figure B.4 60m hole after migration.

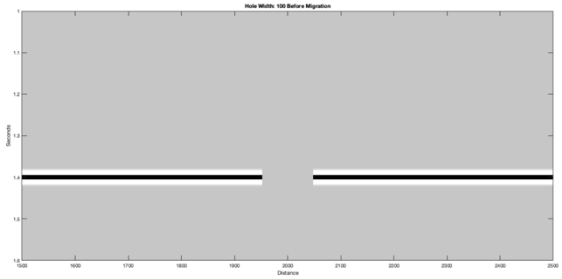

Figure B.5 100m hole before migration.

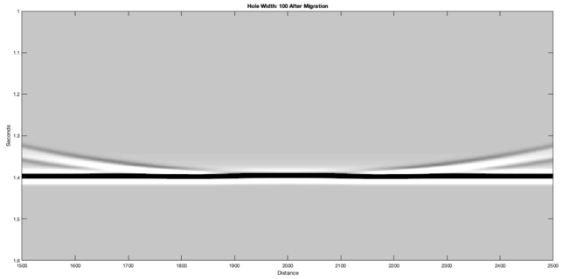

Figure B.6 100m hole after migration.

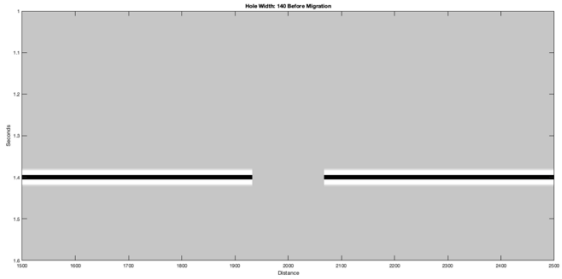

Figure B.7 140m hole before migration.

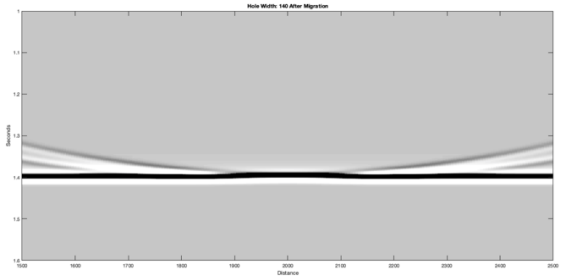

Figure B.8 140m hole after migration.

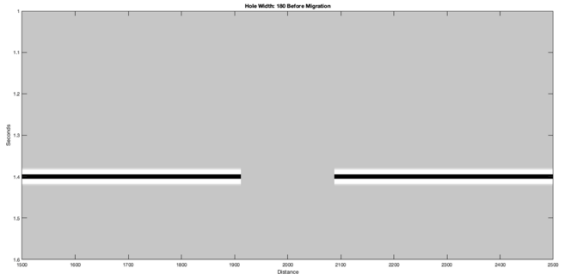

Figure B.9 180m hole before migration.

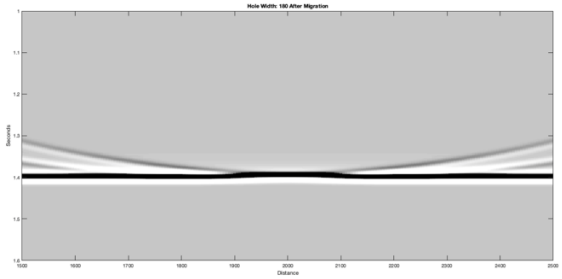

Figure B.10 180m hole after migration.

APPENDIX C – FRESNEL ZONE INFILL EVALUATION

Fresnel zone infill evaluation is carried out through a simple procedure with some slight variations between seismic contractors. The steps for a simple infill evaluation are shown below on the Hd2D dataset.

1. Identify target reflectors in area of interest.
2. Determine a mute function and assign each offset group a target horizon of interest (deeper targets with larger offsets).

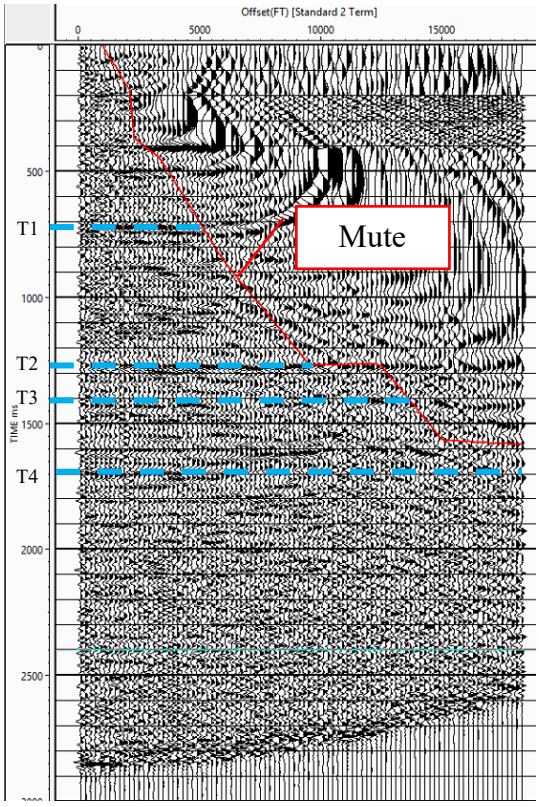

Figure C.1 NMO corrected CMP with target horizons T1-T4, and mute annotated.

3. Measure or predict frequency content and rms velocity at target horizons of interest.
    a. Frequency content is estimated by a set decrease from the frequency with the highest power on the frequency spectrum. This is usually 10 to 20 dB below the maximum. See Figure C.2. As an alternative, filter panels can be used or other visual estimations.

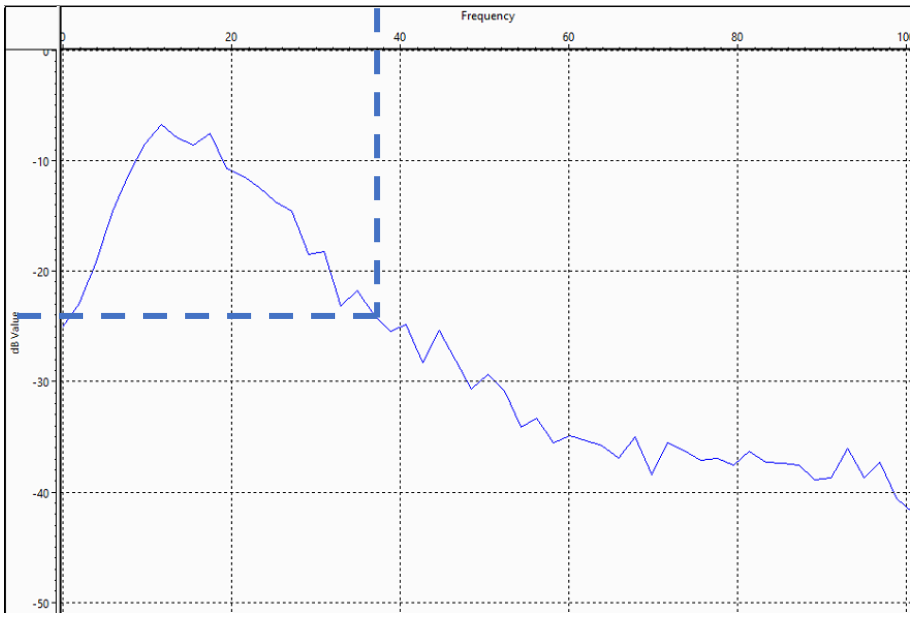

Figure C.2 Frequency spectrum for target T1.

4. Use frequency, two-way time, rms velocity and offset to calculate Fresnel zone size perpendicular to source-receiver axis.

$$\perp \text{ to shot} - \text{receiver axis}: Y_F = \frac{V}{2}\sqrt{t_f^2 - t_0^2 - \frac{4h^2}{V^2}}$$

Where,

$$t_f = t_x + \frac{\tau}{2};\ \ t_x = \frac{2}{v_{rms}}\sqrt{\left(\frac{h}{2}\right)^2 + \left(\frac{t * v}{2}\right)^2};$$

Target	Time (ms)	RMS Vel. (ft/s)	Frequency (Hz)	Mute Offset (ft)	FZ Size
T1	723	10697	38	5250	814
T2	1274	13735	34	9600	1423
T3	1430	14132	25	14000	1869
T4	1607	14535	20	18000	2321

5. Assign a cutoff percentage of the Fresnel zone size as the acceptability for the number of empty bins.
    a. This step accounts for errors in the calculations or estimation of variables that may have led to erroneously large Fresnel zones.

Target	FZ Size	75% of FZ
T1	814	610
T2	1423	1067
T3	1869	1401
T4	2321	1704

APPENDIX D– FRESNEL ZONE MODELS

The function below (OFZ) outputs the Fresnel zone ellipsoid for a given frequency (f), rms velocity (Vrms), source-receiver half distance (h), crossline source-receiver offset (w), and zero offset two-way travel time. The outputs ellout and pout store the Fresnel ellipsoid and plane layer used to calculate it. The outputs WestCross, EastCross, NorthIn, and SouthIn store the intersection points between the plane and the Fresnel ellipsoid in the crossline and inline directions with cardinal north pointing in the direction of the array away from the source. To calculate the crossline Fresnel zone diameter, take the mean of the absolute values of WestCross and Eastcross. Similarly, to calculate the inline Fresnel zone diameter, take the mean of the absolute values of NorthIn and SouthIn.

To enable the plotting of the Fresnel zone ellipsoids and associated planes change the ZeroOffsetTop, ZeroOffsetAngle, FullTop, and FullAngle variables to 'y'. The plot display variables with 'ZeroOffset' will plot the zero offset Fresnel ellipsoid (sphere), and the varaiables with 'Full' will plot the offset Fresnel zone ellipsoid with additional lateral offset component. The plot display variables with 'Top' will display a top view and the variables with 'Angle' will display from an angle ([-1 -1 1]).

```
function [ellout,pout,WestCross,EastCross,NorthIn,SouthIn]=OFZ(f,Vrms,h,w,t0)
%OFZ(f,Vrms,h,w,t0,dipindegrees,azimuthindegrees) future version to
%account for dipping reflector.
%plots? 'y' or 'n'
ZeroOffsetTop = 'n';
ZeroOffsetAngle = 'n';
FullTop = 'n';
FullAngle = 'n';
 %Variables
 w=-w; %fix w
 tx=sqrt(t0^2+(2*h)^2/(Vrms^2)); %Offset traveltime equation
 y0=-h/2;x0=0;t=-pi+.01:pi;
 tx2=t0;
 dip=90*pi/180; %dip=(90-dipindegrees)*pi/180 <- applies dipping reflector.
Equations not suitable for dip currently.
 azimuth=0; %azimuth=azimuthindegrees*pi/180 <- strike of dipping reflector.
Equations not suitable for dip currently.
```

```
 l=Vrms*(tx+1/(2*f))/2;
 l2=Vrms*(tx2+1/(2*f))/2;
 zp=Vrms*t0/2;
 point = [0,0,-zp];
%%%%%% Create Ellipsoid and Plane w/ Dip and Offset %%%%%%
%normalize = sqrt(cos(dip)*sin(azimuth)+cos(dip)*cos(azimuth)+sin(dip));
normalvector = [0 0 1];
%normalvector=[cos(dip)*sin(azimuth)/normalize,cos(dip)*cos(azimuth)/normaliz
e,cos(dip)/normalize];
d=-
(normalvector(1)*point(1)+normalvector(2)*point(2)+normalvector(3)*point(3));
[x,y,z]=ellipsoid(0,0,0,sqrt(l^2-h^2),l,sqrt(l^2-h^2),100);
ellout=[x,y,z];
[X,Y]=meshgrid(-l*1.1:l*1.1/100:l*1.1);
Z=(-normalvector(1)*X-normalvector(2)*Y-d)/normalvector(3);
pout=[X,Y,Z];
%%%%% Create Ellipsoid and Plane w/OUT Dip and Offset %%%%
normalvector2=[0 0 1];
d2=-
(normalvector2(1)*point(1)+normalvector2(2)*point(2)+normalvector2(3)*point(3
));
[x2,y2,z2]=ellipsoid(0,0,0,l2,l2,l2,100);
[X2,Y2]=meshgrid(-l*1.1:l*1.1/100:l*1.1);
Z2=-zp.*ones(size(X2));
%%%%%% 3D Plot Ellipsoid and Plane w/ Dip and Offset %%%%%
if FullTop == 'y' || FullAngle == 'y'
    figure1=figure;

plansesurf=surf(X,Y,Z,'LineWidth',.1,'EdgeAlpha','.1','FaceColor','r','FaceAl
pha','.75');
    hold on

ellipsoidshape=surf(x,y,z,'LineStyle','none','FaceAlpha','.5','FaceColor','b'
);
    direction = [0 0 1];
    if w ~=0
        rotate(ellipsoidshape,direction,5);
    end
    axis equal
    hold on
    plot3(point(1),point(2),point(3),'.','MarkerSize',25,'Color','k');
    plot3(-w,-h,0,'*','MarkerSize',10,'Color','w');
    plot3(w,h,0,'o','MarkerSize',10,'Color','w');
    xlabel('x (m)');ylabel('y (m)');zlabel('z (m)');
    title('Offset Fresnel Ellipsoid')
    a1=gca;
    if FullTop == 'y'
        view([0 0 1]);
    elseif FullAngle == 'y'
        view([-1 -1 1]);
    end
    if FullTop == 'y' && FullAngle == 'y'
        figure1b=figure;
        copyobj(a1,figure1b);
        view([-1 -1 1]);
    end
end
```

```
%%%% 3D Plot Ellipsoid and Plane w/OUT Dip and Offset %%%%
if ZeroOffsetTop == 'y' || ZeroOffsetAngle == 'y'
    figure2=figure;

plansesurf2=surf(X2,Y2,Z2,'LineWidth',.1,'EdgeAlpha',.1,'FaceColor','r','Face
Alpha','.75');
    hold on

ellipsoidshape2=surf(x2,y2,z2,'LineStyle','none','FaceAlpha','.5','FaceColor'
,'b');
    axis equal
    hold on
    plot3(point(1),point(2),point(3),'.','MarkerSize',25,'Color','k');
    plot3(-w,-h,0,'*','MarkerSize',10,'Color','k');
    plot3(w,h,0,'o','MarkerSize',10,'Color','k');
    xlabel('x (m)');ylabel('y (m)');zlabel('z (m)');
    title('Zero Offset Fresnel Ellipsoid')
    a2=gca;
    if ZeroOffsetTop == 'y'
        view([0 0 1]);
    elseif ZeroOffsetAngle == 'y'
        view([-1 -1 1]);
    end
    if ZeroOffsetTop == 'y' && ZeroOffsetAngle == 'y'
        figure2b=figure;
        copyobj(a2,figure2b);
        view([-1 -1 1]);
    end
end
%%%%%%% Calculate Inline and Crossline Components %%%%%%%%
yi=0;li=l;hi=h;di=d;ai=normalvector(1);bi=normalvector(2);ci=normalvector(3);
xi=0;wi=w;
if h==0
    offsetangle=0;
else
    offsetangle=atan(w/h);
end
WestCross = -(ci*li*(ai^2*li^4+ci^2*li^4*cos(offsetangle)^2-
      di^2*li^2*cos(offsetangle)^2+ci^2*hi^4*sin(offsetangle)^2+di^2*hi^2*sin
      (offsetangle)^2+ci^2*li^4*sin(offsetangle)^2-
      di^2*li^2*sin(offsetangle)^2-
      ai^2*hi^2*li^2+bi^2*hi^2*yi^2*sin(offsetangle)^2+ci^2*hi^2*yi^2*sin(off
      setangle)^4-ai^2*li^2*yi^2*sin(offsetangle)^2-
      bi^2*li^2*yi^2*sin(offsetangle)^2-ci^2*li^2*yi^2*sin(offsetangle)^4-
      ci^2*hi^2*li^2*cos(offsetangle)^2+ai^2*hi^2*yi^2*cos(offsetangle)^2+ci^
      2*hi^2*yi^2*cos(offsetangle)^4-ai^2*li^2*yi^2*cos(offsetangle)^2-
      2*ci^2*hi^2*li^2*sin(offsetangle)^2-bi^2*li^2*yi^2*cos(offsetangle)^2-
      ci^2*li^2*yi^2*cos(offsetangle)^4+2*ci^2*hi^2*yi^2*cos(offsetangle)^2*s
      in(offsetangle)^2-
      2*ci^2*li^2*yi^2*cos(offsetangle)^2*sin(offsetangle)^2-
      2*bi*di*li^2*yi*cos(offsetangle)^2+2*bi*di*hi^2*yi*sin(offsetangle)^2-
      2*bi*di*li^2*yi*sin(offsetangle)^2+2*ai*di*hi^2*yi*cos(offsetangle)*sin
      (offsetangle)+2*ai*bi*hi^2*yi^2*cos(offsetangle)*sin(offsetangle))^(1/2
      )+ai*di*li^2+ai*bi*li^2*yi+ci^2*hi^2*yi*cos(offsetangle)*sin(offsetangl
      e))/(ai^2*li^2-
      ci^2*hi^2*sin(offsetangle)^2+ci^2*li^2*cos(offsetangle)^2+ci^2*li^2*sin
      (offsetangle)^2);
```

```
EastCross = -(ai*di*li^2 - ci*li*(ai^2*li^4 + ci^2*li^4*cos(offsetangle)^2-
      di^2*li^2*cos(offsetangle)^2+ci^2*hi^4*sin(offsetangle)^2+di^2*hi^2*sin
      (offsetangle)^2+ci^2*li^4*sin(offsetangle)^2-
      di^2*li^2*sin(offsetangle)^2-
      ai^2*hi^2*li^2+bi^2*hi^2*yi^2*sin(offsetangle)^2+ci^2*hi^2*yi^2*sin(off
      setangle)^4-ai^2*li^2*yi^2*sin(offsetangle)^2-
      bi^2*li^2*yi^2*sin(offsetangle)^2-ci^2*li^2*yi^2*sin(offsetangle)^4-
      ci^2*hi^2*li^2*cos(offsetangle)^2+ai^2*hi^2*yi^2*cos(offsetangle)^2+ci^
      2*hi^2*yi^2*cos(offsetangle)^4-ai^2*li^2*yi^2*cos(offsetangle)^2-
      2*ci^2*hi^2*li^2*sin(offsetangle)^2-bi^2*li^2*yi^2*cos(offsetangle)^2-
      ci^2*li^2*yi^2*cos(offsetangle)^4+2*ci^2*hi^2*yi^2*cos(offsetangle)^2*s
      in(offsetangle)^2-
      2*ci^2*li^2*yi^2*cos(offsetangle)^2*sin(offsetangle)^2-
      2*bi*di*li^2*yi*cos(offsetangle)^2+2*bi*di*hi^2*yi*sin(offsetangle)^2-
      2*bi*di*li^2*yi*sin(offsetangle)^2+2*ai*di*hi^2*yi*cos(offsetangle)*sin
      (offsetangle)+2*ai*bi*hi^2*yi^2*cos(offsetangle)*sin(offsetangle))^(1/2
      )+ai*bi*li^2*yi+ci^2*hi^2*yi*cos(offsetangle)*sin(offsetangle))/(ai^2*l
      i^2-
      ci^2*hi^2*sin(offsetangle)^2+ci^2*li^2*cos(offsetangle)^2+ci^2*li^2*sin
      (offsetangle)^2);

SouthIn = -
      (ci*li*(bi^2*li^4+ci^2*hi^4*cos(offsetangle)^2+di^2*hi^2*cos(offsetangl
      e)^2+ci^2*li^4*cos(offsetangle)^2-
      di^2*li^2*cos(offsetangle)^2+ci^2*li^4*sin(offsetangle)^2-
      di^2*li^2*sin(offsetangle)^2-
      bi^2*hi^2*li^2+bi^2*hi^2*xi^2*sin(offsetangle)^2+ci^2*hi^2*xi^2*sin(off
      setangle)^4-ai^2*li^2*xi^2*sin(offsetangle)^2-
      bi^2*li^2*xi^2*sin(offsetangle)^2-ci^2*li^2*xi^2*sin(offsetangle)^4-
      2*ci^2*hi^2*li^2*cos(offsetangle)^2+ai^2*hi^2*xi^2*cos(offsetangle)^2+c
      i^2*hi^2*xi^2*cos(offsetangle)^4-ai^2*li^2*xi^2*cos(offsetangle)^2-
      bi^2*li^2*xi^2*cos(offsetangle)^2-ci^2*hi^2*li^2*sin(offsetangle)^2-
      ci^2*li^2*xi^2*cos(offsetangle)^4+2*ci^2*hi^2*xi^2*cos(offsetangle)^2*s
      in(offsetangle)^2-
      2*ci^2*li^2*xi^2*cos(offsetangle)^2*sin(offsetangle)^2+2*ai*di*hi^2*xi*
      cos(offsetangle)^2-2*ai*di*li^2*xi*cos(offsetangle)^2-
      2*ai*di*li^2*xi*sin(offsetangle)^2+2*bi*di*hi^2*xi*cos(offsetangle)*sin
      (offsetangle)+2*ai*bi*hi^2*xi^2*cos(offsetangle)*sin(offsetangle))^(1/2
      )+bi*di*li^2+ai*bi*li^2*xi+ci^2*hi^2*xi*cos(offsetangle)*sin(offsetangl
      e))/(bi^2*li^2-
      ci^2*hi^2*cos(offsetangle)^2+ci^2*li^2*cos(offsetangle)^2+ci^2*li^2*sin
      (offsetangle)^2);

NorthIn = -(bi*di*li^2-
      ci*li*(bi^2*li^4+ci^2*hi^4*cos(offsetangle)^2+di^2*hi^2*cos(offsetangle
      )^2+ci^2*li^4*cos(offsetangle)^2-
      di^2*li^2*cos(offsetangle)^2+ci^2*li^4*sin(offsetangle)^2-
      di^2*li^2*sin(offsetangle)^2-
      bi^2*hi^2*li^2+bi^2*hi^2*xi^2*sin(offsetangle)^2+ci^2*hi^2*xi^2*sin(off
      setangle)^4-ai^2*li^2*xi^2*sin(offsetangle)^2-
      bi^2*li^2*xi^2*sin(offsetangle)^2-ci^2*li^2*xi^2*sin(offsetangle)^4-
      2*ci^2*hi^2*li^2*cos(offsetangle)^2+ai^2*hi^2*xi^2*cos(offsetangle)^2
+ci^2*hi^2*xi^2*cos(offsetangle)^4-ai^2*li^2*xi^2*cos(offsetangle)^2-
      bi^2*li^2*xi^2*cos(offsetangle)^2-ci^2*hi^2*li^2*sin(offsetangle)^2-
      ci^2*li^2*xi^2*cos(offsetangle)^4+2*ci^2*hi^2*xi^2*cos(offsetangle)^2*s
      in(offsetangle)^2-
```

```
      2*ci^2*li^2*xi^2*cos(offsetangle)^2*sin(offsetangle)^2+2*ai*di*hi^2*xi*
      cos(offsetangle)^2-2*ai*di*li^2*xi*cos(offsetangle)^2-
      2*ai*di*li^2*xi*sin(offsetangle)^2+2*bi*di*hi^2*xi*cos(offsetangle)*sin
      (offsetangle)+2*ai*bi*hi^2*xi^2*cos(offsetangle)*sin(offsetangle))^(1/2
      )+ai*bi*li^2*xi+ci^2*hi^2*xi*cos(offsetangle)*sin(offsetangle))/(bi^2*l
      i^2-
      ci^2*hi^2*cos(offsetangle)^2+ci^2*li^2*cos(offsetangle)^2+ci^2*li^2*sin
      (offsetangle)^2);
end

% Used to find inline and crossline equations (above)
% % syms xi yi zi li hi wi ci di ai bi offsetangle
% % ells=solve((xi*cos(offsetangle)+yi*sin(offsetangle)) ...
% % ... ^2/(li^2-hi^2)+(yi*cos(offsetangle)-xi*sin(offsetangle)) ...
% % ... ^2/li^2+zi^2/(li^2-hi^2)==1,zi);
% % planez=solve(ai*xi+bi*yi+ci*zi==-di,zi);
% % solx1=solve(planez==ells(1),xi)
% % solx2=solve(planez==ells(2),xi)
% % soly1=solve(planez==ells(1),yi)
% % soly2=solve(planez==ells(2),yi)
```

APPENDIX E– FRESNEL ZONE RADIUS: CHANGING LATERAL OFFSET

The following lines of MATLAB code were written to determine the influence of lateral offset on Fresnel zone size. The code utilizes the CREWES MATLAB toolbox and the function in APPENDIX D.

```
clear all
%Changing Lateral Offset
fzapp1=[];fzapp2=[];
ells=[];ells2=[];pouts=[];pouts2=[];WestCs=[];WestCs2=[];
EastCs=[];EastCs2=[];NorthIns=[];NorthIns2=[];SouthIns=[];SouthIns2=[];
WestCs0w1=[];EastCs0w1=[];WestCs0w2=[];EastCs0w2=[];
%%% NEAR SHALLOW %%%
t0=.5;
f=80;
v=1500;
h=500;
wvar=0:10:1500;
for w=wvar
   [ellout,pout,WestCross,EastCross,NorthIn,SouthIn]=OFZ(f,v,h,w,t0);
   ells=[ells;ellout];pouts=[pouts;pout];WestCs=[WestCs;WestCross];
   EastCs=[EastCs;EastCross];NorthIns=[NorthIns;NorthIn];
   SouthIns=[SouthIns;SouthIn];fzapp1=[fzapp1;v*sqrt(t0/f)];
   [~,~,WestCross0w1,EastCross0w1,~,~]=OFZ(f,v,h,0,t0);
   WestCs0w1=[WestCs0w1;WestCross0w1];EastCs0w1=[EastCs0w1;EastCross0w1];
end
figure;
hold on
plot(wvar,(abs(EastCs)+abs(WestCs)))
plot(wvar,ones(length(wvar),1)*(abs(WestCross0w1(1))+abs(EastCross0w1(1))))
plot(wvar,fzapp1)
lgd1=legend('XLine & InLine','InLine','None','Location','EastOutside');
title(lgd1,'Offset Vars Included')
xlabel('Lateral Offset (m)');ylabel('FZ Diameter (m)');title('FZ Diameter vs Lateral Offset');
prepfig
%%% Far Deep %%%
t0=5;
f=30;
v=2100;
```

```
h=6000;
for w=wvar
   [ellout,pout,WestCross,EastCross,NorthIn,SouthIn]=OFZ(f,v,h,w,t0);
   ells2=[ells2;ellout];pouts2=[pouts2;pout];WestCs2=[WestCs2;WestCross];
   EastCs2=[EastCs2;EastCross];NorthIns2=[NorthIns2;NorthIn];
   SouthIns2=[SouthIns2;SouthIn];fzapp2=[fzapp2;v*sqrt(t0/f)];
   [~,~,WestCross0w2,EastCross0w2,~,~]=OFZ(f,v,h,0,t0);
   WestCs0w2=[WestCs0w2;WestCross0w2];EastCs0w2=[EastCs0w2;EastCross0w2];
end
figure;
hold on
plot(wvar,(abs(EastCs2)+abs(WestCs2)))
plot(wvar,ones(length(wvar),1)*(abs(WestCross0w2)+abs(EastCross0w2)))
plot(wvar,fzapp2)
lgd2=legend('XLine & InLine','InLine','None','Location','EastOutside');
title(lgd2,'Offset Vars Included')
xlabel('Lateral Offset (m)');ylabel('FZ Diameter (m)');title('FZ Diameter vs Lateral Offset');
prepfig

figure;
plot(wvar,abs((abs(EastCs)+abs(WestCs))-
ones(length(wvar),1)*(abs(WestCross0w1(1))+abs(EastCross0w1(1)))))
hold on
plot(wvar,abs((abs(EastCs2)+abs(WestCs2))-
ones(length(wvar),1)*(abs(WestCross0w2)+abs(EastCross0w2))))
lgd3=legend('Near/Shallow','Far/Deep','Location','NorthWest');
title('FZ Diameter Including Lateral Offet Minus Not Including Lateral Offset vs Lateral Offset')
xlabel('Lateral Offset (m)');ylabel('Difference In FZ Diameter (m)');
prepfig
```